ETA MESON PHOTOPRODUCTION IN THE REGION OF THE THIRD NUCLEON RESONANCE

Thesis by
Charles Y. Prescott

In Partial Fulfillment of the Requirements
For the Degree of
Doctor of Philosophy

California Institute of Technology
Pasadena, California
1966

ACKNOWLEDGMENTS

The success of this experimental effort must be directly attributed to cooperation in a group association. Clemens A. Heusch, as head of our group, conceived the experiment, laid down general guidelines for the experimental approach, supervised all details of construction of apparatus, and provided continuing motivation during the several years of experimental testing and construction. Elliott Bloom and Leon Rochester assisted in all aspects of the experiment, from equipment construction to data analysis, and deserve a full share of the credit. Walter Nilsson was an invaluable assistant, and every aspect of the apparatus shows his skillful craftmanship, imaginative innovation, and patient attention to detail.

The author appreciates the continual support offered by R. L. Walker and A. V. Tollestrup. Both were sources of helpful suggestions and reliable advice. Many useful conversations with R. Dashen and D. Beder provided awareness of the connections of this experiment with points of interest in current theory. Assistance from the synchrotron crew under Larry Loucks, from Earle Emery, and from the synchrotron operators, headed by Al Neubieser, is gratefully acknowledged.

For financial support, the author is indebted to the National Science Foundation, the Atomic Energy Commission, and to the California Institute of Technology.

ABSTRACT

The differential cross section for the photoproduction reaction

$$\gamma + p \rightarrow \eta^{o} + p$$

has been measured in the energy region about the N*** (1688, 5/2 +) and at an angle $\theta^{*}_{\eta} = 45^{o}$. The eta was detected through its two photon decay mode

$$\eta^{o} \rightarrow \gamma + \gamma \ .$$

Two thin foil spark chambers and an aluminum plate range chamber are used to measure the lab angle and energy of the outgoing proton and two shower counters measure the energies of the decay photons and the lab angle of the η^{o}. Overdetermined kinematical parameters allow the mass of the two photon object to be measured. A striking peak centered at 549.9 ± 1.5 Mev on top of a small, broad background indicates a clean selection of eta mesons. Comparison of the measured ratio

$$N^{***} \rightarrow \eta^{o}p / N^{***} \rightarrow \pi^{o}p$$

provides an experimental measure for the ratio

$$G_{\eta NN^{***}} / G_{\pi NN^{***}}$$

to be compared with predictions of unbroken unitary symmetry. This ratio confirms that the N*** (1688) belongs to a J = 5/2 + baryon octet, and gives experimental limits for the F/D coupling ratio for (PS B B*) couplings.

To Anne

TABLE OF CONTENTS

TABLE OF CONTENTS (cont.)

TABLE OF CONTENTS (cont.)

LIST OF FIGURES

LIST OF FIGURES (cont.)

LIST OF FIGURES (cont.)

LIST OF TABLES

I. INTRODUCTION

This thesis is the study of the reaction

$$\gamma + p \rightarrow \eta^{o} + p$$

in the vicinity of the third nucleon resonance. The history of the discovery of the eta meson is an interesting and valuable episode in the growth of the field of elementary particle physics. The results of electron-proton scattering had led theorists to predict the existence of a vector meson of light mass (around 400 Mev) in order to explain the behavior of the isoscalar part of the nucleon form-factor. Investigation of π-meson triplets was completed in 1961 by a bubble chamber group[1] studying the reaction

$$\pi^{+} + d \rightarrow p + p + \pi^{+} + \pi^{-} + \pi^{o}$$

The mass plot of the π-meson triplets showed clear peaking of masses at 760 Mev and at 550 Mev. The peak at 550 Mev was interpreted as evidence for the much-desired isoscalar, $J^{P} = 1^{-}$, meson.

Investigation of reactions looking for an η^{+} produced negative results indicating that the η was indeed an isoscalar particle. The initial excitement generated by its discovery turned into a major disappointment, however, when the η failed to satisfy the basic requirements of those theories that motivated the search. The discovery of the decay mode

$$\eta^{o} \rightarrow 3\pi^{o}$$

upset the neat picture, since an I = 0 state cannot be constructed out of 3 π^o's. Existence of this decay mode required that isotopic spin be violated in the decay. Finally, discovery of the decay mode

$$\eta^o \rightarrow 2\gamma$$

showed that the decay was electromagnetic in nature, and furthermore that the particle was a pseudoscalar meson, like the π^o. Thus the quantum numbers of the meson were identified as $J^{PG} = 0^{-+}$, I = 0. However, the theory of unitary symmetry existed at this time and predicted the existence of this new meson.[2] Indeed this success was so impressive that SU(3) became the new fashion of elementary particle physics. Thus, in 1961 a new meson entered into the particle scheme. This new particle was light enough to be produced by a number of particle accelerators in existence, and experiments were immediately undertaken to produce the particle in π and γ beams. This thesis reports one such experiment performed at the Caltech Synchrotron Lab.

A series of liquid hydrogen bubble chamber experiments and heavy liquid bubble chamber experiments have identified and measured the different decay modes of the η^o.[3-8] Table 1.1 gives the significant decay modes and branching ratios as they stand at this time.[9]

The quantum numbers and decay modes of the eta are well established and questions are now arising concerning the interactions of the eta with other particles. In the limit of unitary symmetry, predictions of coupling constants of the η to the baryons relative to those for the π^o lead directly to experimental observables under specific assumptions for the interaction kinematics. Specifically, we have chosen in this experiment to study

TABLE 1.1

Decay Modes and Branching Ratios for the Eta Meson

Decay Mode	Fraction (%)
$\gamma\gamma$	38.6 ± 2.7
$3\pi^0$ and $\pi^0 2\gamma$	30.8 ± 2.3
$\pi^+ \pi^- \pi^0$	25.0 ± 1.6
$\pi^+ \pi^- \gamma$	5.5 ± 1.2

the third nucleon resonance (N***, 1688, $J^P = 5/2^+$, I = 1/2) with the intention of measuring its contribution to eta photoproduction. The N*** (1688) is known to contribute significantly to π^o photoproduction, and since eta mesons have the same spin and parity, the contribution of N*** to η^o photoproduction should differ only in coupling constants and kinematical factors.

Experimentally, we perform a measurement of the process

$$\gamma + p \rightarrow p + \eta^o \hookrightarrow 2\gamma$$

for the lab photon energies $950 \leq k_\gamma \leq 1100$ Mev and angles in the lab corresponding to $\theta^*_\eta = 45^o$, where the angular distribution from the $F_{5/2}$ decay is expected to exhibit a maximum. Hopefully, then, the results will allow for separation of isobar production, if other processes do not contribute significantly.

R. F. Dashen has worked out a general discussion of contributing processes in η photoproduction.[10] Figure 1.1 shows the type of processes that may be expected to contribute. These Feynman diagrams are identical to diagrams which occur in π^o photoproduction. The coupling constants used at the outgoing vertex correspond to the eta meson instead of the π meson, and in some cases, conservation of I-spin requires the couplings to be zero. For example, the first nucleon resonance (N*, 1238, $J^P = 3/2^+$, I = 3/2) cannot decay into $p + \eta^o$ (I = 1/2) and similarly for the fourth nucleon resonance (N****, 1924, J = 7/2, I = 3/2).

Charge conjugation invariance rules out exchange of a single π^o or η^o. Exchange of a single photon ("Primakoff Effect") should exist, but be small because of the small coupling at the $\eta\gamma\gamma$ vertex. Contribution to π^o photoproduction from the nucleon Born

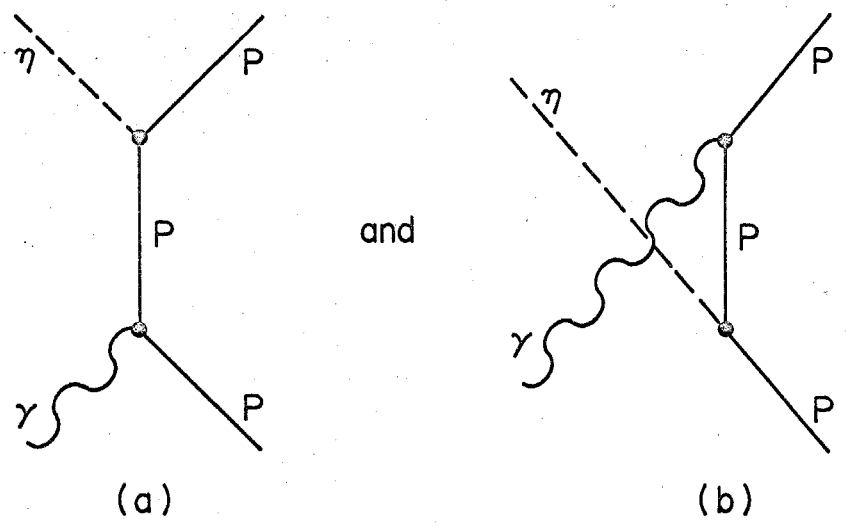

NUCLEON BORN TERMS

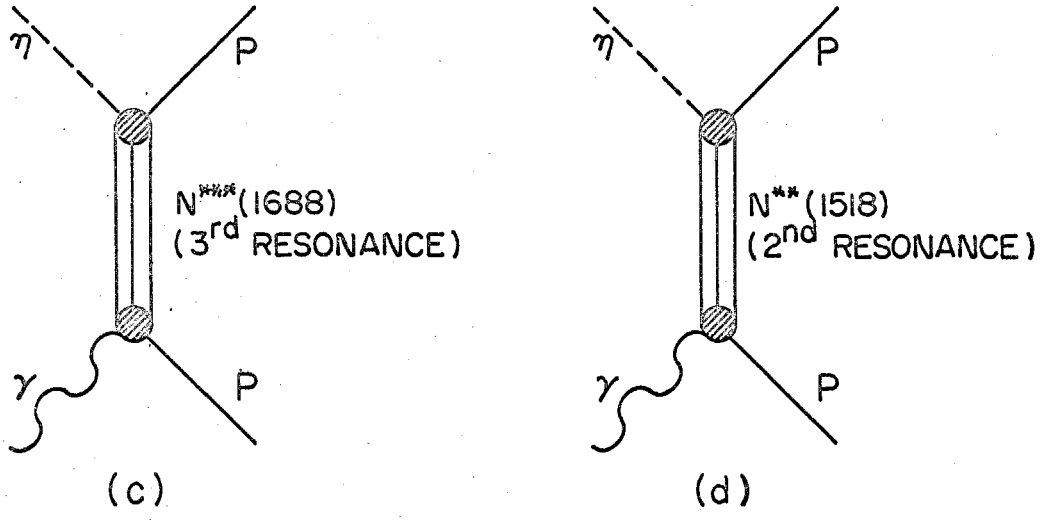

ISOBAR TERMS

Figure 1.1 Diagrams of processes contributing to eta photoproduction

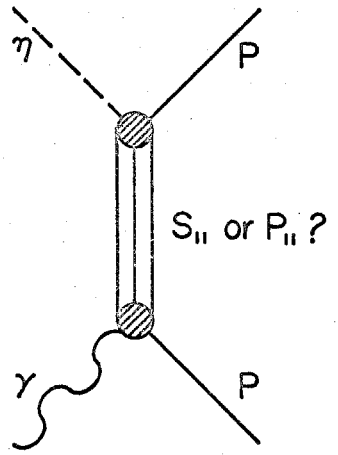

(e)

ISOBAR TERMS

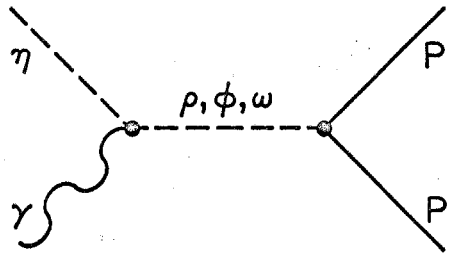

(f)

VECTOR EXCHANGE

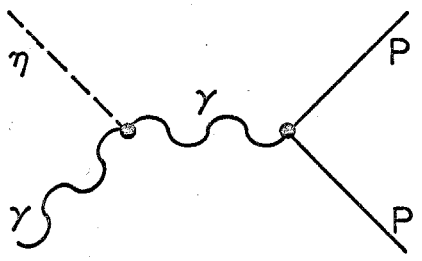

(g)

PRIMAKOFF EFFECT

Figure 1.1 (cont.) Diagrams of processes contributing to eta photoproduction

terms (diagrams (a) and (b)) are experimentally found to be much smaller than calculation of these first order diagrams predicts. We expect that the contribution from Born terms to η photoproduction would be suppressed by the same mechanism that suppresses them in π^0 photoproduction. Furthermore, unitary symmetry predicts

$$G_{\eta NN} = 1/\sqrt{3}\ (3 - 4\alpha)\ G_{\pi NN}$$

where $\alpha/(1 - \alpha)$ is the ratio of D to F type coupling. Experimental results give $\alpha \tilde{=} 2/3$ which give

$$G_{\eta NN} = 1/3\sqrt{3}\ G_{\pi NN}\ .$$

On this basis the Born terms would be further suppressed.

Contributions from the isobars may play the most important role in η photoproduction as they do in π^0 photoproduction. Cross section measurements near η-threshold show that both in π-production and in photoproduction of η^0's an enhancement occurs which has been variously interpreted as evidence for either an S_{11} or a P_{11} nucleon resonance of mass somewhere in the range 1400 - 1500 Mev.[11-17]

The second nucleon resonance (N**, 1512, $J^P = 3/2^-$, I = 1/2) is not expected to contribute significantly to η photoproduction. Experimentally observed angular distributions are flat in this region and are therefore inconsistent with a D-wave. The resonance peak is only 10 Mev above eta threshold, and the angular momentum barrier significantly suppresses this contribution. Kinematical factors in the cross section introduce $(q^*/m)^{2\ell+1}$ for $\ell = 2$. Furthermore, SU(3) predicts that

$G_{\eta NN^{**}} = 1/10\ G_{\pi NN^{**}}$, so that for the overall contribution to η photoproduction one obtains

$$\Gamma(N^{**} \rightarrow \eta^{o} + N) \leq 10^{-3}\, \Gamma(N^{**} \rightarrow \pi^{o} + N) \ .$$

The third resonance is of more interest experimentally. It is known to have spin = 5/2 and positive parity. The branching ratio into $\eta^{o}p$ and $\pi^{o}p$ depends on the strength of the outgoing vertex and on kinematical factors. One finds

$$\frac{\sigma(\gamma p \rightarrow p\eta)}{\sigma(\gamma p \rightarrow p\pi)} = \frac{G^{2}_{\eta NN^{***}}}{G^{2}_{\pi NN^{***}}} \frac{f(q_{\eta})}{f(q_{\pi})}$$

where $f(q)$ is a kinematical factor arising from angular momentum barrier penetration and phase space available to the outgoing states. A fully relativistic calculation of $f(q)$ involves entanglement in spin 5/2 formalism, and Dashen suggests the use of an approximation originally employed by Glashow and Rosenfeld[18]. He gets $f(q_{\eta})/f(q_{\pi}) = 1/3$. Furthermore, as before, if $\alpha'/(1 - \alpha')$ is the ratio of D to F type coupling for the (PS B B*) coupling, unitary symmetry predicts $G_{\eta NN^{***}} = 1/\sqrt{3}\ (3 - 4\alpha')\ G_{\pi NN^{***}}$ where the N^{***} has been placed in a $J^{P} = 5/2^{+}$ baryon octet, according to the suggestion of Glashow and Rosenfeld[18]. Measurement of the relative sizes of the coupling constants $G_{\eta NN^{***}}$ and $G_{\pi NN^{***}}$ will yield a value for α', which will not necessarily agree with α obtained for other baryon octets.

Finally, another process may contribute to η photoproduction, given by Figure 1.1 (f). The effect of exchange of vector mesons has apparently been seen in π^{o} photoproduction at forward angles in the region of the N^{***} (1688) and at higher

energies.[19, 20] The differential cross section for η photoproduction for this diagram takes the form

$$\frac{d\sigma}{d\Omega} = \frac{1}{2} |A(\Delta^2)|^2 \, k \, q \, w^2 \left(\beta^2 \sin^2\theta + \frac{\Delta^2}{2W^2}(1 - \beta\cos\theta)^2\right)$$

where

$\Delta^2 = 2kw(1 - \beta\cos\theta) - M_\eta^2$

q = η Momentum

w = η Energy

k = photon energy

W = total c. m. energy

$\beta = q/w$

and $A(\Delta^2) = 1/4\pi \left(\frac{1}{2} \frac{f_{\rho NN} f_{\rho\eta\gamma}}{\Delta^2 + M_\rho^2} + \frac{f_{\omega NN} f_{\omega\eta\gamma}}{\Delta^2 + M_\omega^2} + \frac{f_{\varphi NN} f_{\varphi\eta\gamma}}{\Delta^2 + M_\varphi^2} \right)$.

Presence of such terms would be indicated by peaking of the differential cross section at forward angles. In light of the fact that such terms are indicated in π^o photoproduction, it would be interesting to see if they are observed in η photoproduction.

To carefully separate and identify each of these processes requires a major experimental effort. Differential cross sections would have to be measured at many angles and energies. This experiment was necessarily limited by time available, so objectives were narrowed down. The experiment was proposed to measure the amount of N*** in η photoproduction and the kinematical parameters were chosen to best show this off. The apparatus was set so that it could scan an incident photon energy range of 950-1100 Mev (the N*** is centered at k_γ = 1020 Mev in

the lab) and at a center-of-mass angle of 45^{o}. A pure $F_{5/2}$-wave has an angular distribution

$$\frac{d\sigma}{d\Omega} \sim 1 + 6 \cos^{2}\theta^{*}_{\eta} - 5 \cos^{4}\theta^{*}_{\eta}$$

which has maxima near $\theta^{*}_{\eta} = 39^{o}$ and 141^{o}, and a minimum at 90^{o}. The intention is to isolate the amount of $F_{5/2}$ in the η cross section by looking for a bump in the cross section as one scans through the N*** resonance.

II. EXPERIMENTAL METHOD

The process under study in this experiment is the two-body reaction

$$\gamma + p \rightarrow \eta^{o} + p \ .$$

The photoproduction cross section has been measured in previous experiments at energies below those of this experiment and at center-of-mass angles different from those proposed for this experiment.[21] The results of these early experiments indicated that a rather small cross section would exist at the energies above 1000 Mev, and consequently the counting rate would be rather low. Thus, it was felt that background problems might be severe, and it would be desirable to over-determine all parameters to the maximum extent possible to help suppress potentially severe background contamination.

In a two-body reaction, all kinematical parameters are determined if one measures the angle and energy of one of the final state particles, provided the masses of the particles and the direction of the incident beam are known. Measurement of angle or energy of the other outgoing particle constitutes over-determination of the kinematics, and provides a stringent test of all events, by which backgrounds can be identified and weeded out.

In this experiment eta mesons were photoproduced off protons contained in a liquid hydrogen target. The angle of the recoil proton was measured by means of two thin-foil spark chambers, and the energy of the proton was measured by its range in an aluminum thick-plate spark chamber.

The eta meson is a short-lived particle (estimated $\tau \sim 10^{-19}$ sec.) that decays into $\pi^+\pi^-\pi^o$ (25.0 ± 1.6%), $3\pi^o$ and $\pi^o 2\gamma$ (30.8 ± 2.3%), 2γ (38.6 ± 2.7%), and $\pi^+\pi^-\gamma$ (5.5 ± 1.2%). The mode $\eta^o \rightarrow 2\gamma$ is a good means for detecting the decay of an η meson because the opening angle and energy of the photons are characteristic of the mass of the η. Since the decay of the η is electromagnetic, the width of the η is very narrow (~ 1 kev) and for all practical purposes, it can be considered stable. That is, the mass of the η is much too narrow to cause any broadening of the two-body kinematics. The lab energy of the two decay photons of the eta meson was measured by two lead-lucite sandwich counters, described in detail in the Appendix, Section VII-A. Briefly, these counters consist of six 1/2" lucite sheets, machined and polished to form a lucite radiator assembly shown in Figure 7.1. Lead sheets, 1/2 centimeter thick, are placed between the sheets, and two sheets are placed in front of the counter. Energetic electrons, positrons, or photons that are incident on the aperture of the counter initiate a cascade shower in the lead-lucite sandwich. The charged particles of the shower that pass through the lucite sheets generate Cerenkov light in an amount proportional to the total particle-track length in the lucite. Since the counter largely contains the showers for energies expected in this experiment, the total light generated in the lucite is proportional to the energy of the incident particle. A photomultiplier is attached to the lucite. The integrated pulse from the photomultiplier is used to measure the amount of light generated in the counter, and hence is a measure of the energy of the shower. Fluctuations in the amount of Cerenkov light and fluctuations inherent in the photomultiplier broaden the energy resolution of the counter. (for details, one should see Section VII-A).

The lab angle information for the two decay photons of the eta is obtained by a piece of apparatus referred to as the scintillator hodoscope. There are two scintillator hodoscopes, one for each shower counter. Each scintillator hodoscope consists of five 2" by 6" rectangular pieces of scintillator plastic, attached to 2" photomultipliers. The five scintillator counters were placed side by side, in front of the shower counter aperture, so as to subdivide the aperture into five parts. The first two lead sheets of the shower counters were placed in front of the scintillator hodoscope counters so that photons from the eta meson would convert (i. e., pair-produce) in this lead with a 78% probability (see Appendix, Section VII-D) and would trigger one of the five scintillator counters. The scintillator hodoscopes measure the lab production angles of the decay photons in this manner and taken together constitute a measurement of the production angle of the eta meson.

Since the η has spin 0, the distribution of photons in the center-of-mass is uniform. If one takes the uniform distribution in the center-of-mass and transforms it into the lab system, one finds the distribution is peaked in the direction of the η:

$$\frac{dN}{d\Omega} = \frac{dN}{d\Omega^*}\frac{d\Omega^*}{d\Omega} = \frac{2}{4\pi} \cdot \frac{1 - \beta_\eta^2}{(1 - \beta_\eta \cos\theta)^2}$$

where θ is the angle (in the lab) with respect to the η direction.

If one wishes to detect both of the decay photons simultaneously, one finds that the distribution is best described by the opening angle between the two photons. This distribution falls discontinuously to zero for $\theta_{\gamma\gamma}$ angles less than the minimum opening angle given by

$$\sin \theta/2 = M_\eta/E_\eta$$

and for $\theta_{\gamma\gamma}$ larger than this is given by

$$N(\theta)d\theta = \frac{M_\eta}{2P_\eta} \frac{\cos\theta/2 \, d\theta}{\sin\theta/2 \sqrt{(E_\eta/M_\eta)^2 \sin^2 \theta/2 - 1}} .$$

The effective solid angle for detecting both photons is largest if the counters are centered at the minimum opening angles for the decay photons:

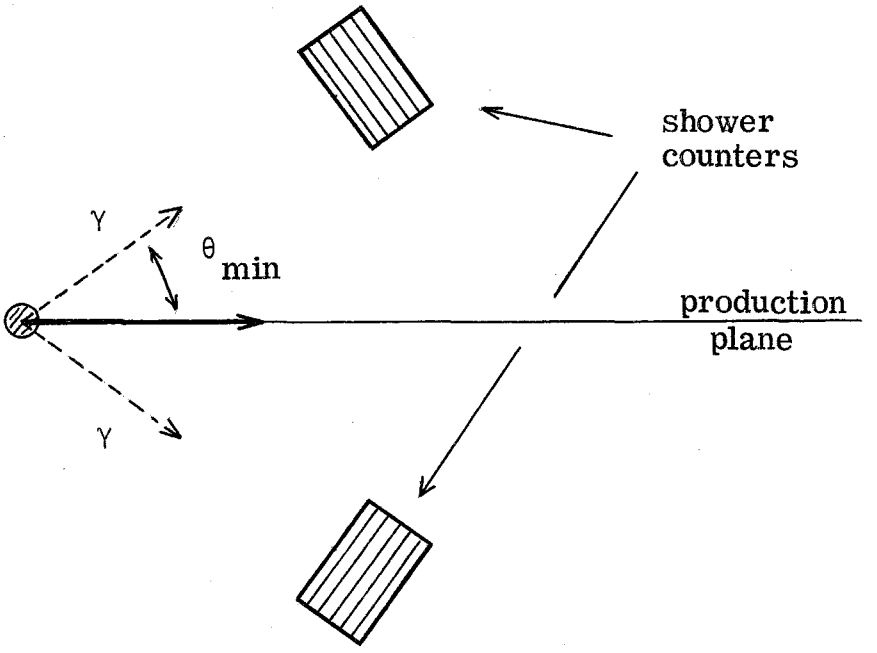

Accordingly, the two shower counters were placed at the lab production angle of the outgoing η meson ($\theta_\eta \sim 20^o$), symmetrically above and below the horizontal production plane ($\theta_{\gamma\gamma/2} \sim 36^o$).

Figure 2.1 shows the layout of the apparatus in the experimental area. The electrons in the synchrotron are accelerated to an energy E_o and the magnetic field in the synchrotron is held

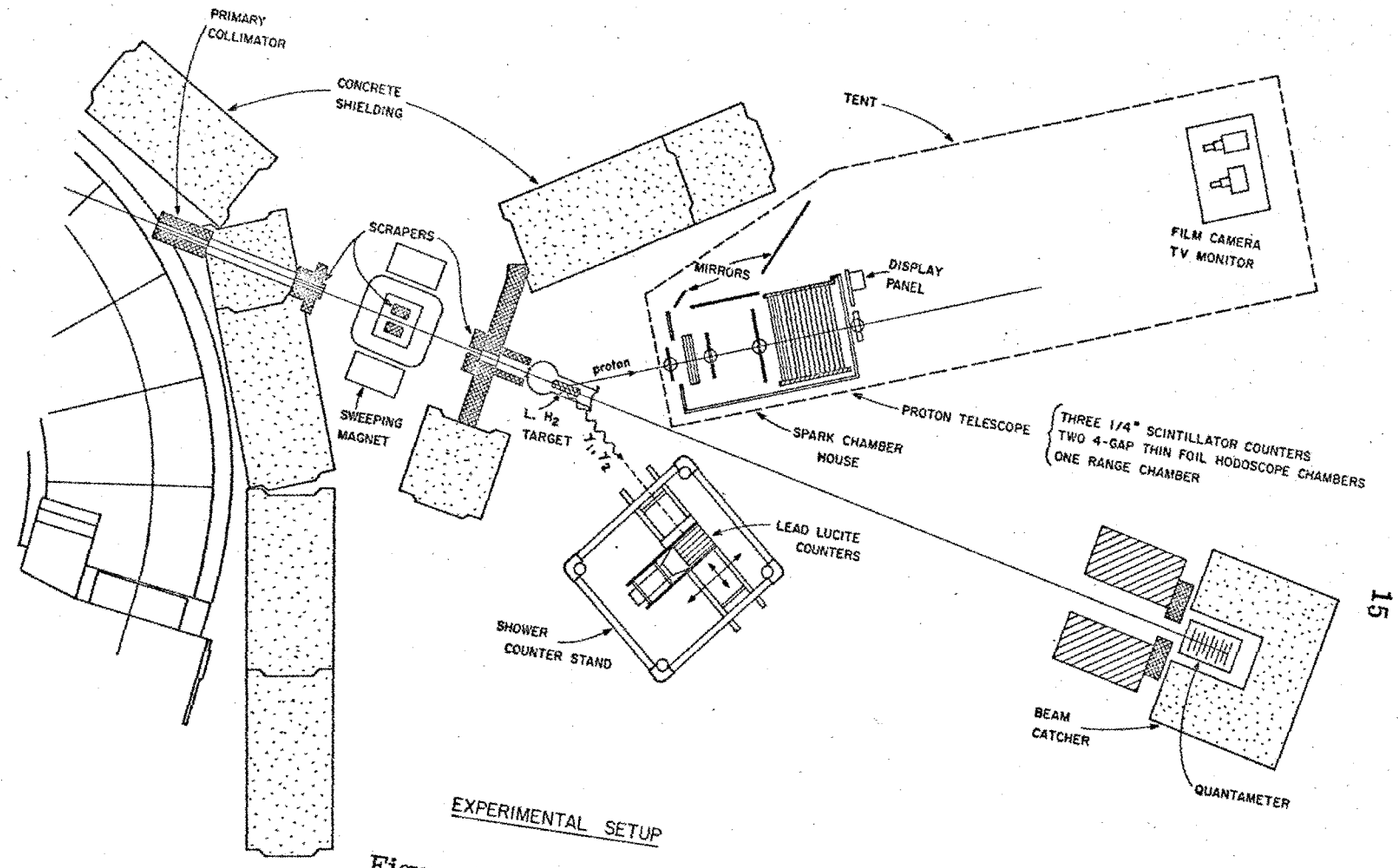

Figure 2.1 The experimental area

constant at its peak value. A target is flipped into the electron path, and bremsstrahlung of the electrons produces a photon beam uniform in intensity and lasting about 100 milliseconds per dump. This beam passes through a primary collimator and several tight scrapers before reaching the hydrogen target. Downstream from the target and to the left at 40° was placed the proton telescope, level with the target. On the right side, opposite the proton telescope, were placed the shower counters. The proton telescope, consisting of three scintillator counters and three spark chambers, were enclosed in a large tent to allow photographs of the spark chamber tracks to be taken. Events were triggered by a fast three-fold coincidence between the two shower counters and the proton telescope. Events thus recorded on film consisted of tracks in the spark chambers plus pulse height and angle information from the shower counters displayed on the film by coded incandescent lamps. By suitable positioning of mirrors, 90° stereoscopic views of each chamber were obtained. A television camera was placed close to the position of the film camera. The television monitor set was placed in the experimental control area to allow continual monitoring of the performance of the spark chamber system. The frames of film were each visually scanned on a projection table. Those events which appeared reasonable were then measured by position encoders on the table. The information from the table was punched on IBM cards in a form suitable for computer analysis of the events. The description of the scanning process and computer analysis will be found in the next section. A more detailed description of apparatus and electronics is contained in the Appendix.

This experiment consists of three independent runs taken at different, but overlapping kinematical settings. The counters

were set at positions chosen so that the incident energies, k_γ, were from overlapping ranges. Table 2.1 gives the kinematical parameters for the three runs. These values were chosen to cover the N*** (1688) resonance at 45^o in the center-of-mass.

TABLE 2.1

Kinematical Parameters

Run	k_o	θ^*_η	θ_p	T_p	θ_η	E_η	$\theta_{\gamma\gamma/2}$
	Mev	deg	deg	Mev	deg	Mev	deg
1	975	48	38.2	86.9	21.4	888.9	38.3
2	1025	45	40.8	84.13	20.3	941.7	36.3
3	1075	44	42.9	86.4	19.9	989.4	33.6

III. ELEMENTS OF THE ANALYSIS

A. Scanning Procedure

The film readout of each event was designed so that all the available information was displayed on the film. Figure 3.1 shows the format of a typical "good" event. Frames like the one in Figure 3.1 were scanned for good events. These were events that had a stopping track in the range chamber and one lamp lit in each the upper and lower scintillator hodoscope counters indicating that the photon had converted in the lead in front of the hodoscope counter. It was necessary to restrict the selection of events to those for which both photons converted. Only in these events were the kinematical restraints tight enough to allow separation of background. The scintillator hodoscopes had two radiation lengths of lead in front for the conversion of the γ's. The detection efficiency in this configuration was 78% for each counter. The events that passed these simple criteria were then measured on a digitized measuring table. This process consisted of measuring the spark coordinates and fiducial mark coordinates in both stereoscopic views of the three spark chambers. Cross hairs on the measuring table were placed on the spark or fiducial mark and a foot pedal was pressed. The scanning table coordinates of that point were then automatically punched out on IBM cards in a specified format. On the same card the shower counter pulse height information, hodoscope information, and numbers of range chamber gaps firing were entered by means of a parameter board associated with the apparatus. This process transferred the information on the film to IBM cards so that the computer could reduce the data.

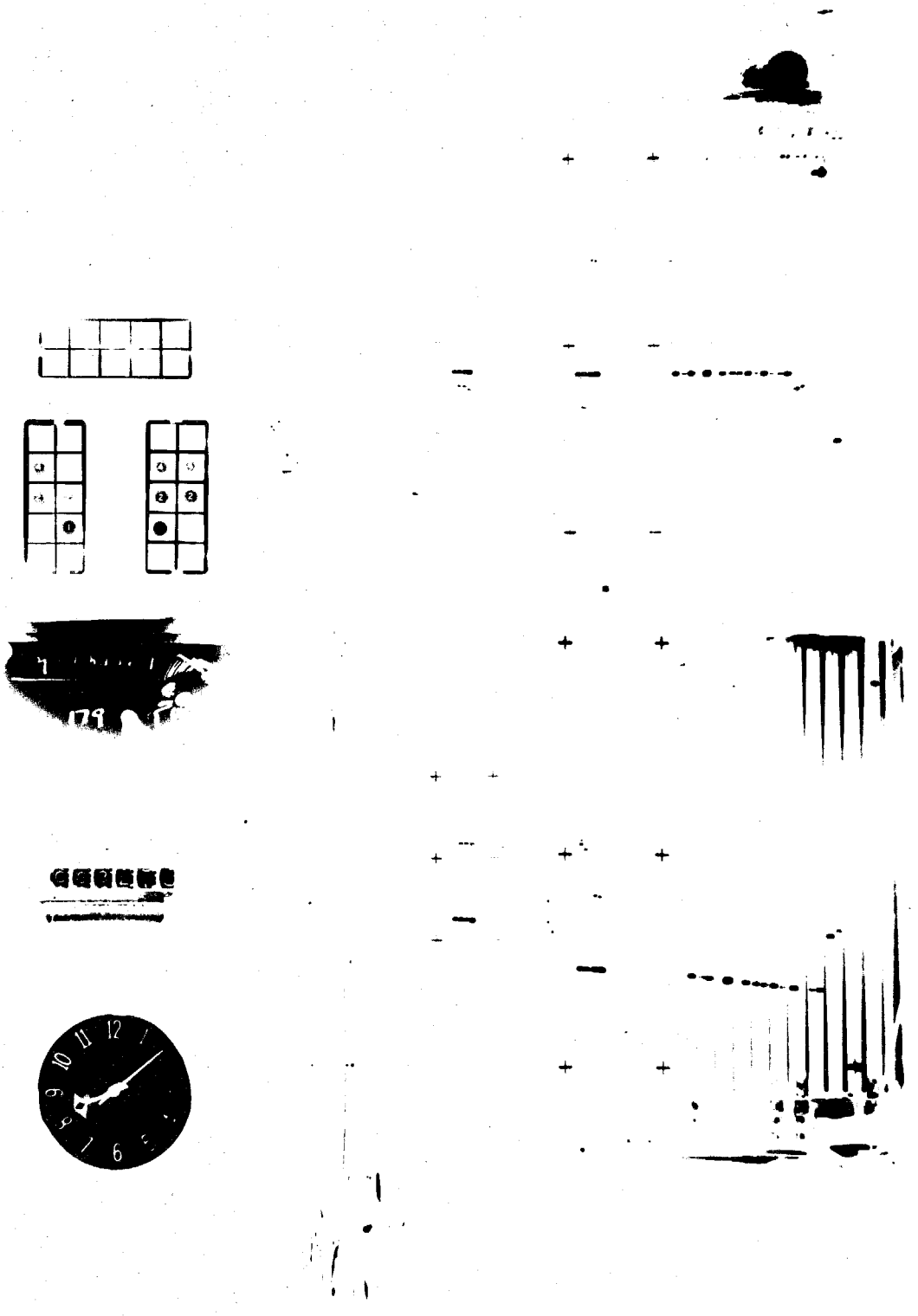

Figure 3.1 Typical spark chamber exposure showing stopping proton. The right half of the frame shows the three spark chambers in stereo views.

It was found that scanning of the events one time located only in the order of 90% of the good events. It was necessary to scan the whole set of film a second time to find the other 10% of the events. The second scan yielded a high degree of consistency, but wherever discrepancies were found, a third measurement was called for. Many events thus were scanned three or more times before uncertainties could be resolved. It is assumed in the further analysis that all good events were found by this method. Complete scanning and rescanning of the experiment, including measurements of all acceptable events required approximately six months. There were 12,000 frames of data involved in the experiment.

B. Measurement Accuracies; Distortions

The measuring table is digitized by encoders into 10,000 discrete units in both the X and Y coordinates. Table 3.1 gives the dimensions of the two hodoscope chambers in real space, in scanning table coordinates, and the scale factors for each view. The range chamber is omitted since it was used only to measure range. The scale factor is the ratio of real space dimensions (in cm) to scanning table dimensions (in scanning table units). The different scale factors for each view result from the different distances of each view from the camera. Using the scale factor, then the real space coordinates of the sparks are found by extrapolating from a near-by fiducial mark, whose coordinates are known in the lab. Repeated measurement of the same frame on the scanning table has shown that the measurement reproducibility is $\pm$ .1 millimeters in real space. The largest error in the measurement of the spark coordinates is the uncertainty in the location of

TABLE 3.1

Spark Chamber Dimensions and Scale Factors

Front Hodoscope Chamber	Real Space Length	Scanning Table Length	Scale Factor
	cm	units	
Top View	25.4	1320	.01932
Side View	20.32	1186	.01725
Back Hodoscope Chamber			
Top View	44.45	2709	.01658
Side View	44.45	3072	.01469

the fiducial marks themselves, and is thought to be of the order of ± 1 millimeter. Multiple scattering of the proton amounts to about ± 1 centimeter in the back hodoscope chamber, but this is symmetrical about the true direction and cannot cause any systematic errors in the experiment. Multiple scattering of the proton broadens the experimental resolution, and discussion of this effect is found in a later section.

Optical distortions were looked for and found to be non-existent to the precision of the scanning table. One mirror was found to have a cylindrical warp after completion of the experiment, but calculation of the error showed that it introduced .4 millimeters error at the extremes of the chamber and negligible in the regions used.

C. Data Reduction

Two basic criteria for each event were applied at the scanning table. These were that

1) The event show a clearly discernible stopping track in the range chamber, and

2) Both shower counters show a converted photon in the scintillator hodoscope counters.

These simple criteria eliminated approximately 90% of the events recorded during the experiment. Approximately 60% of these were eliminated because one or both of the scintillator hodoscopes did not register an event, and the other 30% resulted from the spark chambers showing no track at all, or a passing track.

At this point, all events which passed the criteria were measured and submitted to the computer for computer analysis. The computer was programmed to:

1) compute the spatial coordinates of the sparks
2) find the proton angle, θ_p, from these coordinates
3) compute the proton energy, E_p, from the range-energy relations fed in as external data
4) calculate the most likely origin of event in the target
5) compute an "observed eta angle", θ_η, from the coordinates where the two photons converted
6) calculate a "calculated eta angle" from the information on the proton side and find the difference, $\Delta\theta$, of the calculated and the observed eta angles
7) using the proton kinematical parameters and the angles for the two photons, calculate the mass of X for the reaction

$$\gamma + p \rightarrow p + X \hookrightarrow 2\gamma$$

The computer program required approximately 100 milliseconds to analyze each event. Those events which appeared to come from the target (plus an allowance for the multiple scattering of the proton) were kept. Pulse height requirements on the shower counters were used at this point. Calibration of the pulse height spectrum on fast π's showed that the mean of the π-distribution fell in channel 15 of the pulse height analyzer. A bias of 18 was

applied so as to exclude events triggered by low energy photons, thus artificially introducing an inefficiency in shower detection. This served to suppress the background of π^0-pairs and other unwanted processes, since photons from these events tend to have low energies. The number of events which survived this analysis constituted approximately 5% of the total triggers. Of these, 3/5 could be shown to come from η production, while the remaining 2/5 come from background processes. The calculation of the background contamination and subtraction are the subject of Section V and the Appendix.

D. Proton Range-Energy Relations

One of the measurements central to the experiment was that of the range of the proton. It is necessary to do a careful calculation of the range of the proton as a function of its initial energy, in order to insure a good measurement of the energy of the incident photon.

In the experimental situation, the proton encounters a series of materials before entering the aluminum range chamber. Furthermore, protons passed through different amounts of liquid hydrogen depending from which side of the target the event originated. It was necessary to take these considerations into account in detail. For example, it was found that omission of the black tape wrapped around the three proton counters would have given an error of 2 Mev in the proton energy. Therefore a computer program was written which would take various elements of the range telescope and integrate the proton energy losses to the point where the proton stopped, thus yielding its range. Let

$$W_{max} = \frac{(T_p + M_p)^2 - M_p^2}{M_p\left\{\frac{M_p}{2m_e} + \frac{m_e}{2M_p} + \frac{T_p + M_p}{M_p}\right\}}$$

and

$$\beta^2 = 1 - \left(\frac{M_p}{M_p + T_p}\right)^2$$

where

T_p = proton kinetic energy

M_p = proton rest mass

Then the proton energy loss can be written

$$-\frac{1}{\rho}\frac{dE}{dx} = A\left\{F_1(T_p) - 2\right\} - B\left\{F_2(T_p)\right\}$$

where

$$F_1(T_p) = \frac{1}{\beta^2}\ln\frac{\beta^2 W_{max}}{1 - \beta^2}$$

and

$$F_2(T_p) = \frac{1}{\beta^2}$$

and where A, B are constants that depend on the stopping material only, and ρ = stopping material density.[22]

The constants were adjusted to fit the tables given in reference (22) for each material in the proton telescope. Figure 3.2 shows the range-energy curves for the configuration of the telescope used in the experiment. The three curves correspond to three positions of the origin in the target; nearest to the spark

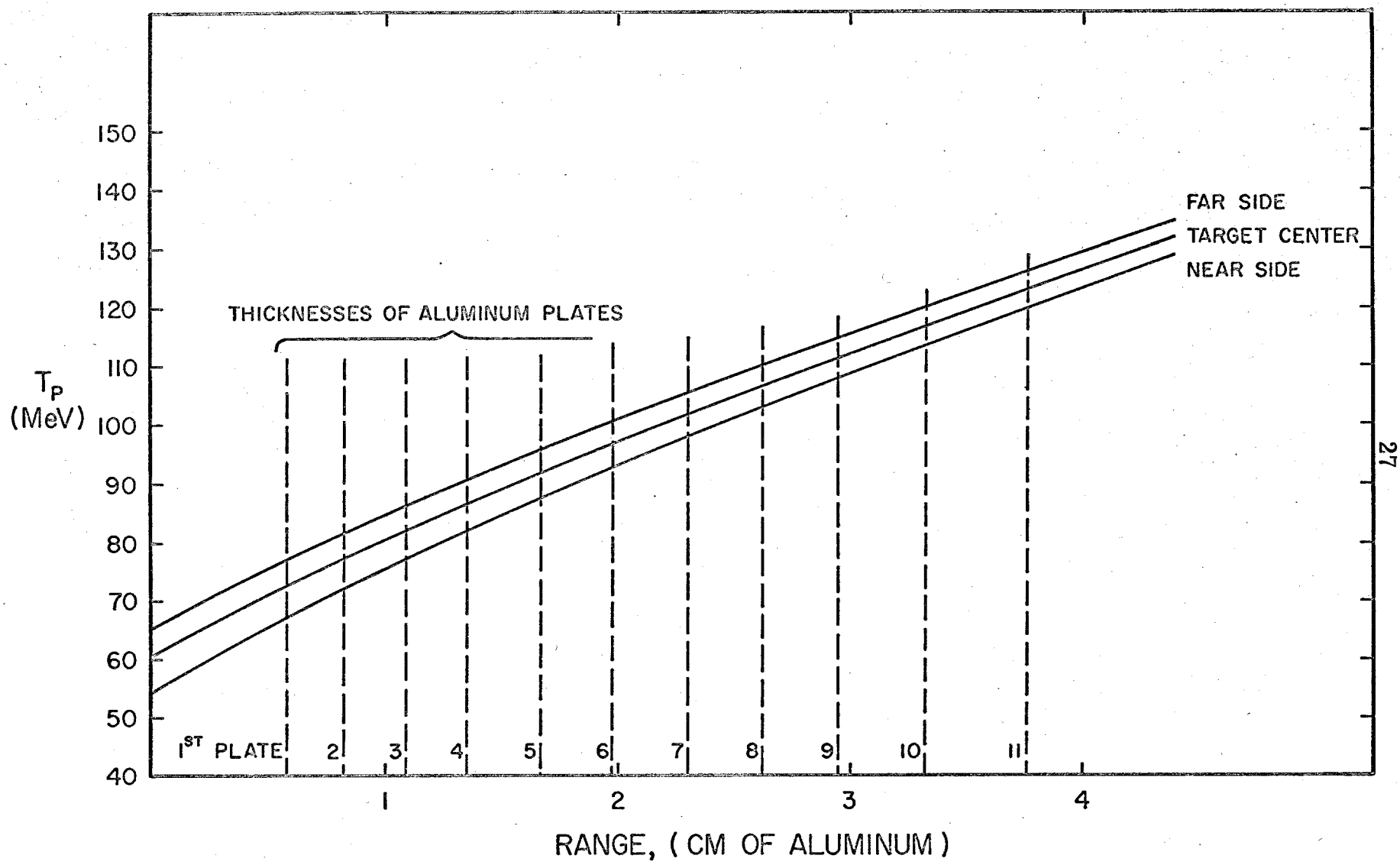

Figure 3.2 Proton kinetic energy versus range in the aluminum range chamber

chambers, center of the target, and the farthest point in the target from the spark chambers.

From these curves it is seen that the largest error in T_p comes from the uncertainty of where the origin of the event occurs in the target. Dividing the stopping material into 11 discrete units also adds to the uncertainty in the range, but it is seen from Figure 3.2 that this contributes errors only about 1/2 of those from the finite target. Straggling of the proton is also a potential source of error in the range measurement, but amounts to 1.2% at 100 Mev in aluminum.[22] These combined errors give a T_p measurement of $\pm$ 4%. These errors should be centered about the true value of T_p, and it is felt that the systematic errors in T_p are held to 1% or less.

E. Multiple Scattering of the Proton

Multiple scattering of the proton is the most important effect in broadening of the resolution of the experiment. It not only affects directly the measurement of the proton angle θ_p, but is felt in other measurements because it changes the position of the apparent origin in the target. For purposes of calculation of the experimental resolution, the well-known gaussian approximation was used;[23]

$$\langle \theta_{MS} \rangle = \frac{15}{P\beta} \sqrt{L/L_{RAD}} \quad (1 + \epsilon) \text{ (radians)}$$

where L/L_{RAD} = thickness in radiation lengths and $\epsilon = -.1$ for thin scatterers. For a number of scatterers such as this experiment has, the square of the mean projected angle is added for each element.

In this telescope, the three scintillator counters accounted for 2/3 of the multiple scattering, while air and the hydrogen target accounted for the other third. Figure 3.3 shows the variation of total $\langle \theta_{MS} \rangle$ as a function of T_p. Multiple scattering in the range chamber is not included here because the proton angle was measured with the two hodoscope chambers, before the proton reached the range chamber.

F. Computer Simulation of the Experiment; Calculation of Resolution in Mass of Eta; $\Delta\theta$ Calculation

A Monte Carlo program was written which reproduced as closely as possible the experimental situation. This program generated events in the target, tested the proton to see if it entered the solid angle of the proton telescope, allowed the η to decay uniformly in its center-of-mass and tested to see if both photons entered the aperture of the shower counters. For those events which succeeded, the proton was allowed to multiply scatter and stop in the range chamber. The kinetic energy assigned to the proton was that given to protons which stop at the center of the corresponding range chamber module, and the two photon angles assigned to the photons were those given to photons that convert at the center of the corresponding scintillator hodoscope. This process was repeated uniformly within the finite target. Thus this program duplicates as well as possible the experimental effects. Each successful event was analyzed in precisely the same manner as the data that were obtained from the film.

A distribution of importance is the measured mass of the eta. In the Monte Carlo calculation the mass of the eta is

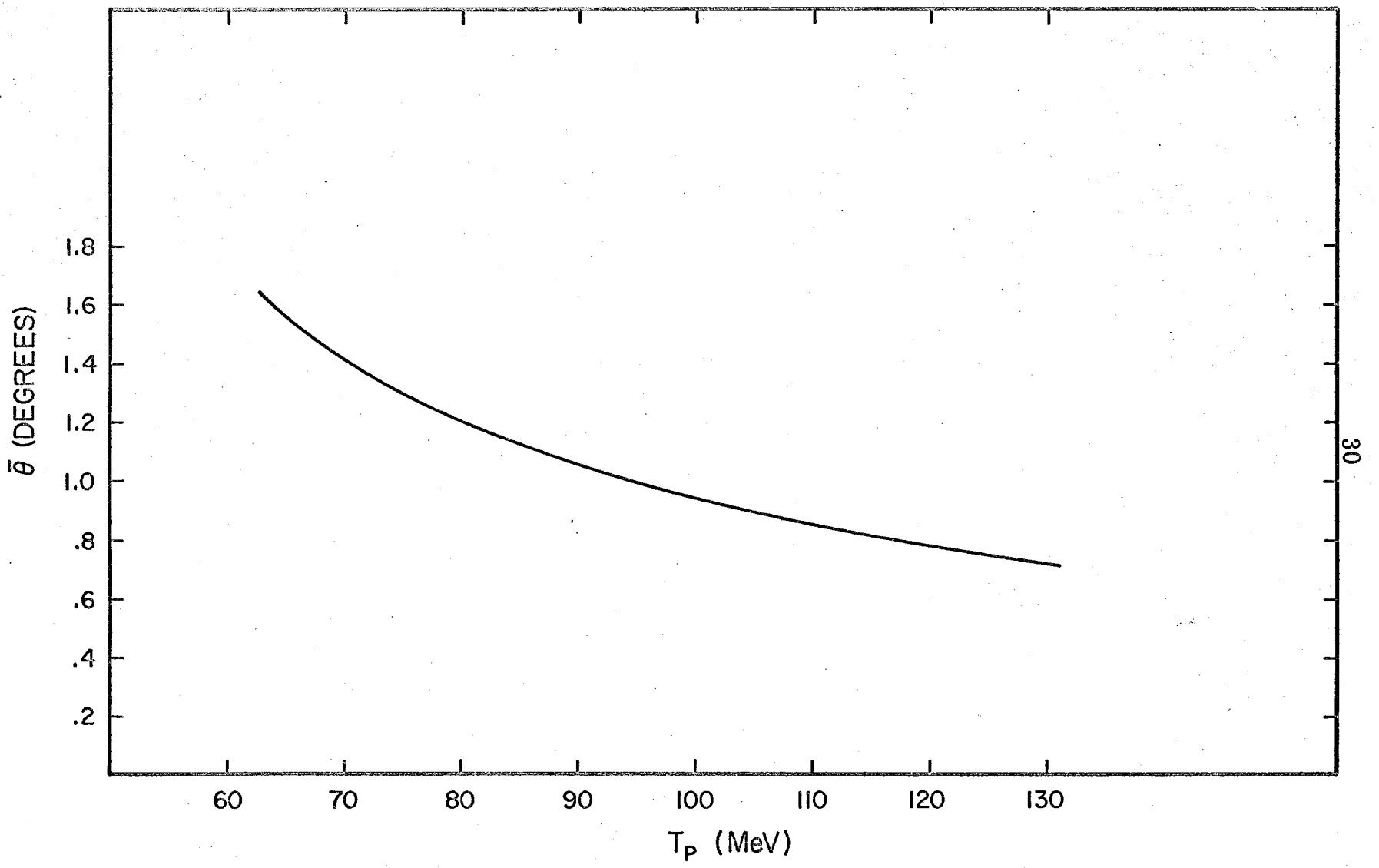

Figure 3.3 Proton multiple scattering versus kinetic energy

introduced in the kinematics, so that the calculated distribution should be peaked about $M_\eta = 548.8$ Mev, but have a width due to the experimental resolution. Figure 3.4 shows the results of the calculation. The histogram is the Monte Carlo program output, while the curve is a best gaussian fit to the histogram. The distribution goes to zero at $\pm$ 40 Mev. This fact is used later to improve the separation of good events from background events.

The same kinematical parameters can be used to calculate a second distribution called the "$\Delta\theta$ distribution". This amounts to obtaining a calculated θ_η from the proton information and comparing it to the observed θ_η. The quantity $\Delta\theta$ is then

$$\Delta\theta_\eta = \text{calculated } \theta_\eta - \text{observed } \theta_\eta \quad .$$

For perfect resolution, this would always be 0 for the real events, but finite experimental resolution broadens this out to a gaussian-like distribution with a gaussian width $\sigma \cong 1.5^\circ$. For the eta experiment, this distribution was not used, since the mass distribution was equivalent and seemed more appropriate. However, in π^0 check runs performed as a consistency check on the experiment, the $\Delta\theta$-distribution was used for kinematical reasons (see Appendix). It should be emphasized that the mass and the $\Delta\theta_\eta$ calculations are essentially the same, and the goodness of the fit, found in Section V, indicates that the mass distribution used is a good one.

G. Calculation of the Resolution in Incident Photon Energy

A second quantity of importance in this experiment is the measurement of the incident photon energy, k_γ. The Monte Carlo program described in Section 3F is the best means available for

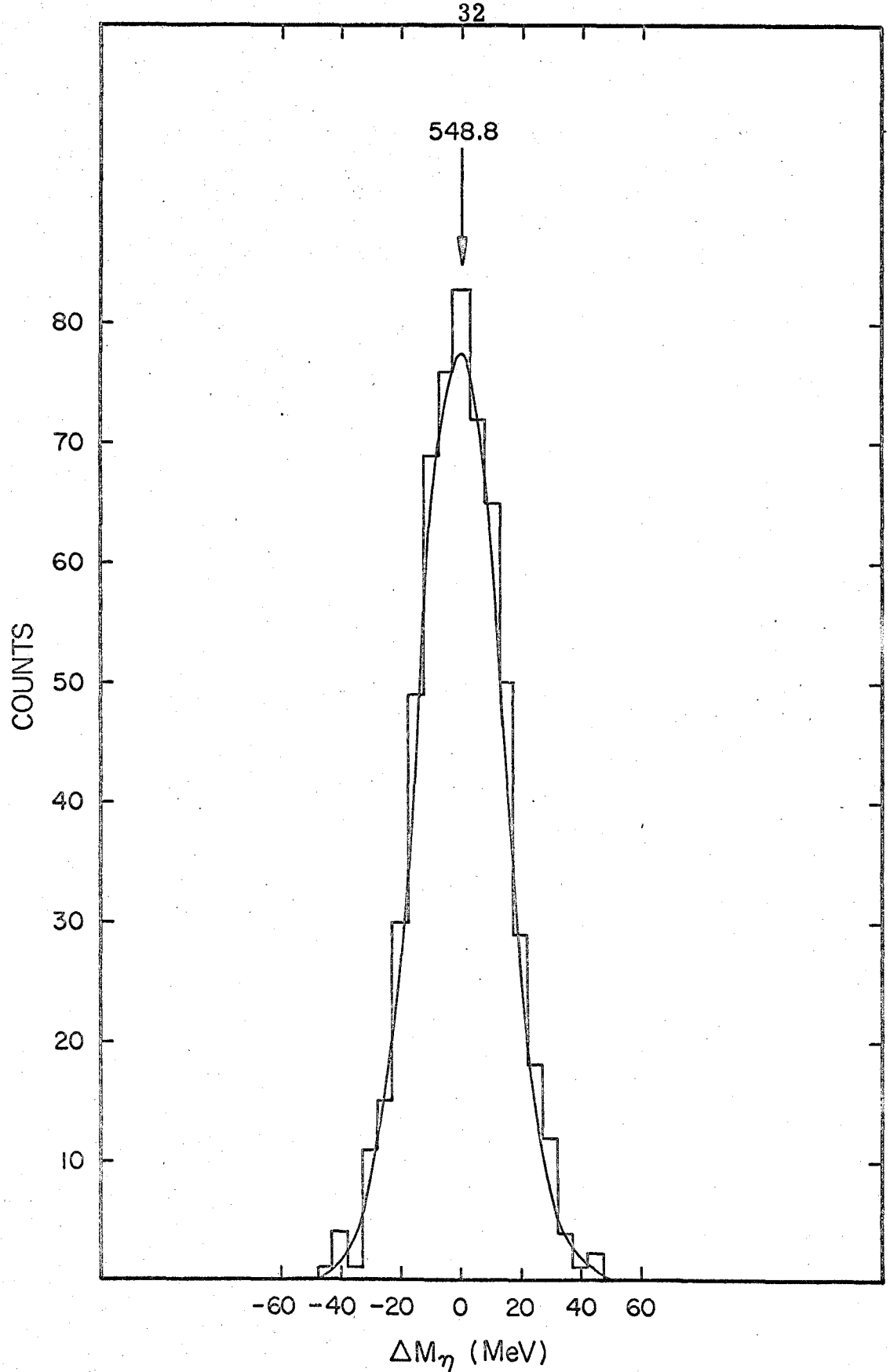

Figure 3.4 Monte Carlo calculation of mass resolution

calculating the experimental resolution in k, since it folds in all known effects to good approximations. The limitations of the method are statistical, which can be overcome by increasing the length of the computer time used.

To obtain the resolution in k, the computer generates an event of known k_o. The proton is allowed to multiply scatter and stop in the range chamber. The proton angle is changed by this process, and kinetic energy of the proton is changed to that of the central value of the aluminum plate of the range chamber in which it stopped. A new value of k is calculated from the new θ_p and T_p. The difference $k - k_o$ is then formed and falls into the distribution that forms the histogram. Figure 3.5 shows such a calculation. Figure 3.6 shows the value of the gaussian σ for the energies of interest in the experiment.

H. Calculation of the Geometrical Detection Efficiencies

To obtain a cross section from the processed data, the efficiency for detection of events produced in the target must be known. The Monte Carlo program measures the geometrical efficiency directly by keeping track of the number of successful events (i.e., events for which all particles enter the counter apertures) relative to the number of tries. In principle, one could allow the proton to go into all 4π in the center-of-mass, and let the two decay photons go into all 4π solid angle in the eta center-of-mass. This would measure the detection efficiency directly by counting the fraction of successful trials. In practice this does not work because it requires 10^6 attempts per success. Both the proton and the two-photon decay must be constrained to rather tight limits about the positions of the counters. Then the probability of success

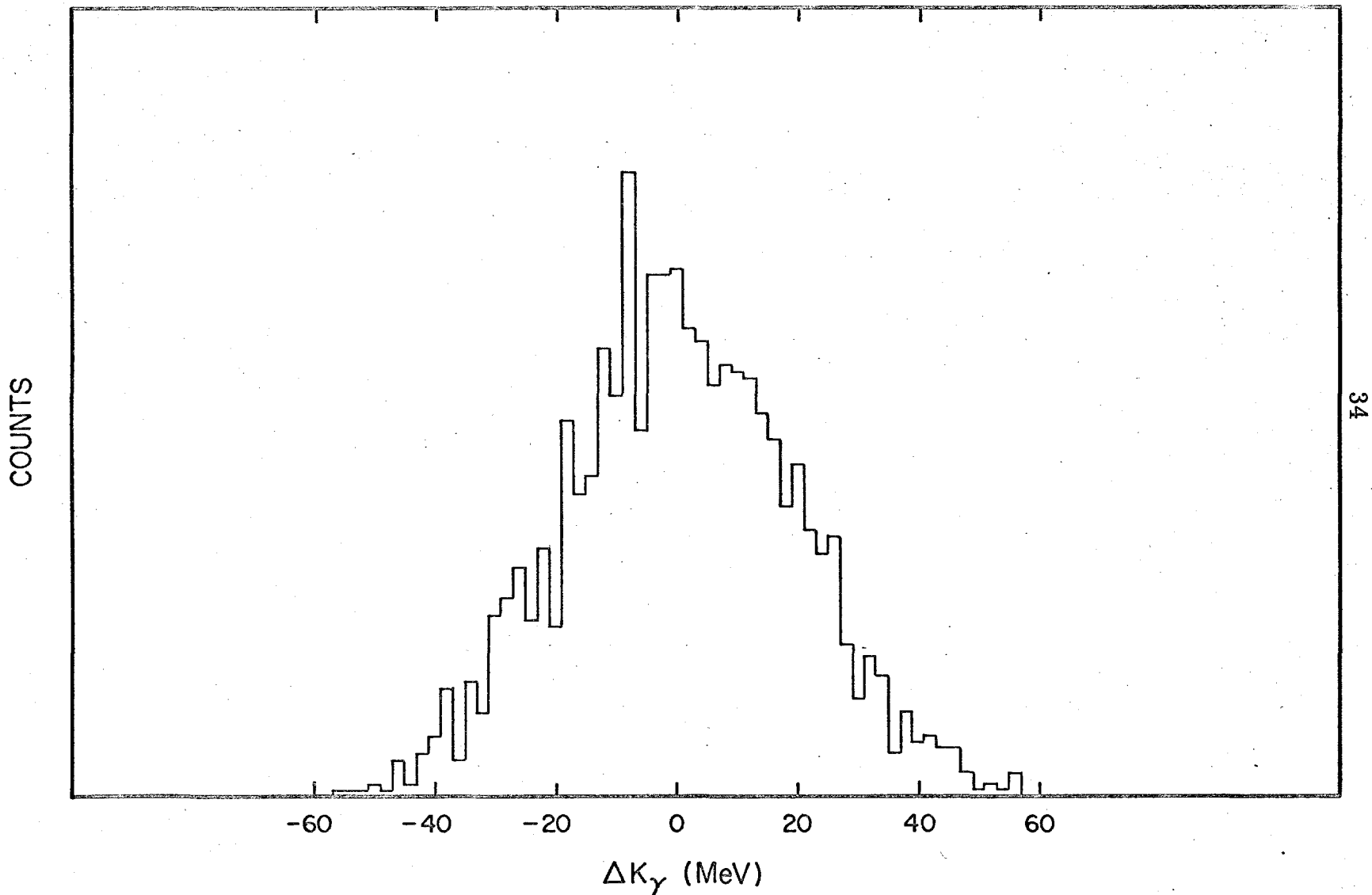

Figure 3.5 Monte Carlo calculation of k-resolution for k = 1025 Mev

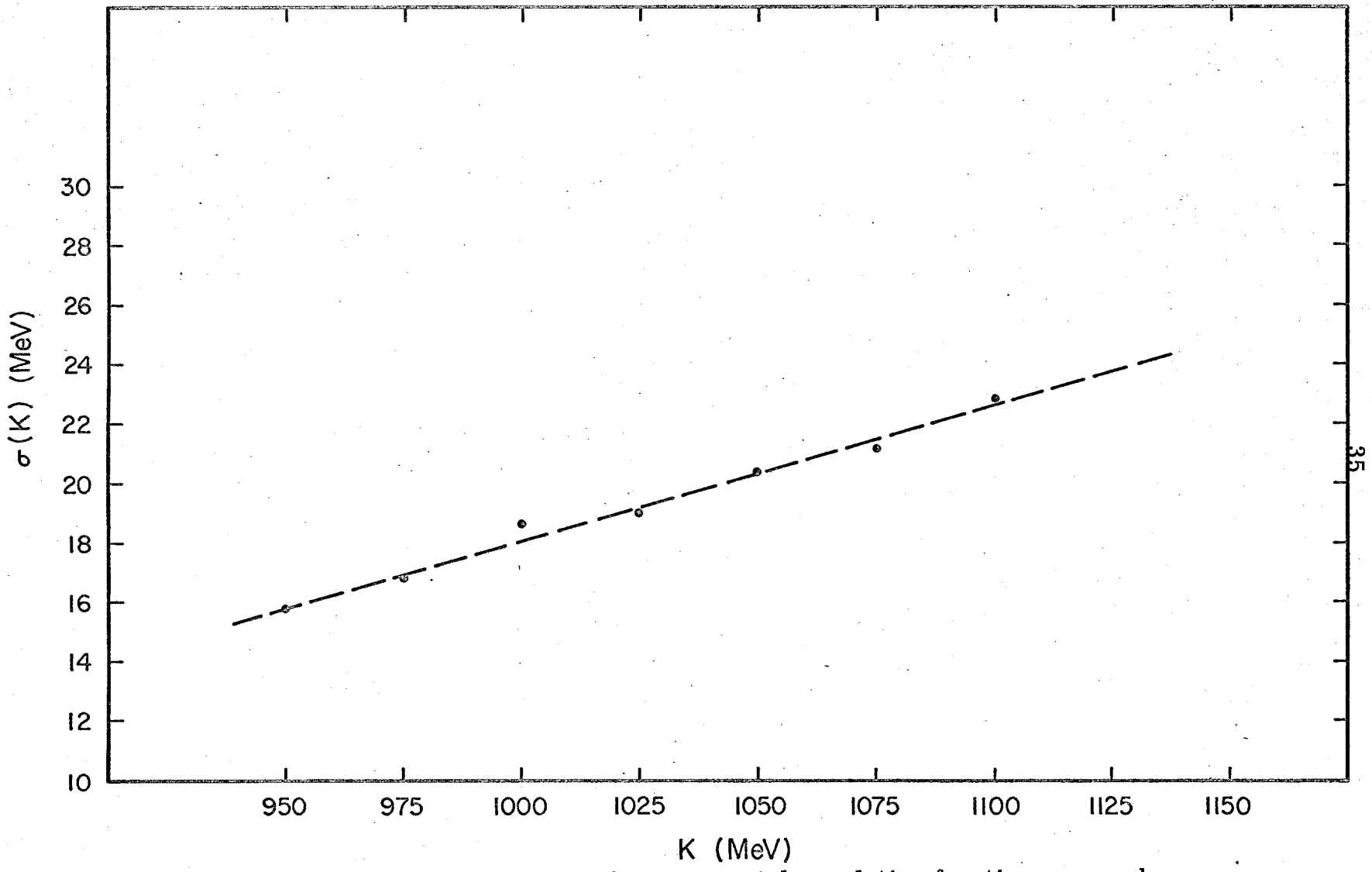

Figure 3.6 Gaussian width of experimental resolution function versus k

is good enough that a large number of events succeed in a reasonable amount of computer time. Care must be taken so that errors in the efficiency do not occur because of improper choice of limits.

The rate of successful events for the final form of the Monte Carlo program was 5000 events per minute at the peak efficiency, but averaged only about 500 events per minute when run over the finite target and all k and $\cos\theta^*$ asked of it. Since the experiment consists of about 500 events, 10 minutes of computer time would seem adequate to calculate the efficiency to good precision. In calculating the cross section, however, these efficiency curves must be broadened by the resolution of the experiment. To generate sufficient smoothness for the folding of the curves, the Monte Carlo program was run 30 minutes for all k and $\cos\theta^*$ required.

The geometrical efficiency is related to effective center-of-mass solid angles according to

$$\epsilon = \frac{\Delta\Omega^*_p}{4\pi} \frac{\Delta\Omega^*_{\gamma\gamma}}{4\pi}$$

where $\Delta\Omega^*_p$ is the proton telescope solid angle in the ηp center-of-mass and $\Delta\Omega^*_{\gamma\gamma}$ is the solid angle subtended by the overlap of the shower counters in the η center-of-mass (one shower counter being reflected through the origin in the η center-of-mass).

Attempts to calculate the solid angles and geometrical efficiencies analytically were abandoned because of the difficulties involved. The resulting integrals required numerical methods and would have used considerably more computer time than the Monte Carlo program needed. Figure 3.7 shows the results of the calculations for the three settings of this experiment.

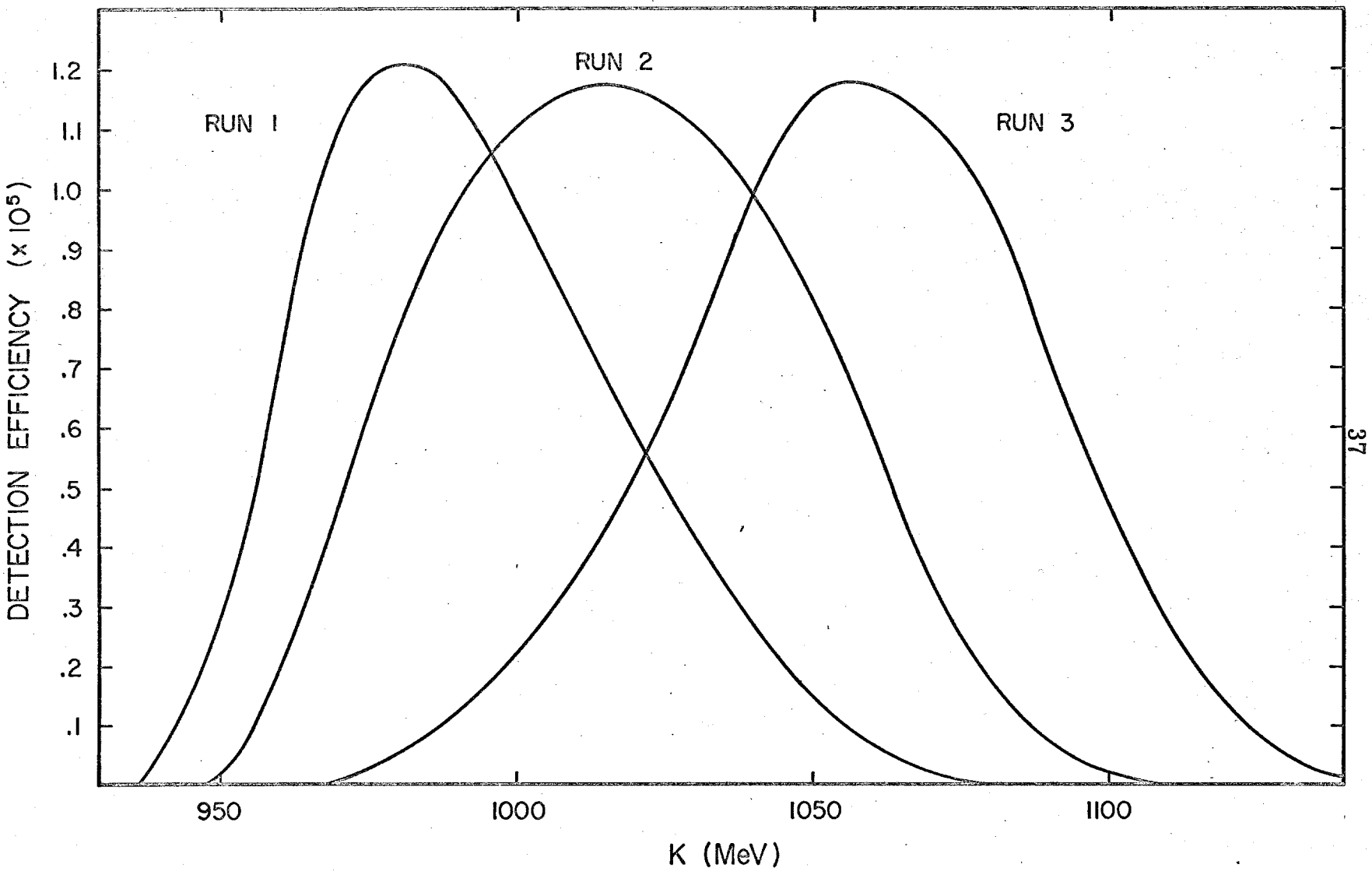

Figure 3.7 Geometrical detection efficiency for the three runs

IV. BACKGROUND CONTAMINATION

A. Identification of Backgrounds

In Section III-F the calculation of the expected distribution in mass is described. Measurement of this quantity provides a good means of separating good events from background events. If one assumes the following process occurs:

$$\gamma + p \rightarrow p + X \quad (X \hookrightarrow 2\gamma)$$

and asks for the value of the mass of X, one finds that

$$M_x^2 = \left(P_p \left(\cos\theta_p + \frac{\sin\theta_p}{\tan\theta_\eta}\right) - T_p\right)^2 - P_p^2 \left(\frac{\sin\theta_p}{\sin\theta_\eta}\right)^2$$

where P_p = proton momentum

T_p = proton kinetic energy

θ_p = proton lab angle

and θ_η = eta lab angle .

T_p is obtained by the range in the chambers, θ_p by the angle of the track in the two thin foil spark chambers, and θ_η is obtained from the points of conversion of the decay photons in the scintillator hodoscope. For the process

$$\gamma + p \rightarrow p + \eta^o \quad (\eta^o \hookrightarrow 2\gamma)$$

then the distribution of events should be peaked at the mass of the eta, 548.8 Mev. The shape of the distribution for the mass is the

subject of Section III-F. The shape of the background is determined by the physical geometry of the counters and, to a lesser degree, by the background processes involved. Background events give a broad distribution because the events are not correlated to any definite mass and tend to come from many-particle final states.

It is felt that most of the background events come from

$$\gamma + p \rightarrow p + \pi^o + \pi^o$$

with each π^o decaying into two photons. Only two of the four photons are needed to trigger the system. The mass of the π^o-pair system is completely lost because two of the four photons are not seen and the calculated mass will fall into a wide distribution characteristic of the background distribution. Figure 4.1 shows the mass plot for all events surviving the scanning criteria. The calculation of Section III-F shows that the good events should all lie in a region 80 Mev wide centered about the eta mass. The events which lie outside this 80 Mev bin come from backgrounds and provide a good sample of data concerning the background contaminations.

The sources of background are mainly two known processes, and Section IV-B shows that two processes appear to account for all the major contributions to the background. The most important background contamination comes from photoproduction of π^o-pairs,

1) $\gamma + p \rightarrow p + \pi^o + \pi^o \rightarrow p + 4\gamma$.

A second process which can contribute backgrounds is

2) $\gamma + p \rightarrow p + \eta^o \rightarrow p + 3\pi^o \rightarrow p + 6\gamma$

and a third, less important process, similar to 2) is

3) $\gamma + p \rightarrow p + \eta^o \rightarrow p + \pi^o + 2\gamma \rightarrow p + 4\gamma$.

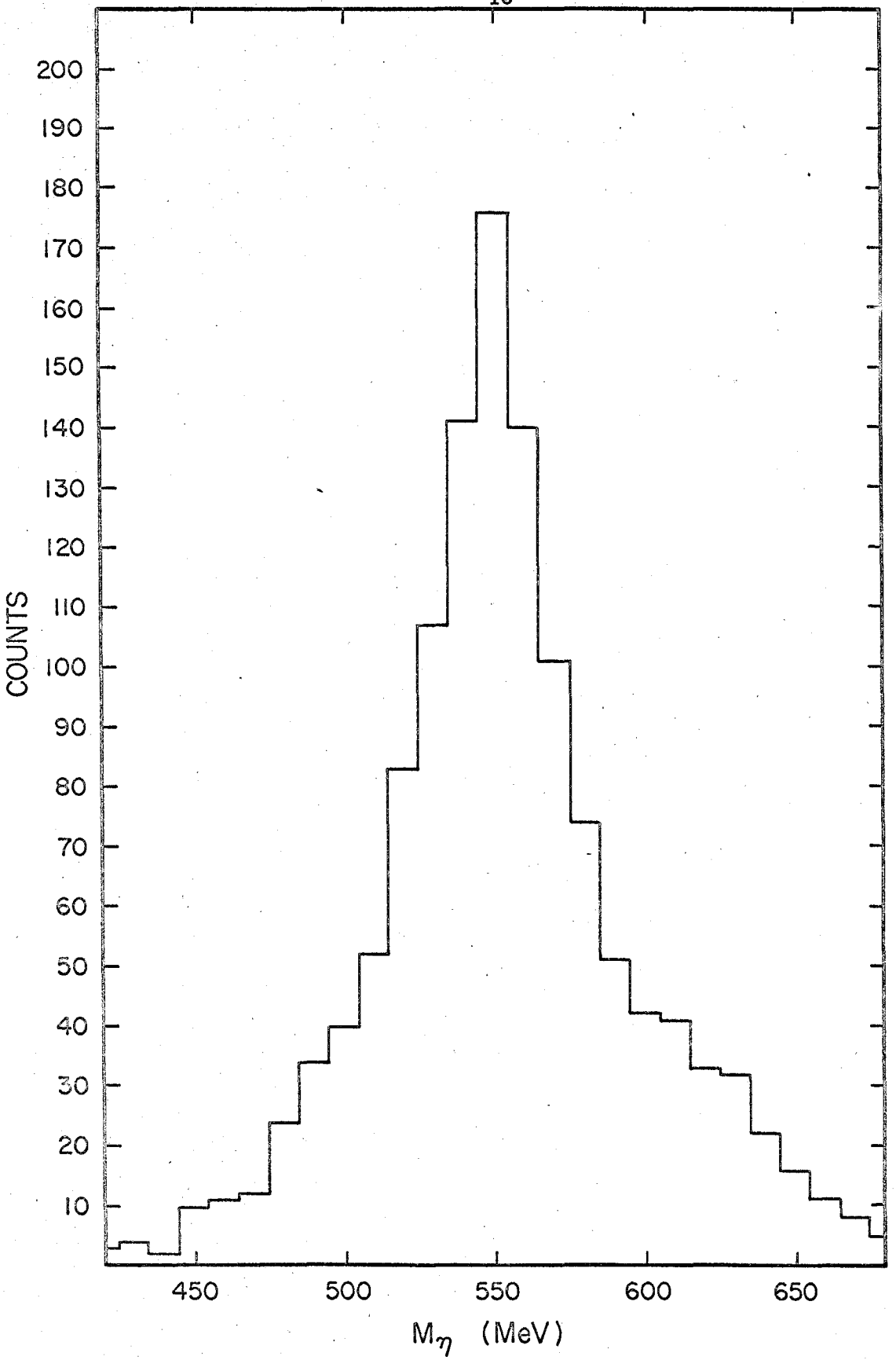

Figure 4.1 Distribution of mass of the two photons for all events. See Figure 4.5 for comparison with background runs.

The second and third processes would be of interest if they could be identified, but the decay into six or four photons in the final state relaxes the kinematical constraints on the particles seen and consequently produces events which lie outside the 80 Mev bin of the mass distribution. These decay modes must therefore be treated as backgrounds. Normal π^0 photoproduction cannot contribute to the backgrounds because the angles defined by the counters kinematically exclude triggers from π^0 photoproduction. The calculation of the contamination is the subject of two sections in the Appendix. Comparison of the calculations with the data will be found in the next section. The corrections that are applied to the data are also described in the next section.

B. Comparison of Calculated Backgrounds with Observed Backgrounds

Figure 4. 1 in Section IV-A shows the distribution in mass of the two photon object. Examination of this histogram shows that the selection of events is not pure in η mesons, but contains some contamination from background processes. This section describes how these backgrounds are identified and how they are treated so that the resulting data can be used to evaluate the cross section.

A pure selection of photoproduced eta mesons would result in a distribution of the mass of all events being centered about 549 ($\pm$ 1) Mev and being gaussian in shape. No events would fall outside a bin with limits $\pm$ 40 Mev of the central value. The histogram obtained from the experiment shows a gaussian peak centered at 549. 9 Mev, but sitting on top of a broad background.

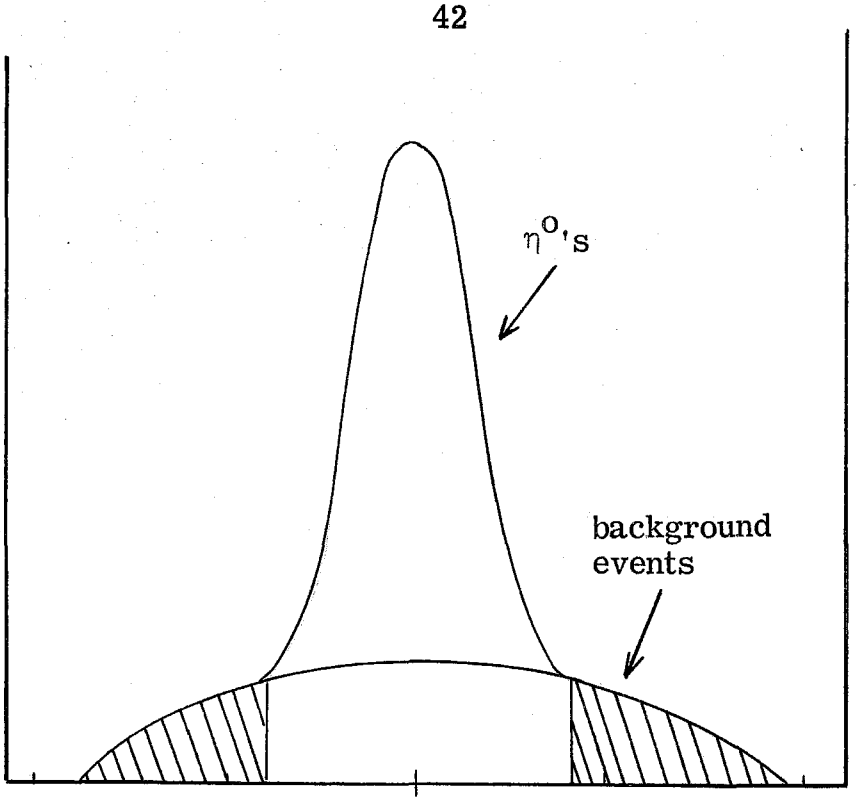

The events which fall into the shaded regions are clearly from background processes, and these provide a good sample of data which can be compared to the background calculations.

In addition to measuring the mass of the two-photon object, the analysis program calculates the incident photon energy, k, for each event. The distribution in k for all events is needed in order to calculate the photoproduction cross section. However, background events must be eliminated before this can be done. Calculation of the resolution in mass shows that no η-events will result in a measured mass outside the limits 549 ± 40 Mev. Thus, events for which the mass ≤ 509 Mev or for which the mass ≥ 589 Mev cannot have resulted from η^o photoproduction. These events are clearly background events and are eliminated at this point. However, background events still exist for which the measured

mass falls inside the limits 509 Mev $\leq$ mass $\leq$ 589 Mev. Since all kinematical information has been used at this point, these events cannot be isolated from the η-events. A different approach is used to eliminate these background events.

If one knows how background processes are distributed in k, and if one knows how many events from background processes are present, one can subtract the background events from the k-distribution of all events, thus obtaining the k-distribution of the η-events.

The question of the shape of the k-distribution from background processes was approached from two directions. First, one has a large selection of background events available from the data. Those events for which the mass $\leq$ 509 Mev or mass $\geq$ 589 Mev are clearly background processes. If one assumes that the shape of the k-distribution of the background processes is the same for mass $\leq$ 509 Mev and mass $\geq$ 589 Mev, then one expects that background events for which 509 Mev $\leq$ mass $\leq$ 589 Mev will have the same k-distribution. This assumption was checked and appears good. The k-distribution of the events from the wings of the mass distribution are plotted in Figures 4.2, 4.3, and 4.4, according to runs of the experiment. The three different runs were taken with the counters located in different places in the lab, and therefore the three k-distributions differ slightly.

A second approach was taken as a check on the shape of the k-distributions of the background events. Calculation of these distributions seemed a reasonable thing to attempt since the shape of the distributions is mostly determined by the geometry of the experiment and only to a lesser degree by the models assumed for the production of background events. The first two processes

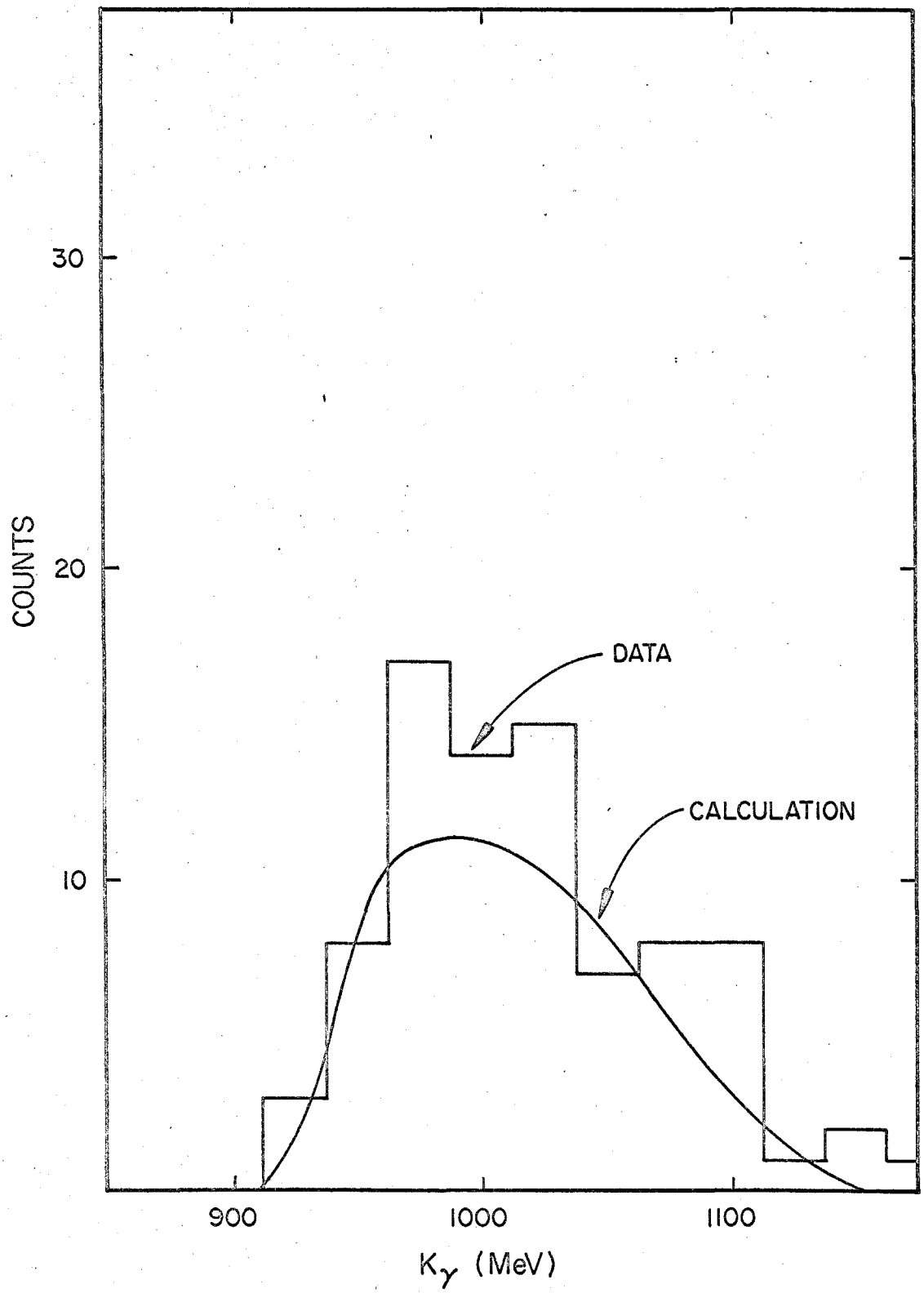

Figure 4.2 Comparison of data with background calculation for Run 1. Data is obtained from those events which lie in the wings of the mass plot.

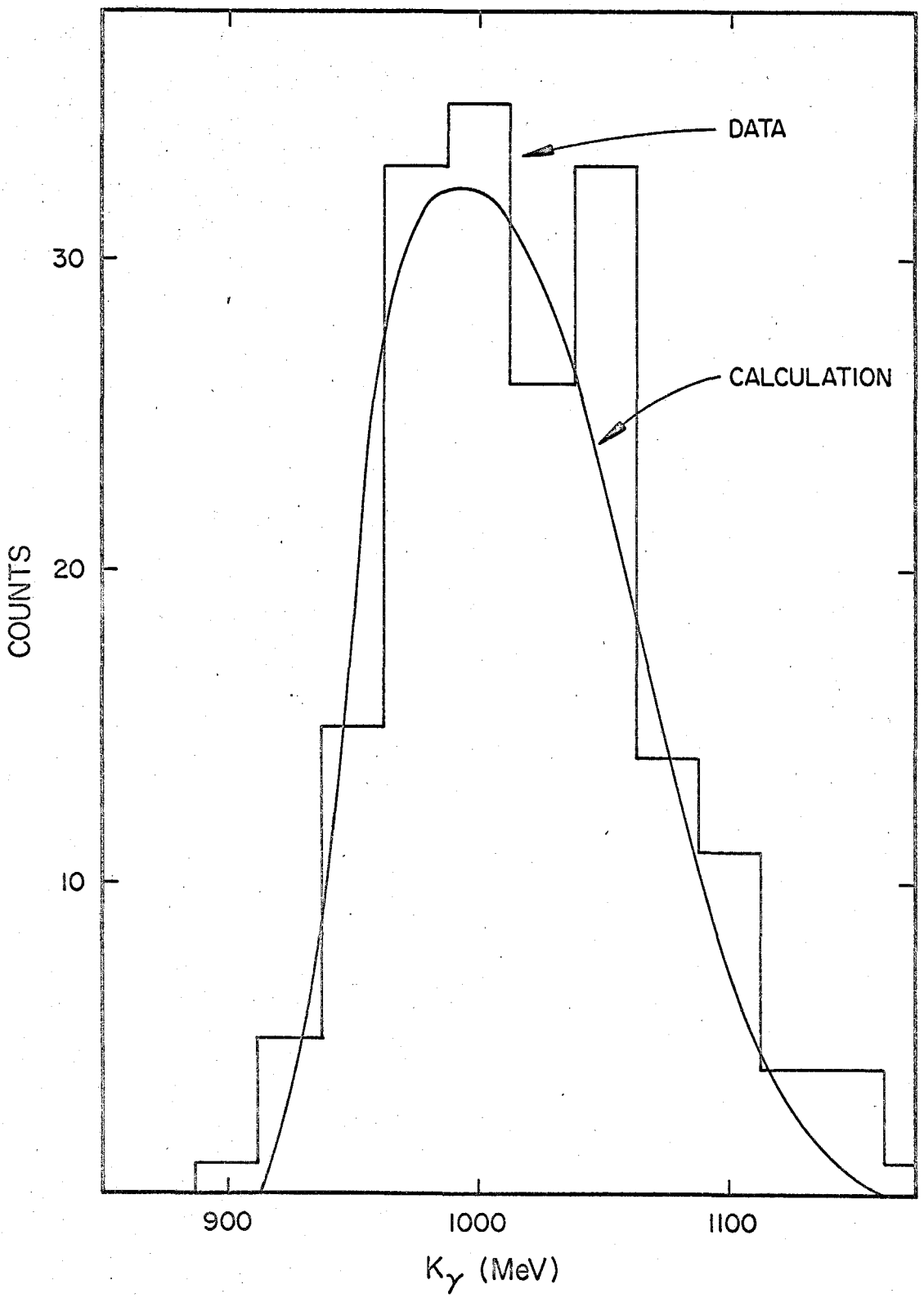

Figure 4.3 Comparison of data with background calculation for Run 2. Data is obtained from those events which lie in the wings of the mass plot.

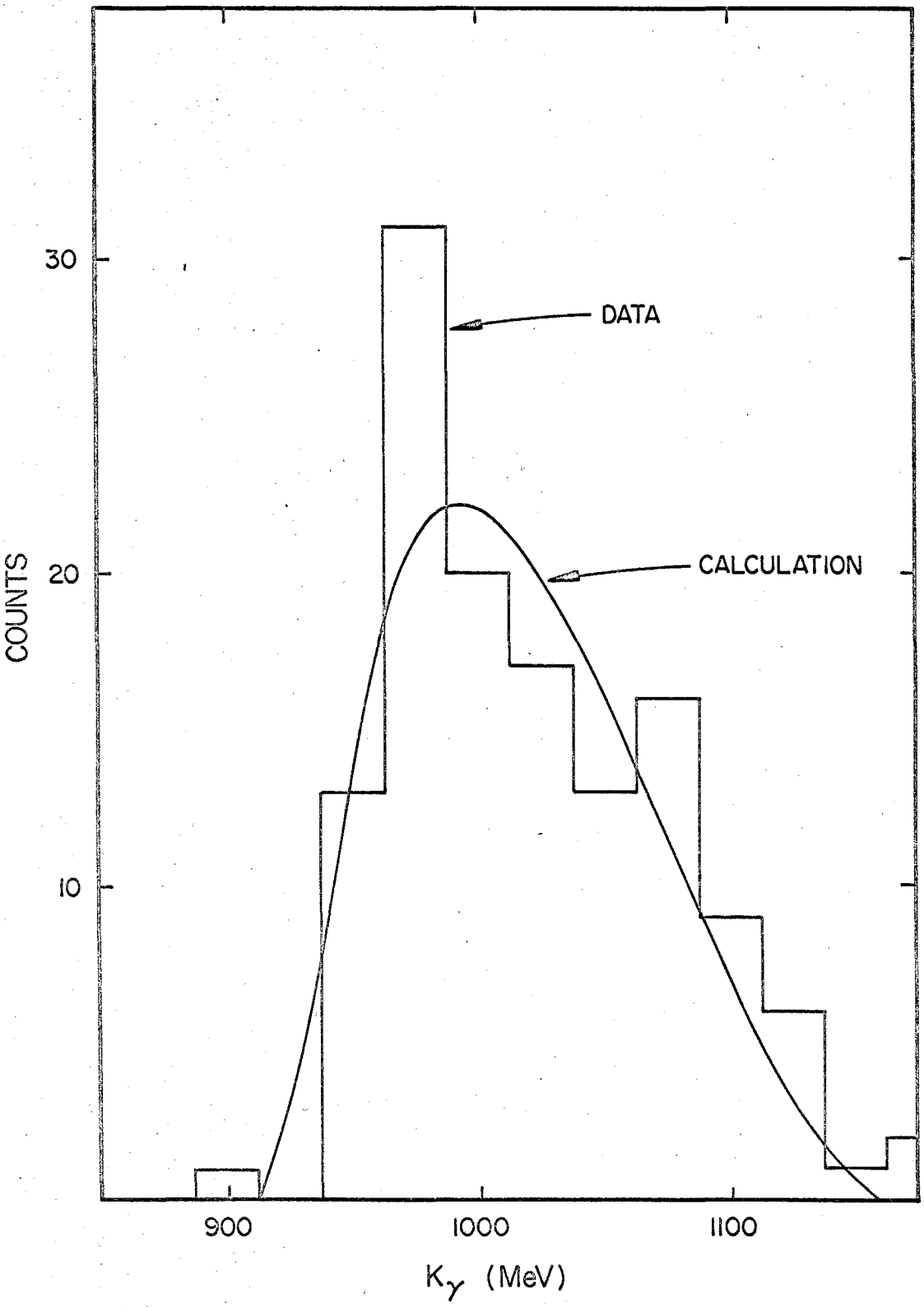

Figure 4.4 Comparison of data with background calculation for Run 3. Data is obtained from those events which lie in the wings of the mass plot.

mentioned in Section IV-A were taken as the sources of backgrounds and the k-distribution of the resulting events was calculated. In this calculation only the total π^o-pair cross section was taken as an adjustable parameter. The details of the calculation are contained in the Appendix, Sections VII-H and VII-I.

Figures 4.2, 4.3, and 4.4 show the agreement achieved between the data and the calculation. The histograms are the data, and the curves are the results of the calculated backgrounds added together. The π^o-pair cross section was taken to be flat in energy (for the range 600 Mev $\leq k_\gamma \leq$ 1100 Mev) and the amount needed for a fit was

$$\sigma_T \begin{cases} \tilde{=} 42 \ \mu\text{barns} & \text{for Run 1} \\ \tilde{=} 46 \ \mu\text{barns} & \text{for Run 2} \\ \tilde{=} 47 \ \mu\text{barns} & \text{for Run 3} \end{cases} .$$

These values for the π^o-pair cross section agree reasonably with values obtained in $\pi^+\pi^-$-photoproduction. Recent data available from Stanford shows that the $\pi^+\pi^-$ total cross section rises rapidly from threshold to a maximum of 75 μbarns at k_γ = 650 Mev, and drops off uniformly to 45 μbarns around 1 Bev. Perhaps the only conclusion that should be drawn from these calculations is that π^o-pair production seems to account for the majority of the background, and together with the addition of the $3\pi^o$ decay of the η, no significant discrepancies are found. The magnitude of the cross section used to obtain a fit is not considered to be a good measurement. Its general agreement with the data and the charged-π-pair cross section is presented only to lend credibility to the explanation of the backgrounds.

C. Background Runs

For the purpose of background calculations, it was desirable to have a direct measure of the background contamination. This was simple to do by moving the counters to angles kinematically not allowed for the decay photons of the eta.

When the eta decays into two photons, the opening angle in the lab between the photons has a minimum value that occurs for the symmetrical decay. (i. e., when the two photons are emitted at 90^{o} to the η-direction in the eta center-of-mass).

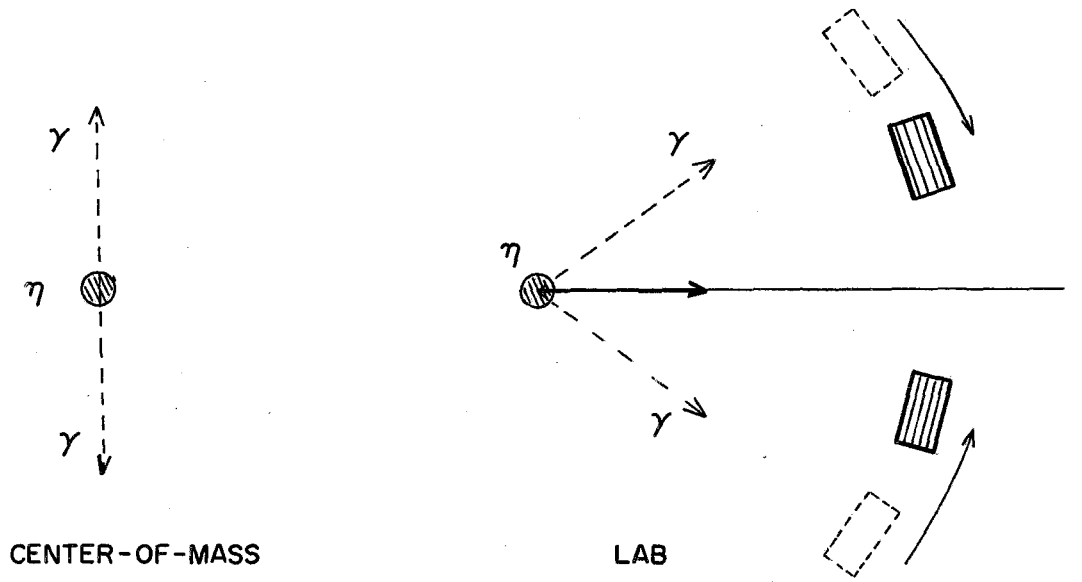

Thus, if the two shower counters are placed inside this minimum opening cone, it is impossible for both photons to be seen. In this simple way, the good events are eliminated, and only the background processes remain. Figure 4. 5 shows the mass distribution for the events obtained from these "off-kinematics" runs. This should be compared with Figure 4. 1 where a noticeable η-peak was observed.

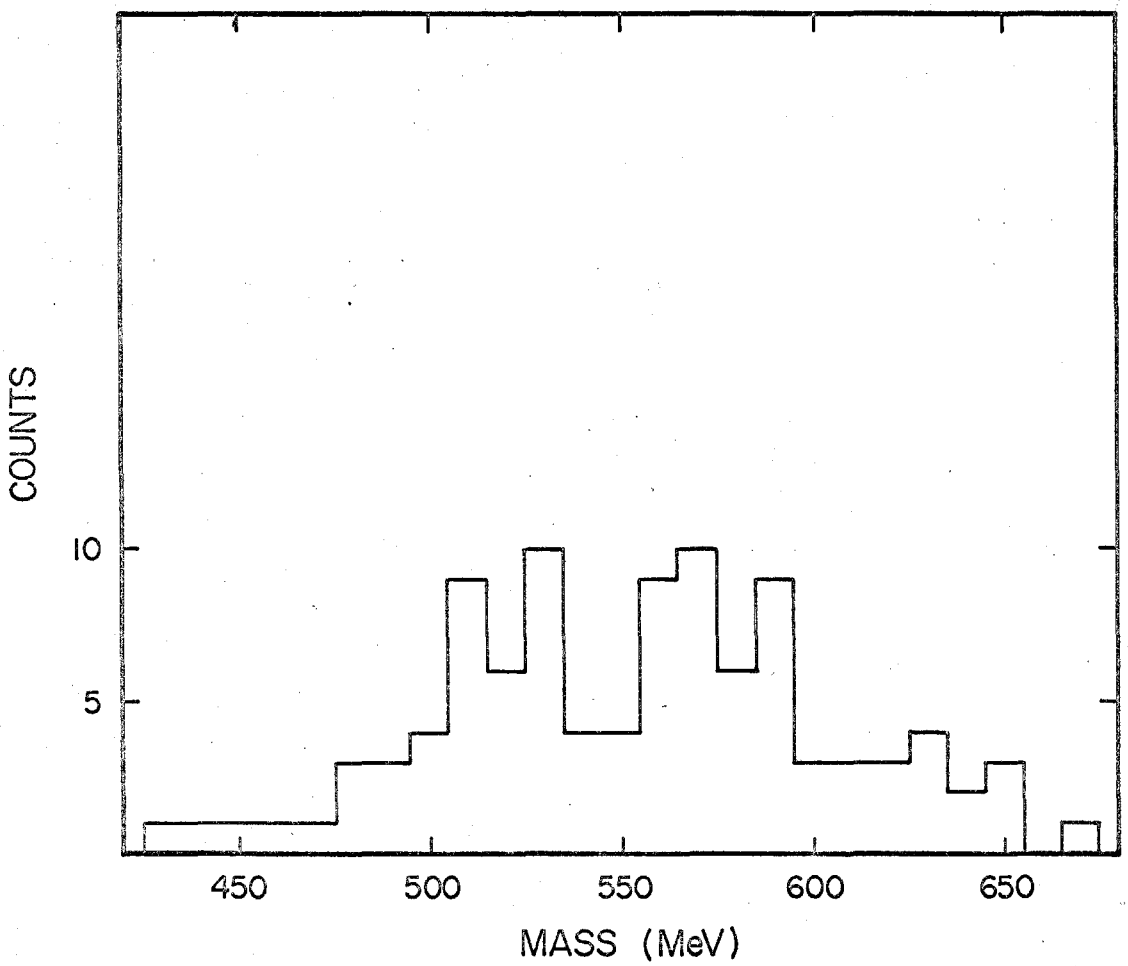

Figure 4.5 Distribution of mass of the two photons for off-kinematics runs. This should be compared to the distribution in Figure 4.1.

Here no such peak exists, and a general background remains similar to the background seen in Figure 4. 1.

If one takes these events and plots the distribution in apparent k, the histogram in Figure 4. 6 is obtained. The smooth curve is the calculation based on π^o-pair production and $\eta \rightarrow 3\pi^o$ decay, the same as that found in Figures 4. 2, 4. 3, and 4. 4. The value of the π^o-pair cross section used in the calculation was

$$\sigma_T = 45 \ \mu\text{barns} \ .$$

This value was chosen the same as that needed to fit the three data runs of this experiment. There are no other adjustable parameters in the calculation.

The success of these models and the good agreement with the data allow a subtraction to be performed. The shape of the subtracted distribution was taken from the calculation, but could have been taken from the data, since agreement is good. The amount of the subtraction was scaled so that the number of events subtracted was equal to the number of events under the η-peak.

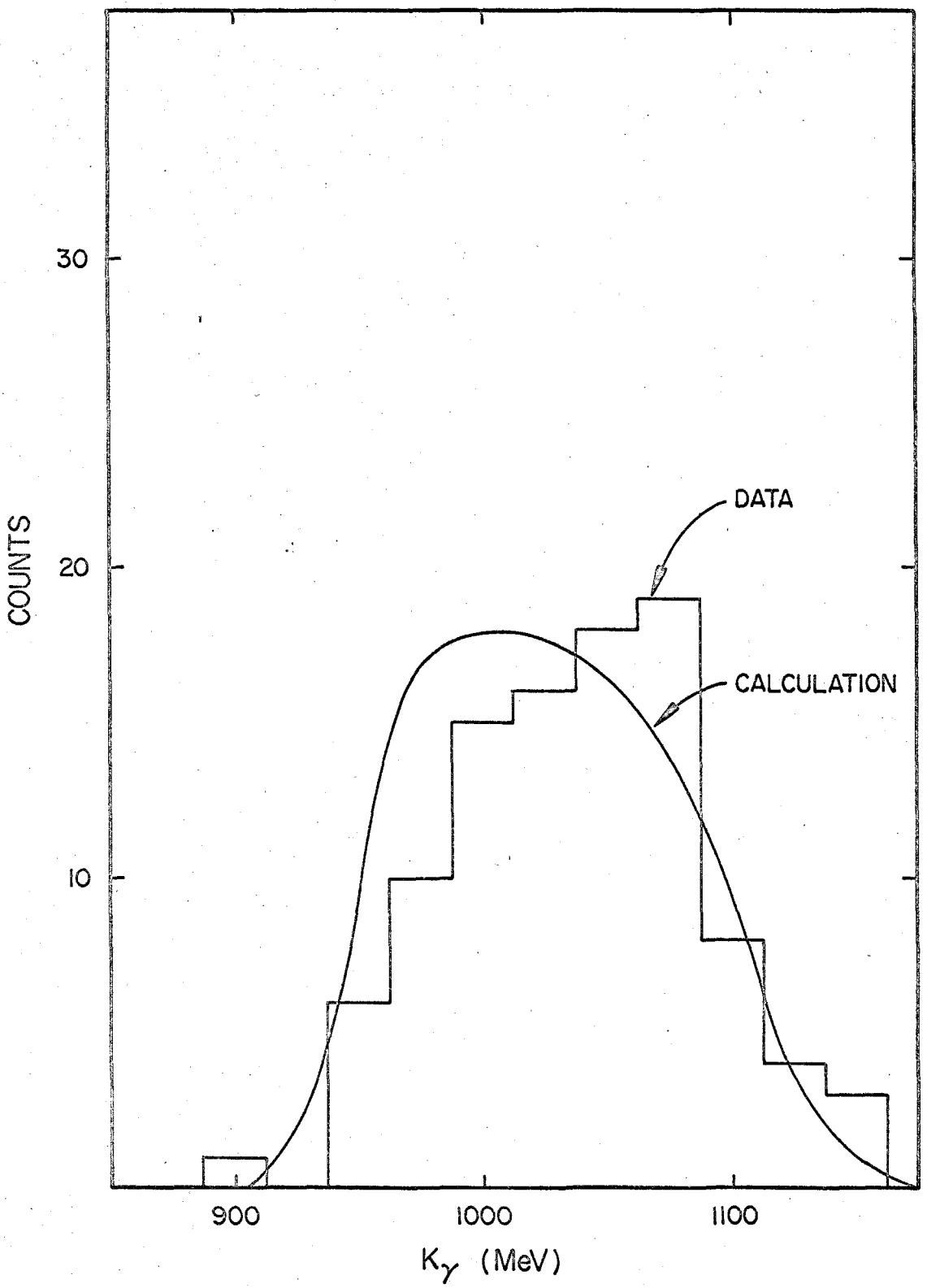

Figure 4.6 Comparison of data with background calculation for off-kinematics runs. Data is all events from off-kinematics runs.

V. EXPERIMENTAL RESULTS: CROSS SECTION, MASS OF ETA, EXPERIMENTAL WIDTH OF ETA

A. Cross Section Evaluation

The general form for calculating the counting rate in this experiment is

$$C(k) = \frac{d\sigma}{d\Omega}(k)\, N_p \cdot N_\gamma(k) \cdot \epsilon(k) \cdot \Gamma \cdot \alpha \cdot 4\pi \cdot \Delta k$$

where

$C(k)$ = number of events generated in interval $k \pm \Delta k/2$

$N_\gamma(k)$ = number of photons of energy k per unit interval in k

N_p = number of protons contained in target per cm^2

$\epsilon(k)$ = efficiency for detection of event initiated from photon of energy k

Γ = branching ratio into mode of interest

α = factor arising from systematic effects .

A limitation in the experiment is the experimental resolution in k. What one obtains experimentally is not the distribution C(k), but a different distribution C'(k) which is C(k) broadened by the resolution in k:

$$C'(k) = 4\pi\alpha\Gamma N_p \int \frac{d\sigma}{d\Omega}(t) N_\gamma(t) \cdot \epsilon(t)\, \exp(-(t-k)^2/2\sigma^2(t))\, dt \cdot \Delta k/\sqrt{2\pi}$$

Since the cross section is the unknown, one is forced to approximate this by

$$C'(k) \cong 4\pi\alpha\Gamma N_p \overline{\frac{d\sigma}{d\Omega}}(k) \left\{N_\gamma(k)\, \epsilon(k)\right\} \Delta k \ .$$

For constant cross section, this is exact. But where there are variations of cross section this gives the cross section broadened by the resolution in k.

$$\overline{\frac{d\sigma}{d\Omega}}(k) = \frac{C'(k)}{F(k)} \cdot \frac{E_o}{4\pi\alpha\Gamma \cdot N_p \cdot W \cdot B \cdot \Delta k \cdot \delta^2}$$

where E_o = the synchrotron endpoint in Mev,

W = quantameter constant (=1.17 $\times$ 10^{13} Mev/BIP),

Δk = energy bin (= 25 Mev),

N_p = number of protons in target (= .686 $\times$ 10^{24} per cm^2),

δ^2 = photon conversion factor (= .615),

B = number of BIP's,

Γ = branching ratio for $\eta^o \rightarrow 2\gamma$ (= .386),

and $F(k)$ = $B(k)\, \epsilon(k)/k$ ($B(k)$ is the bremsstrahlung function).

B. Systematic Effects

There exist in all experiments of this type numerous small corrections to the measurement. In most cases these corrections are, taken singly, small enough to be neglected as far as the overall effect on the experiment is concerned. Taken collectively, however, the added effect is not negligible. It is the purpose of this section to list the effects in this experiment and corresponding to each, the size of the error. The systematic errors are given in Table 5.1.

TABLE 5.1

Systematic Effects

	Effect	Loss (%)	Remarks
I.	Electronic Inefficiencies		
	Spark Chamber Dead Time	.5	
	SP - 1	.6	
	SP - 2	.2	
	SP - 3	.2	
	PBL - 1	-	negligible
	PBL - 2	-	negligible
	V1	.5	
	V2	.5	
II.	Counter Inefficiencies		
	Photon Pre-conversion*	6.5	each 3.2%
	Shower Counter Inefficiencies**	9.0	each 4.5%
	Proton Counter Inefficiencies	-	negligible
III.	Scanning Inefficiencies		
	Event Oversight	-	small
	Multitrack Confusion	4.1	
IV.	Miscellaneous		
	Nuclear Interactions	.8	
	Mass Cutoff	.5	
	Bubbling in Target	-	estimated small
	Total Corrections	21.5%	Loss

* Photons which convert in the target walls or in air before reaching the veto counters are lost.

** Pulse height requirement introduced in the analysis is responsible for this inefficiency. The electronic bias was set low enough so that it introduced negligible inefficiencies.

They are classified into four general groups; electronic inefficiencies, counter inefficiencies, scanning inefficiencies, and miscellaneous effects.

C. Eta Photoproduction Cross Section

Table 5.2 lists the relevant parameters used in evaluating the cross section. The cross section listed in the last column contains the systematic corrections of the previous section. Figures 5.1, 5.2, and 5.3 show the k-distribution of the events after subtraction. The solid line is the k-dependence of the acceptance of the apparatus, scaled to give an approximate fit. The ratio of the histogram to the curve shows how the cross section varies in k. The cross sections obtained from the individual runs are listed in the last column of Table 5.2 and are displayed in Figure 5.4. Figure 5.5 shows the combined results of the three runs of this experiment. The combined values for the cross section are given in Table 5.3.

D. Independent Measurement of the Eta Meson Mass; Limit on the Width of the Eta Meson

The measurement of the mass of the eta is possible because of the overdetermination of the kinematical parameters. Previous experiments, mostly bubble chamber data, have yielded the result $548.9 \pm .5$ Mev, which was the value assumed for the analysis of this experiment. This piece of information has been used as a consistency check on the experiment, but it is felt that an independent measurement of the eta mass is worth reporting.

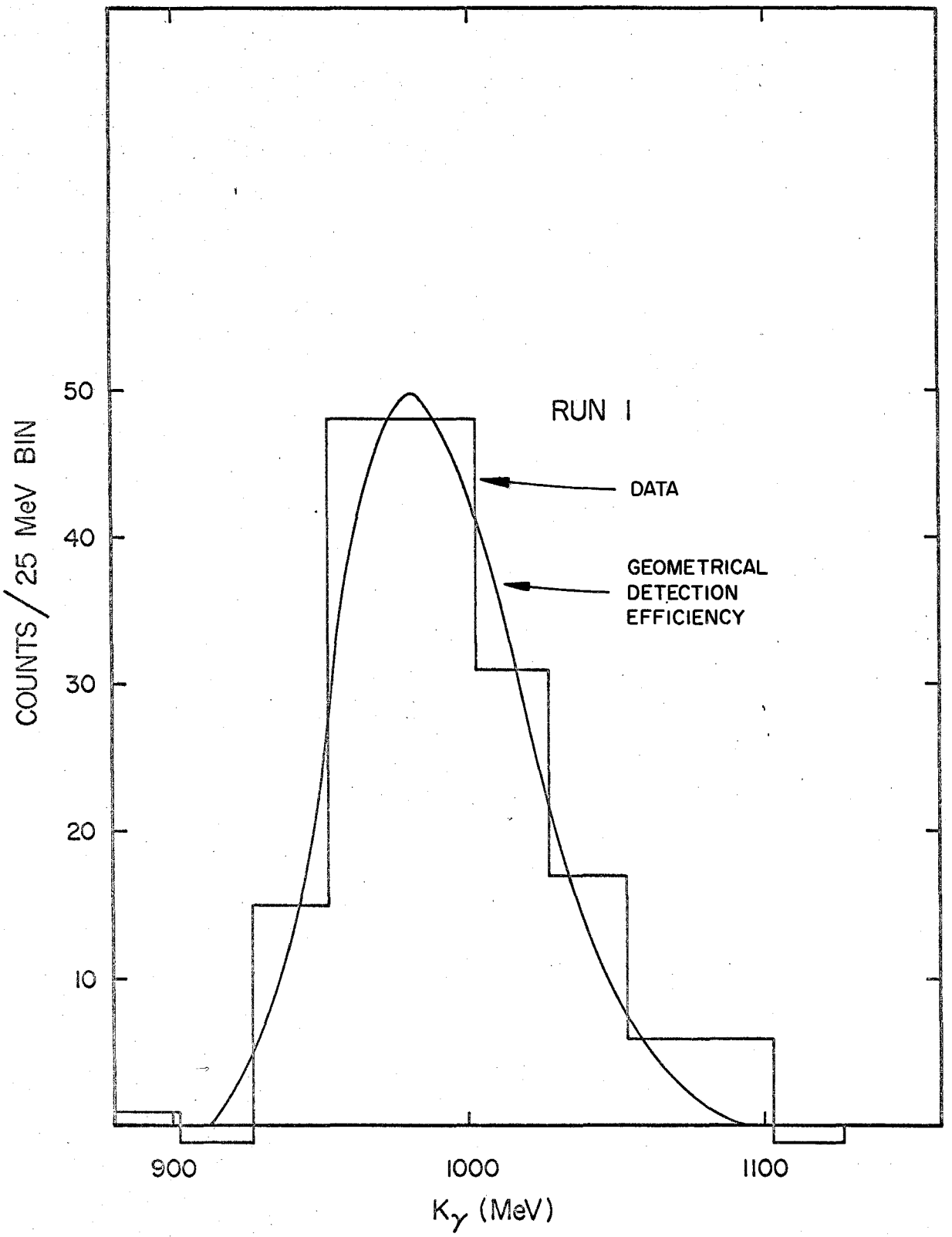

Figure 5.1 Distribution of events in k for Run 1, after background subtraction

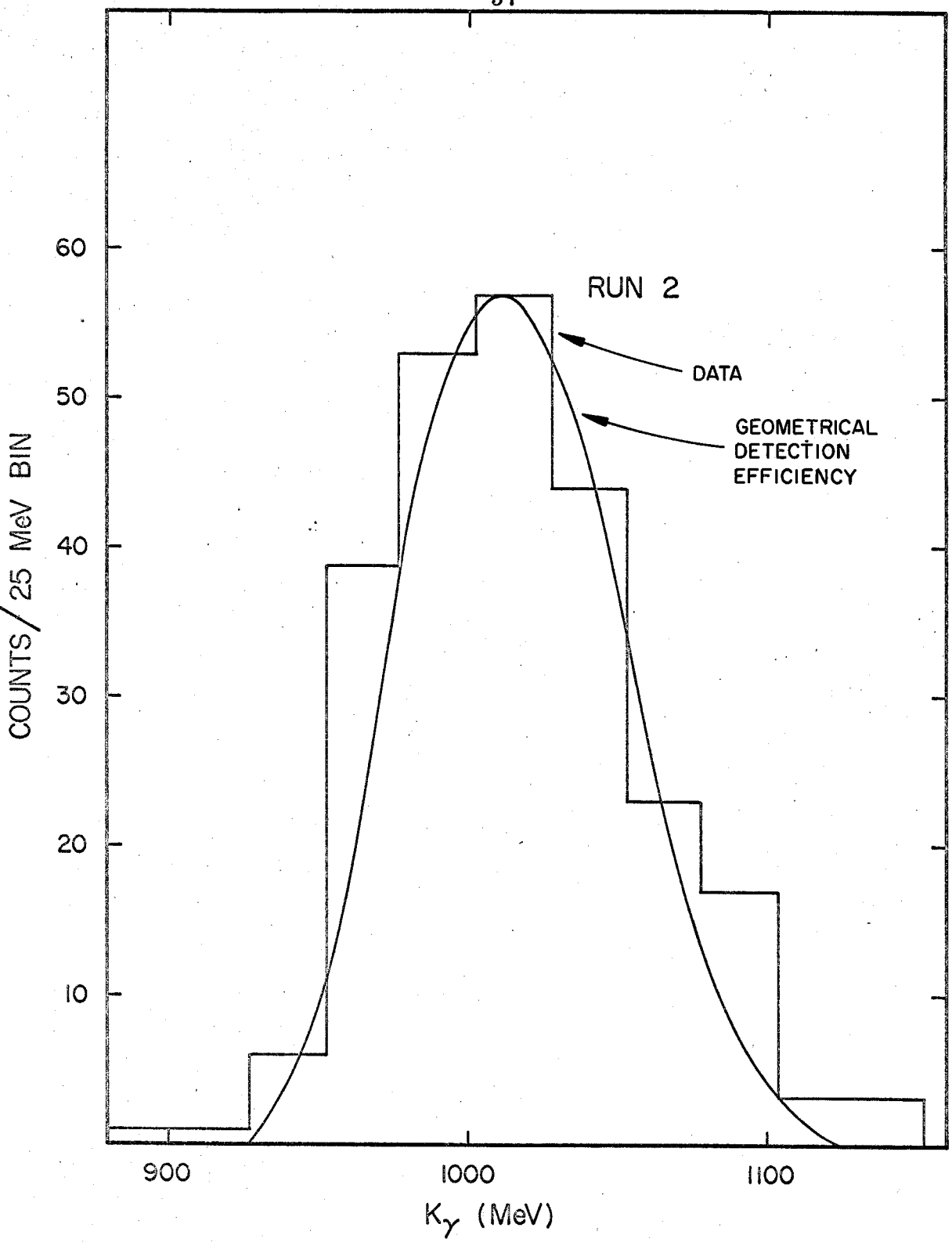

Figure 5.2 Distribution of events in k for Run 2, after background subtraction

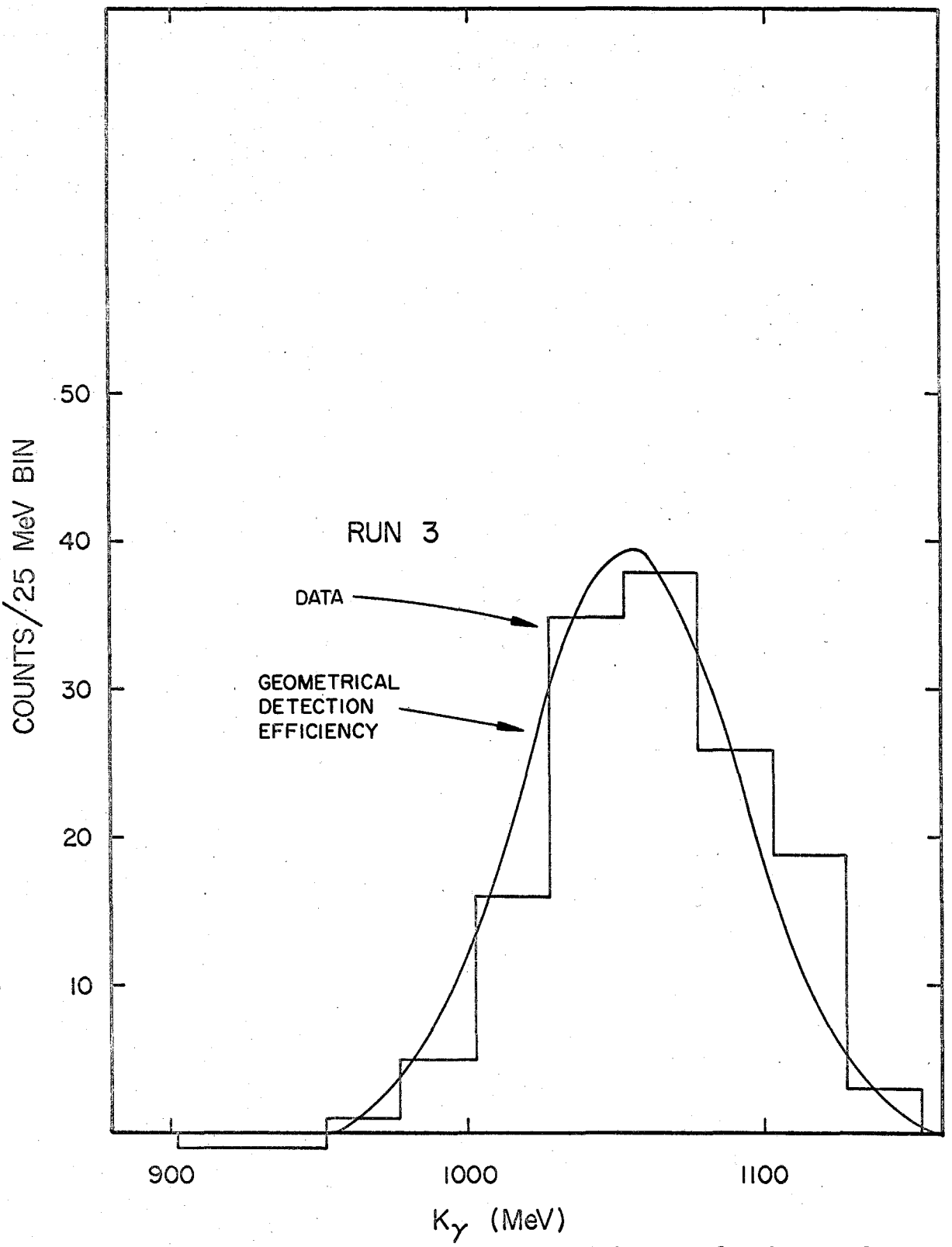

Figure 5.3 Distribution of events in k for Run 3, after background subtraction

TABLE 5.2

Parameters Involved in Cross Section Evaluation

Run	k_o Mev	E_o Mev	BIPs*	k Mev	F(k)	Unsubtracted Counts	Subtracted Counts	$\frac{d\sigma}{d\Omega}$ ($\frac{\mu b.}{Ster.}$)
1	975	1125	6.70 ($\times 10^4$)	940	2.186 ($\times 10^{-9}$)	22	15	.248 ± .078
				965	7.05	57	48	.245 ± .040
				990	8.39	57	48	.206 ± .033
				1015	4.97	39	31	.206 ± .043
				1040	2.41	24	17	.254 ± .074
2	1025	1200	10.8 ($\times 10^4$)	940	.557	19	6	.257 ± .187
				965	3.72	67	39	.254 ± .055
				990	7.79	82	53	.163 ± .029
				1015	8.92	82	57	.152 ± .025
				1040	7.06	66	44	.149 ± .029
				1065	3.74	36	23	.146 ± .039
3	1075	1200	6.2 ($\times 10^4$)	990	1.65	25	5	.126 ± .126
				1015	4.30	36	16	.156 ± .060
				1040	7.09	52	35	.204 ± .043
				1065	7.46	51	38	.212 ± .041
				1090	5.02	35	26	.216 ± .050

* Note: 1 BIP = 1.17×10^{13} Mev

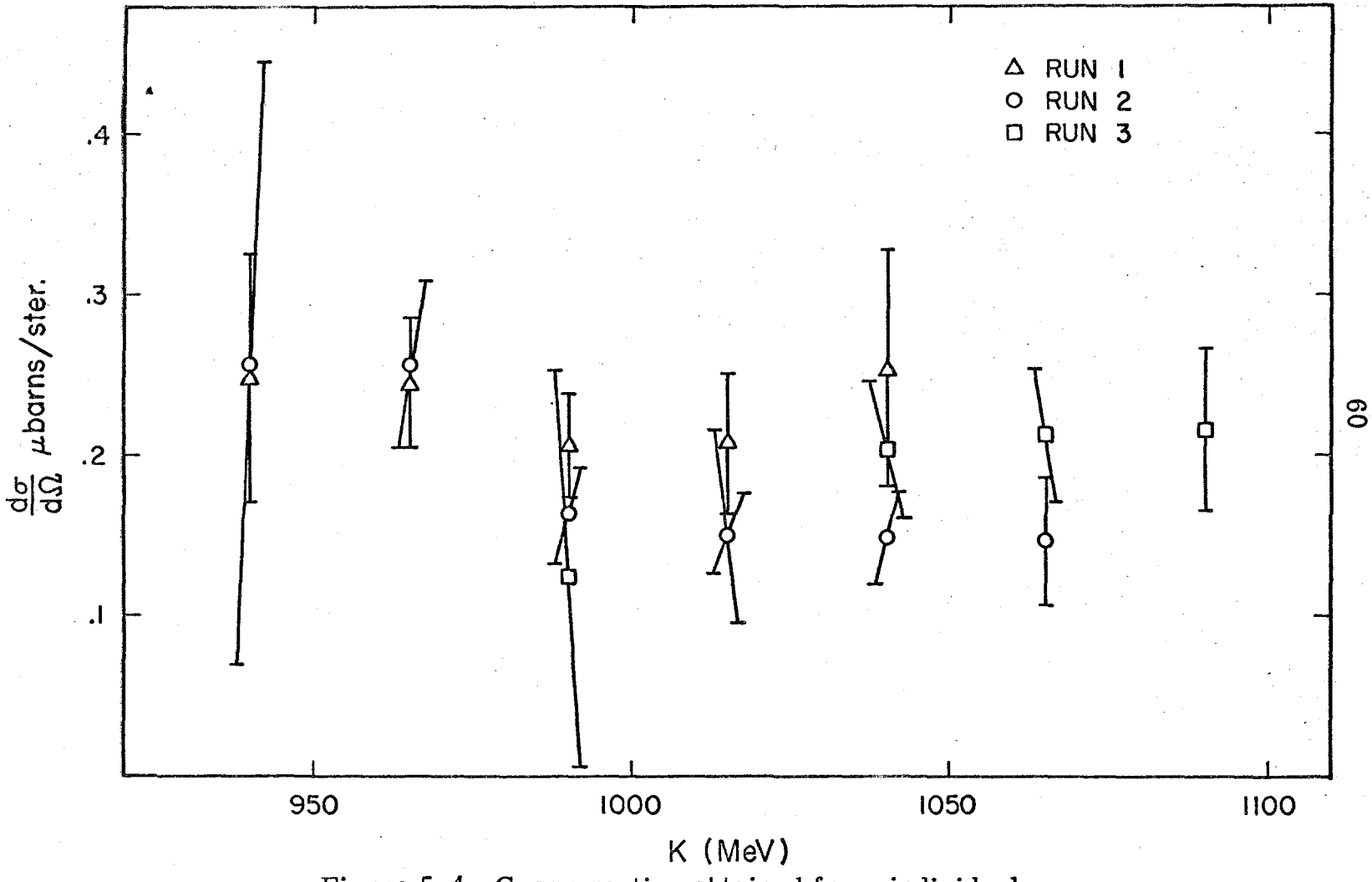

Figure 5.4 Cross section obtained from individual runs

TABLE 5.3

Eta Meson Photoproduction Cross Section

$\theta^*_\eta = 45^o$

Lab Photon Energy Mev	Cross Section barns/ster.
940	$.249 \pm .072$
965	$.248 \pm .032$
990	$.180 \pm .021$
1015	$.164 \pm .020$
1040	$.175 \pm .023$
1065	$.177 \pm .028$
1090	$.216 \pm .050$

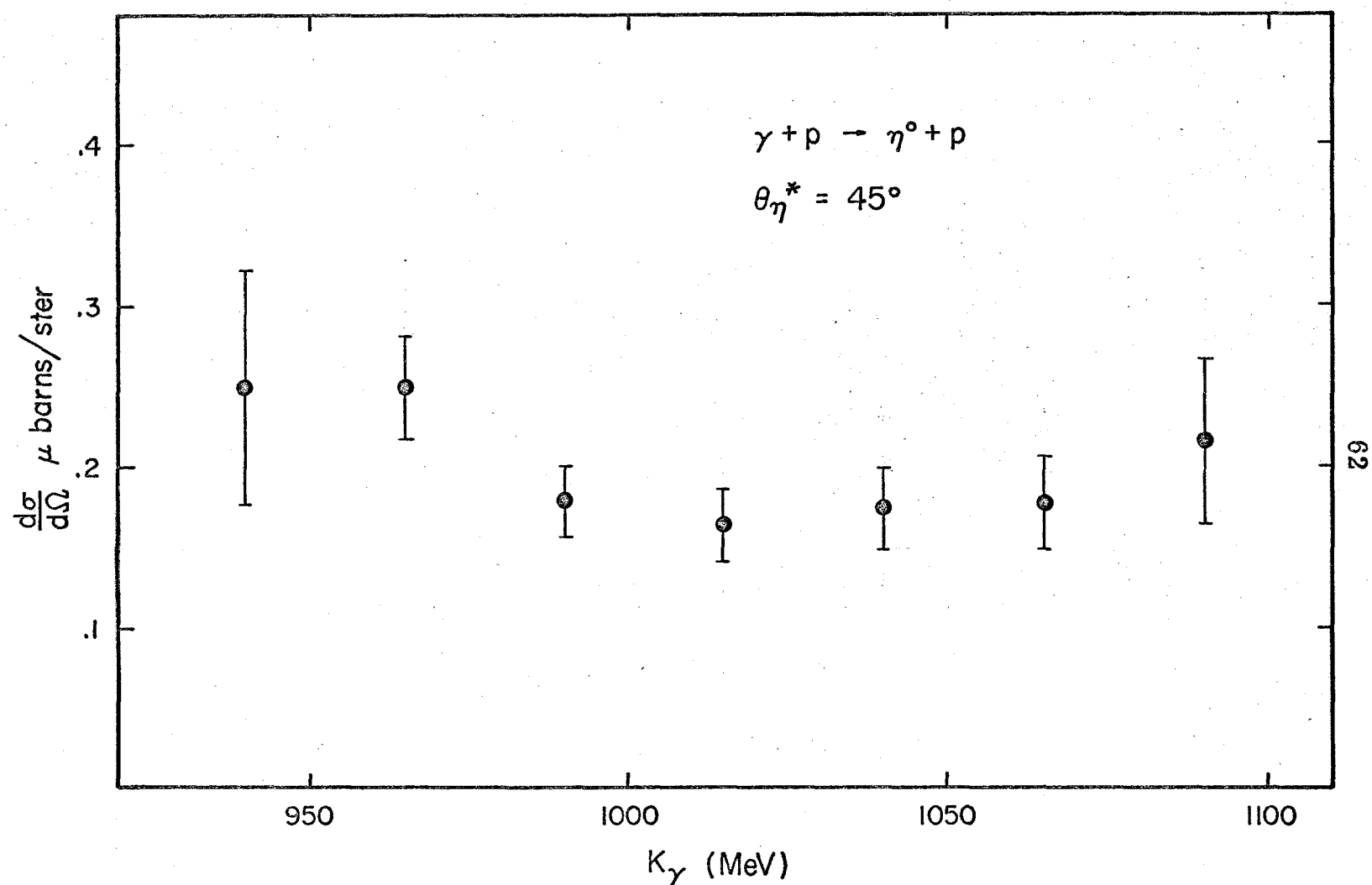

Figure 5.5 Cross section obtained from combined data

For this purpose only those events with large pulse heights* in the shower counters are considered, since this suppresses the background to a greater degree than the foreground. Figure 5.6 shows the mass distribution of all events which survive the higher pulse height requirements. The measured mass of the eta is the mean of the peak sitting on the broad background. These events have a mean

$$M_\eta = 549.9 \pm 1.5 \text{ Mev} .$$

This value does not change for higher or lower base-lines, indicating that the background is symmetrical about $M_\eta = 549.9$ Mev. The statistical uncertainty in the mass is

$$\Delta M_\eta = \sigma/\sqrt{N} = 15/\sqrt{450} = .71 \text{ Mev}$$

where σ is the gaussian width of the distribution, and $N = 450$, the number of events in the distribution. However, the systematic errors are felt to be larger and of the order of 1.5 Mev, so the error quoted is largely determined by the estimated systematic errors.

The measurement of the natural width of the eta is also of interest. Theoretically, this number is expected to be relatively small because the eta is not seen to have any strong decay modes. Consequently, the width should be characteristic of the electromagnetic decays and has been predicted to be in the region of 1 kev.

---

* More precisely, only those events for which both shower counters have pulse heights greater than twice the standard minimum - ionizing pulse height were kept.

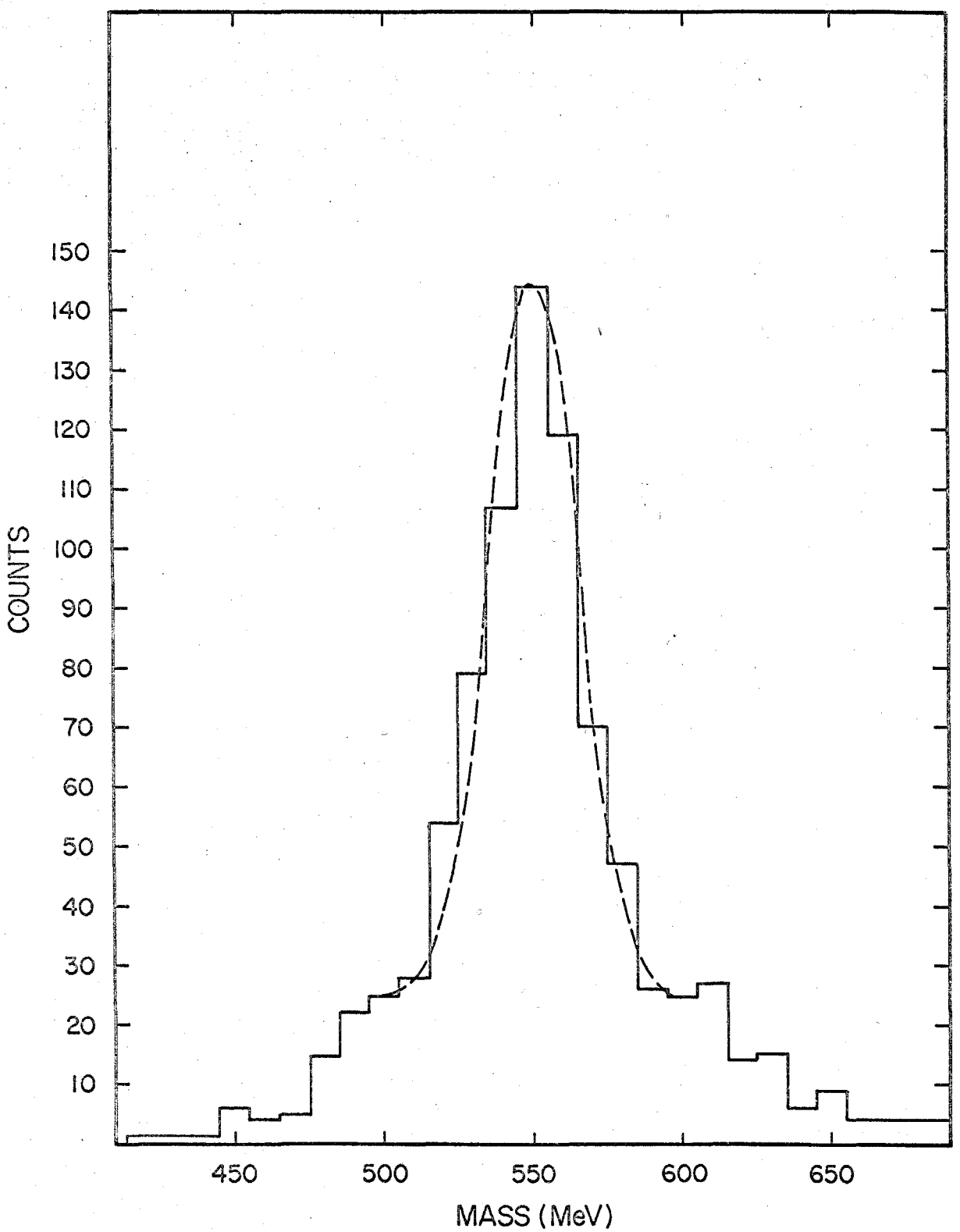

Figure 5.6 Distribution of mass of the two photons for all events satisfying the higher bias criterion. Dashed curve shows expected mass distribution from Monte Carlo calculation

High energy experiments do not approach this sort of resolution and therefore direct observation of the width is not expected. However, an experimental upper limit can be obtained.

If one lets the intrinsic width for the eta be Γ_η, then the observed width, squared, is the sum of squares of the intrinsic width and the experimental resolution $\sigma_{exp.}$:

$$\sigma^2_{obs.} = \Gamma^2_\eta + \sigma^2_{exp.} \quad .$$

The value $\sigma_{obs.}$ is obtained from the histogram and the value $\sigma_{exp.}$ is obtained from the resolution calculation. Solving for the upper limit,

$$\Gamma^2_\eta \leq \sigma^2_{obs.} - \sigma^2_{exp.} \quad .$$

The values $\sigma_{obs.} = 36.7 \pm 1.2$

$\sigma_{exp.} = 35.0$

give

$$\Gamma_\eta \lesssim 15 \text{ Mev} \quad .$$

This value adds no new information. Bubble chamber data give $\Gamma_\eta \leq 10$ Mev for the limit. However, improvements in the apparatus and improvements in the method, which could lower the limit on the width, would be easy, and further experiments will probably achieve this.

VI. DISCUSSION

At this point cautious conclusions will be drawn. A truly complete discussion is not possible due to lack of data. Cross section data over a wider range of energy, and more importantly, over angles would be very valuable. We proceed here with full awareness of these weaknesses and emphasize that our conclusions are tentative.

The data consists of a scan in energy from 950 - 1100 Mev lab photon energy at $\theta^*_\eta = 45^o$ in the center-of-mass. It is known that π^o photoproduction shows a significant bump in this region due to the N***$^+$ (1688, $J^p = 5/2^+$) intermediate state. This is due to the process given by the diagram below. Similarly, eta photoproduction presumably has such a mechanism.

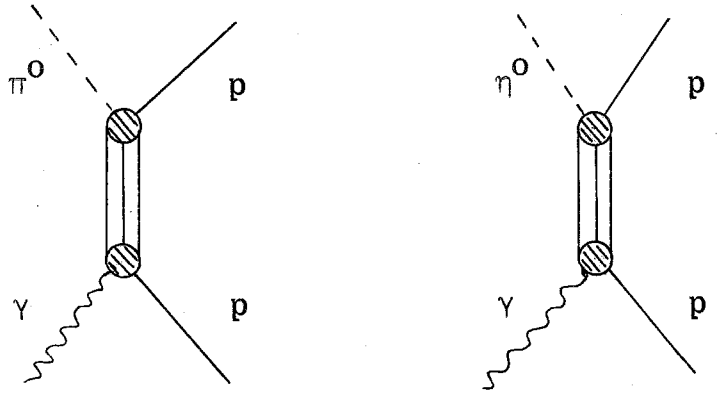

The formation of the intermediate state can be expressed in terms of two amplitudes, i. e., its electric and magnetic multipole transitions. This is characteristic of the ingoing vertex and is the same whether $\pi^o p$ or $\eta^o p$ are in the final state. The outgoing vertex is different and is characterized by different kinematical factors and different coupling constants. As explained in the

introduction, the ratio of $N^{***} \to \pi^o p$ to $N^{***} \to \eta^o p$ can be calculated on the basis of SU(3) and kinematical factors. One gets

$$\frac{\frac{d\sigma}{d\Omega}(\gamma p \to N^{***} \to p\eta)}{\frac{d\sigma}{d\Omega}(\gamma p \to N^{***} \to p\pi)} = \frac{G^2_{NN^{***}\eta} f(q_\eta)}{G^2_{NN^{***}\pi} f(q_\pi)}$$

where f(q) can be approximated by

$$f(q) = q(q^2/q^2 + X^2)^3 \text{ and}$$

X = 350 Mev, which corresponds to a typical "interaction volume" of a particle whose mass falls close to the unbroken SU(3) mass of the pseudoscalar octet*. Numerical evaluation yields $f(q_\eta)/f(q_\pi) \cong 1/3$. Thus

$$\frac{\frac{d\sigma}{d\Omega}(\gamma p \to N^{***} \to p\eta)}{\frac{d\sigma}{d\Omega}(\gamma p \to N^{***} \to p\pi)} = \frac{1}{3} \frac{G^2_{NN^{***}\eta}}{G^2_{NN^{***}\pi}} .$$

Unbroken SU(3) predicts this ratio of coupling constants to be

a) 3 for N^{***} belonging to a $\underline{27}$

b) $1/3\ (3 - 4\alpha)^2$ for the N^{***} belonging to an $\underline{8}$

where α is the F/D coupling ratio defined by $\alpha D + (1 - \alpha)F$ as the $\underline{8} \times \underline{8} \to \underline{8}$ coupling. π^o photoproduction has shown the total cross

---

* This choice of X is by no means compelling and could easily differ by a factor of 2 or 3.

section in this region to yield

$$\sigma_T(\gamma p \to N^{***} \to p\pi^o) \cong 15 \ \mu\text{barns} \ .$$

A quick glance at Figure 5.5 shows that the first case can be excluded. The N*** can be assigned to a new $J^p = 5/2^+$ baryon octet, in agreement with earlier assignments.[18]

The α value has not been measured for couplings to the $5/2^+$ baryon octet. As Figure 5.5 shows, no clear bump in the cross section occurs at the N*** peak. One is tempted to say that no resonance occurs at all. However, interference effects conceivably could change the shape of the differential cross section, while the N*** still would be seen in the total cross section. For an estimate of an upper limit, we will assume that the total cross section for $N^{***} \to \eta^o p$ is given by simply,

$$\sigma_T(N^{***} \to \eta p) \leq 4\pi \frac{d\sigma}{d\Omega}(45^o) \approx 2.5 \ \mu\text{barns}$$

so that

$$\frac{\sigma_T(N^{***} \to \eta p)}{\sigma_T(N^{***} \to \pi p)} \cong \frac{1}{9}(3 - 4\alpha)^2 \leq .166 \ .$$

For limits on α, one obtains

$$.45 \leq \alpha(\text{PS B B}^*) \leq 1.05 \ .$$

VII. APPENDIX

A. Experimental Apparatus

a) The Photon Detectors

For the detection of the eta meson, the decay mode into two photons (branching ratio = 38.6%) was used. The lab energies of the decay photons were 400 to 500 Mev for the kinematical regions covered. These photons are capable of inducing sizeable cascade showers in high-Z materials. The operation of the detectors is based on the phenomenon of photon-induced cascade showers in lead. Each shower counter consisted of alternating layers of lucite and lead. Figure 7.1 shows the lucite radiator of the shower counter. It is constructed out of six sheets of 1/2" lucite, 6" wide by about 14" long. At one end five 1/4" lucite spacers, 4" wide, are glued between the sheets of lucite, separating them by 1/4" gaps. A lucite cement was used in each of these joints so that good, bubble-free contact was achieved. The end with the 1/4" spacers forms a short light pipe for the counter. The piece of lucite is then machined flat around the sides and on the ends. The light pipe section is tapered on a lathe to better fit on a 5" photomultiplier tube. All machined surfaces are then polished to improve the internal reflection of the device. The counter is wrapped with .0005" aluminized mylar and black tape to seal the counter from external light sources. A 5" photomultiplier tube is mounted against the light pipe section with the help of a clear silicon grease to give good optical coupling. The completed counter is then mounted in a frame that supports and protects the device. Lead sheets, 1/2 centimeter thick and cut to fit the 6" by 10" aperture of

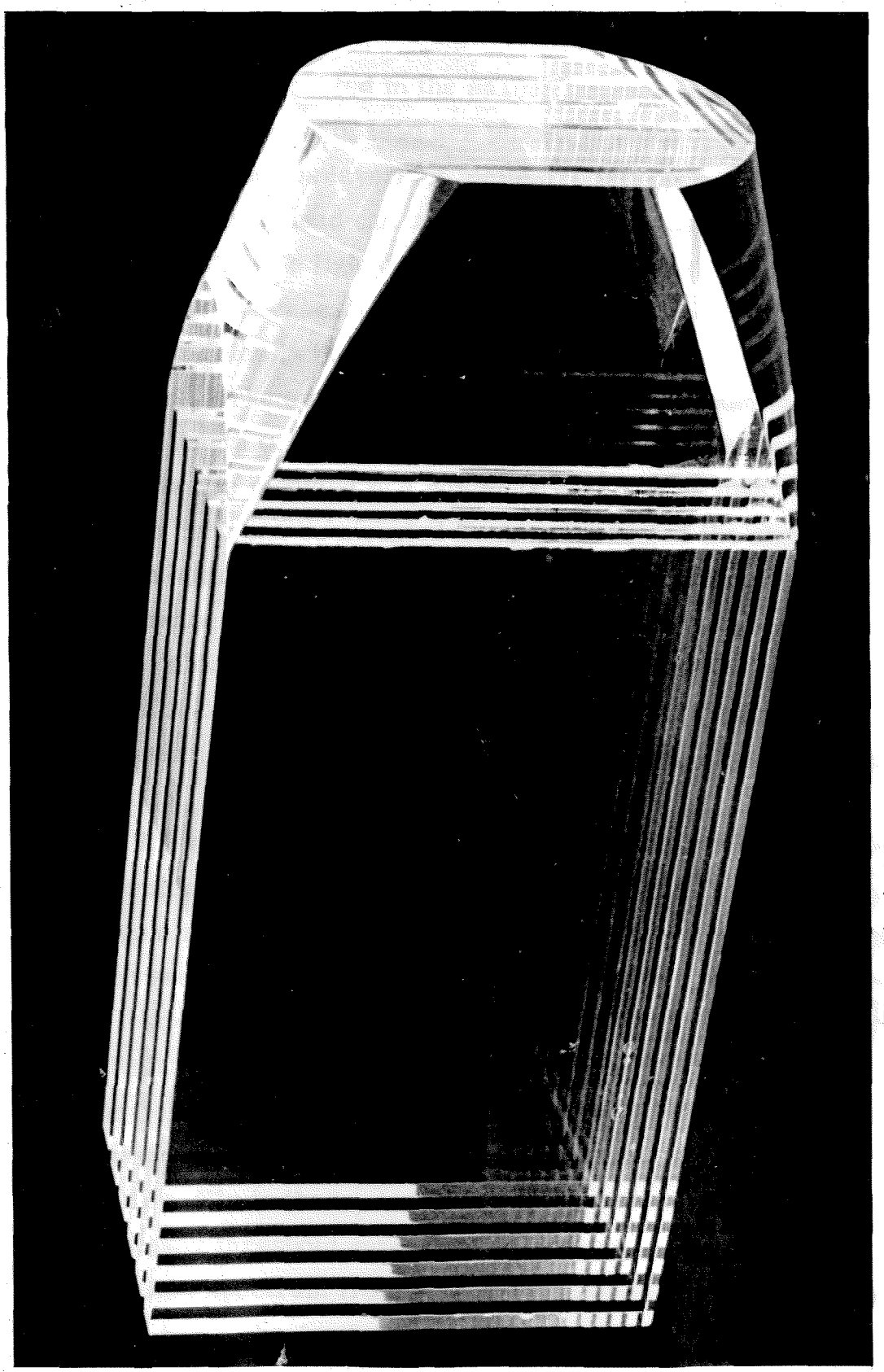

Figure 7.1 The unwrapped lucite radiator

the counter, are inserted in the spaces between the lucite sheets. Two additional sheets of lead are placed in front of the counter. The gaps between the layers of lucite are left open so that the .5 cm thick layers of lead can be easily inserted and removed at will without breaking the light-tightness of the lucite radiator section.

As the cascade shower develops in the layers of lead, the charged particles in the shower generate Cerenkov radiation in the lucite slabs. The amount of light generated is proportional to the total path length of charged particles in the lucite radiator slabs. The radiator is mounted in a holder so that a RCA 7046 5" photomultiplier tube can be mounted flush to the end of the short light pipe. An optical grease is used between the photomultiplier face and the lucite light pipe to insure a good optical joint.

Comparison checks were done with other types of counters in an effort to select the best possible shower counter. In particular, the lucite-lead sandwich scheme was tested against an identical counter consisting of a lead-scintillator sandwich. Figure 7.2 shows the integrated pulse-height distributions for both type counters, tested on π's and e's. The lead-scintillator sandwich has a much sharper front rise, indicating that the light output is much greater than that of the lucite. However, the π-distribution in the lead-scintillator counter has a longer tail, showing that the scintillator is much more capable of producing large pulse heights. This is probably caused by low energy processes such as knock-on protons or nuclear-star type of events. The scintillator will respond readily to these, but the lucite is a Cerenkov radiator, and the Cerenkov threshold cuts these events out. As a result, the pulse-height spectrum from π's passing through the lead-lucite sandwich has a shorter tail than does that of a similar lead-

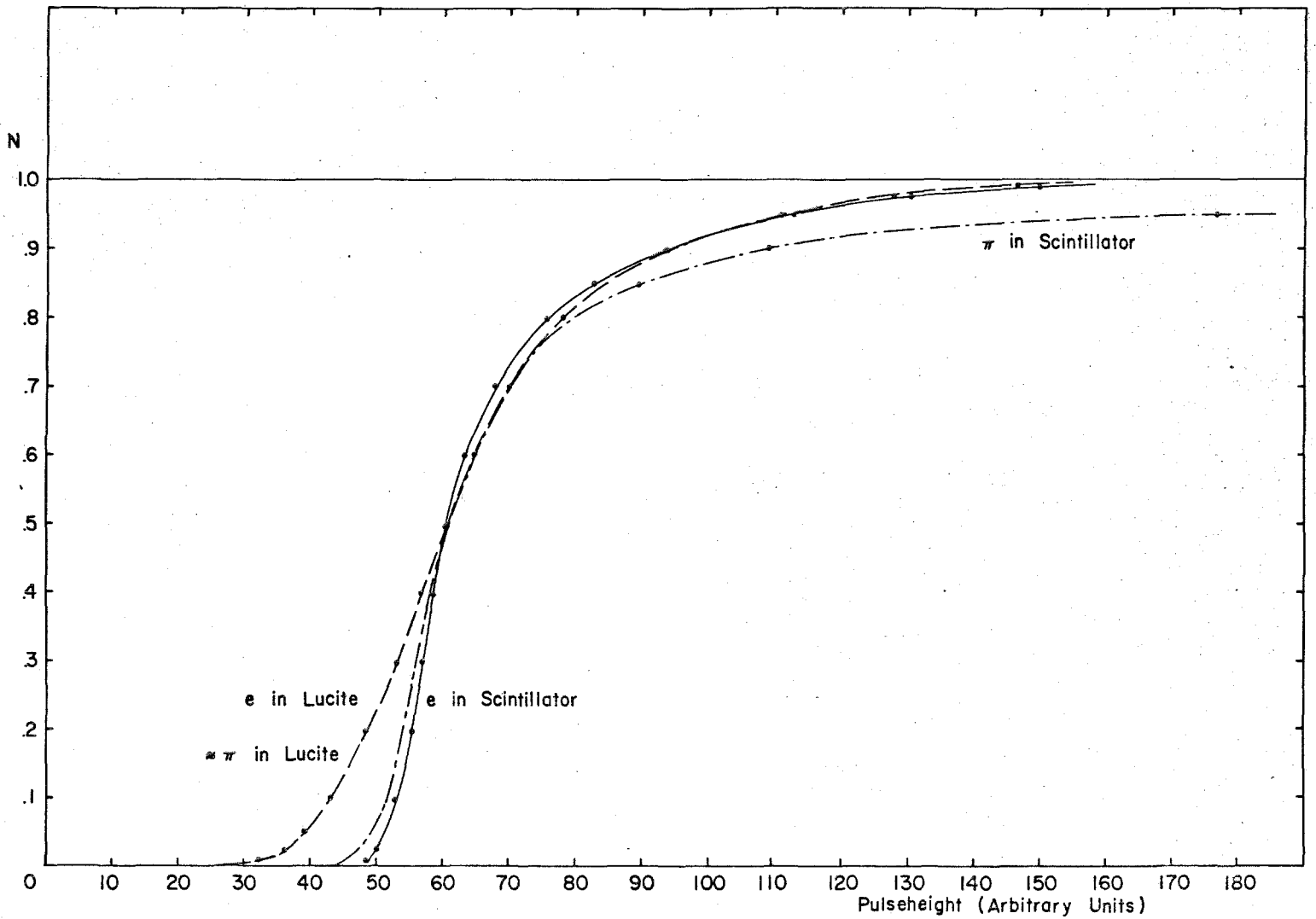

Figure 7.2 Integrated pulse-height distributions; comparison of π and e responses in lucite to those in scintillator

scintillator sandwich. Furthermore, the lead-lucite sandwich has no response at all to incident protons in these energy ranges, because of the Cerenkov cutoff, while the lead-scintillator sandwich will show large responses due to the relatively high dE/dx of slow protons.

Figure 7.3 shows the response of the lead-lucite counter to energetic electrons. The lead-scintillator counter shows very similar distributions. The widths of the distributions are largely due to shower fluctuations in the counter and, only to a lesser degree, to the broadening from light collection within the counter and photoelectron statistics at the photocathode of the photomultiplier. Figure 7.4 shows how pulse heights from π's compare to those of monoenergetic electrons of 500 and 1000 Mev. It is seen that the amount of separation of π's from showers, based on pulse heights, depends on the overlap of the two distributions. Since the π-distribution in the lead-lucite counter has a smaller tail, it was selected for the purpose.

The testing of the shower counters was done with monoenergetic electrons, since monoenergetic photons were not readily available. However, the counter is a total absorption device, and photon showers differ from electron showers significantly only in the first several radiation depths where memory of the incoming charge is still retained to some degree. The counters were thus operated with $2X_0$ (X_0 = radiation lengths) of lead placed in front and $5X_0$ inserted in the counter, $1X_0$ in each of the available gaps. It was assumed that there was no significant difference between photons and electrons. Tests performed after this experiment using the tagged photon beam have confirmed the validity of this assumption.

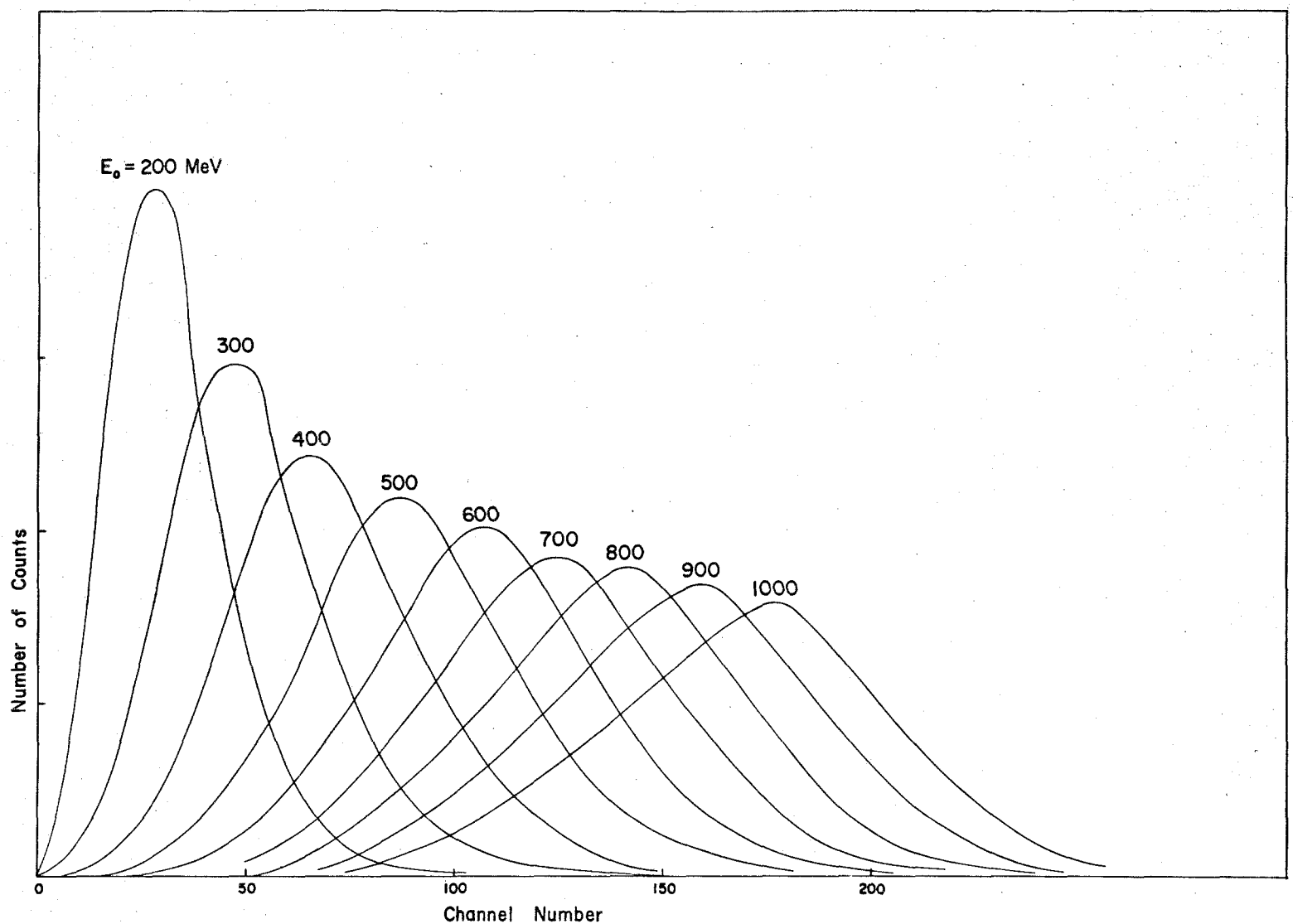

Figure 7.3 Pulse-height distributions from the lead-lucite sandwich counter for mono-energetic electrons

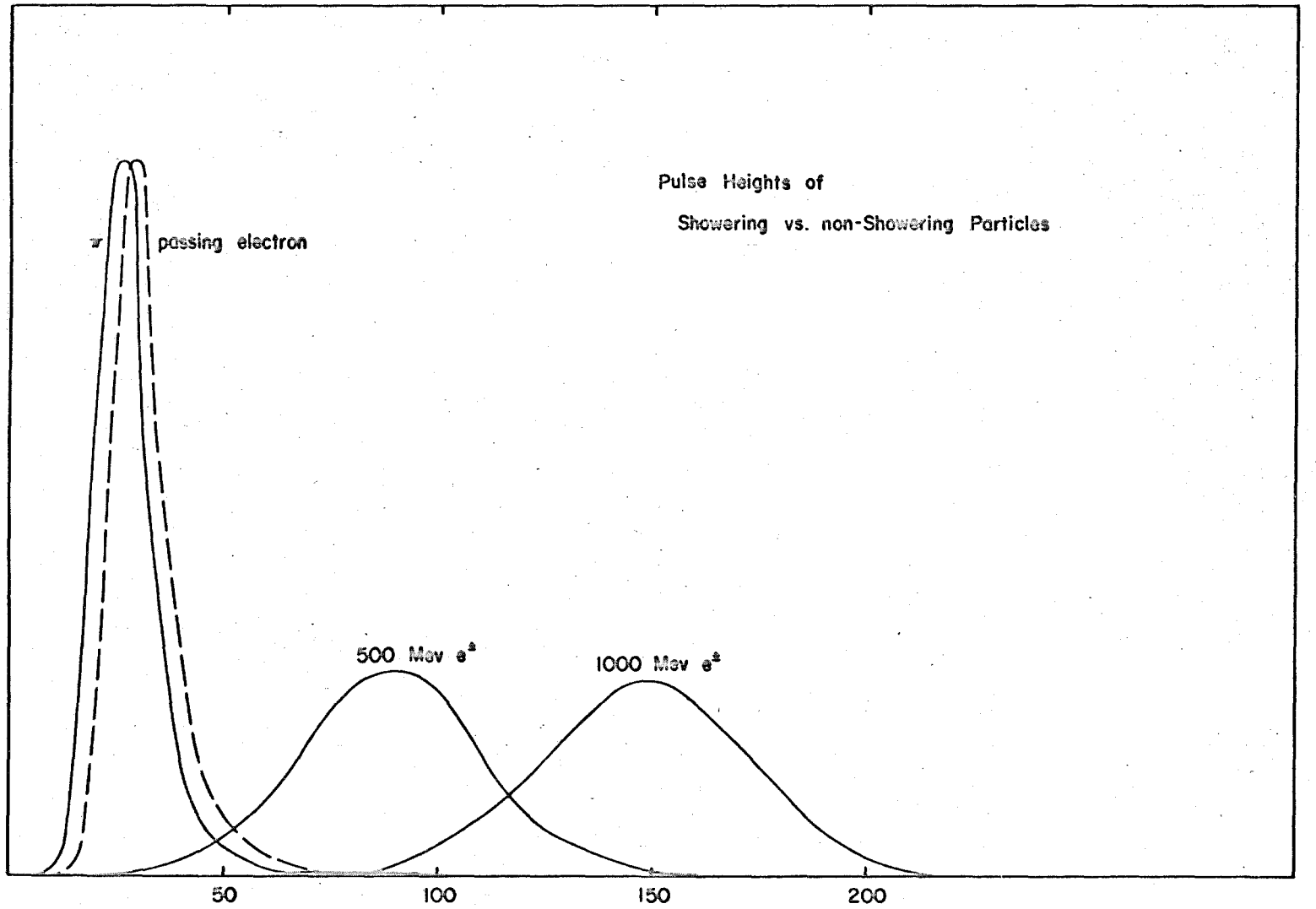

Figure 7.4 Comparison of electron shower distributions with the distribution for fast non-showering particles

To further improve the selection of photons, veto counters were placed in front of the shower counters to veto all charged particles. This eliminated π's and e's since they are charged and, at least in principle, leaves only γ's.

The veto counters consist of two counters, each of 1/4" thick NE102 scintillator cut to the dimensions of the aperture of the shower counters. Two vetoes for each shower counter were necessary because the veto rate for a single counter was found to be too high. To reduce the rates in the counters, .060" aluminum sheet was added in front of the first veto and .060" copper sheet was added between the two veto counters. This procedure held the veto rate to an acceptable 250 kilocycle peak. The two vetoes were run in fast coincidence. Thus, photons converting in the .060" copper sheet would not be vetoed because the coincidence requirement would not be satisfied. Only the .060" aluminum, the air between the counters and the target, the liquid hydrogen in the target, and the target walls were able to convert the photons before they reached the veto counters. Corrections for the loss of events due to photons which prematurely convert are small, and will be found in the section devoted to systematic corrections. The efficiency of these counters was measured to be greater than 99% on fast π's passing through the counters. Thus, with high efficiency charged particles were rejected at the first line of defense.

The pulse height generated in the shower counters was a significant piece of information. The pulse height in each counter was electronically converted to binary-coded-decimal and displayed on the film with incandescent lamps. In addition to the pulse-height information, more information on the photon was needed. The

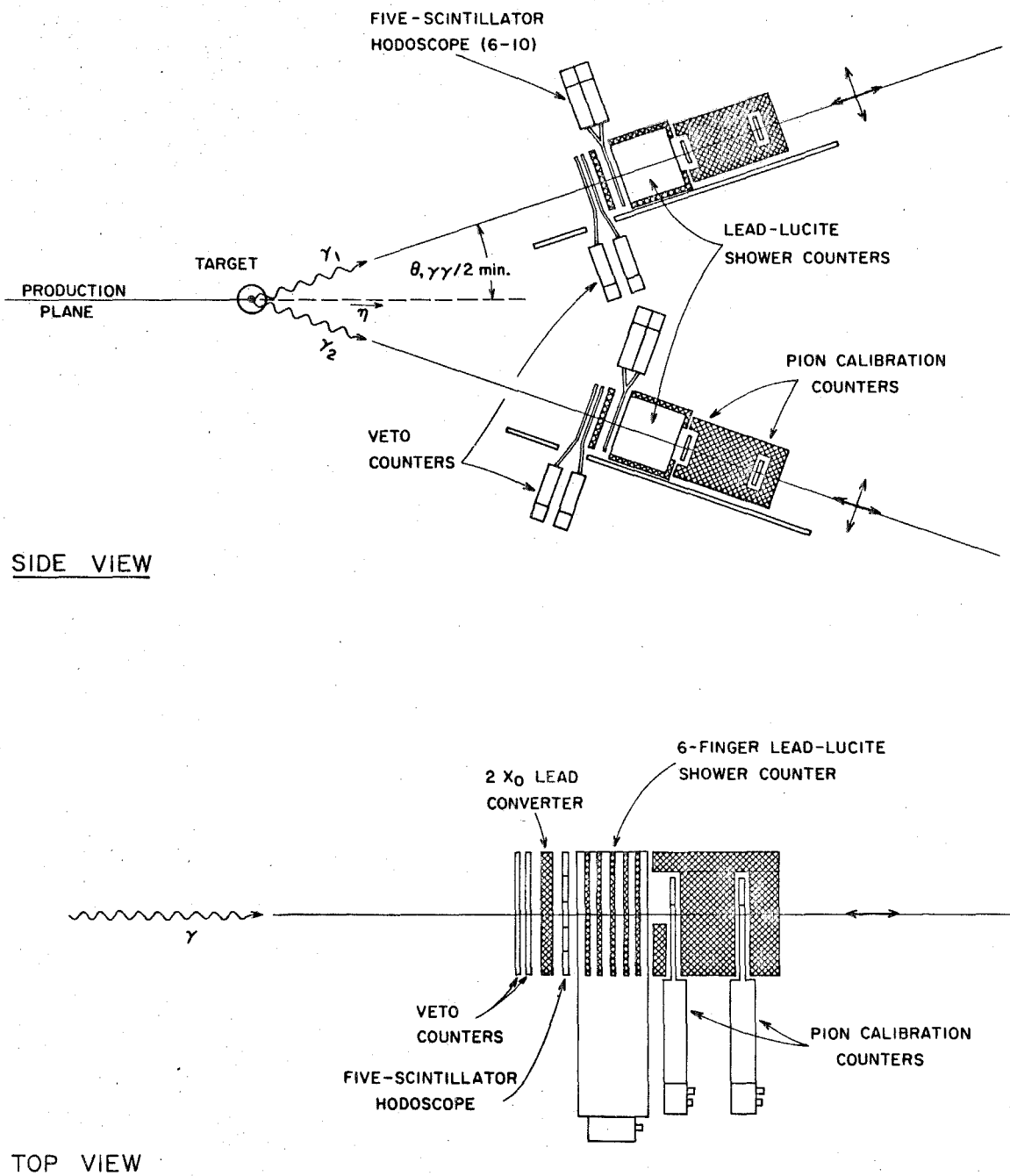

Figure 7.5 Configuration of the photon counters

position of the point at which the photon entered the shower counter was an important kinematical parameter. A scintillation hodoscope was constructed of five scintillator counters, each attached to a separate RCA 7850 photomultiplier. The scintillators were 2" wide and 6" long, and were placed adjacent to each other, covering the aperture of the shower counter. Each scintillator fell approximately along lines of constant θ so that each of the five scintillator counters subtended different θ-bands on the face of the counter. Two radiation lengths of lead were placed in front of the hodoscope so that photons would interact in the material, produce e-pairs, and thus reveal the θ-position by pulses generated in one of the scintillator hodoscope slats.

The complete photon detection apparatus is shown in Figure 7.5. Behind the shower counters sit two more counters used for defining fast π's. Between these two counters are placed 6" of lead to stop all particles except fast π's and μ's. These give a standard minimum-ionizing distribution used to calibrate the pulse heights of the shower counter, and they were also used to test the efficiencies of the vetoes and the scintillator hodoscope. The details of the calibration procedure are given in the Appendix, Section VII-C. A more detailed discussion of the shower counters will be found in CTSL-41[25] and in the literature[26].

b) The Proton Telescope

The proton telescope consists of three scintillation counters and three spark chambers. Figure 7.6 shows the physical layout of the proton telescope. The three scintillator counters were constructed of 1/4" NE102 scintillator, with dimensions chosen

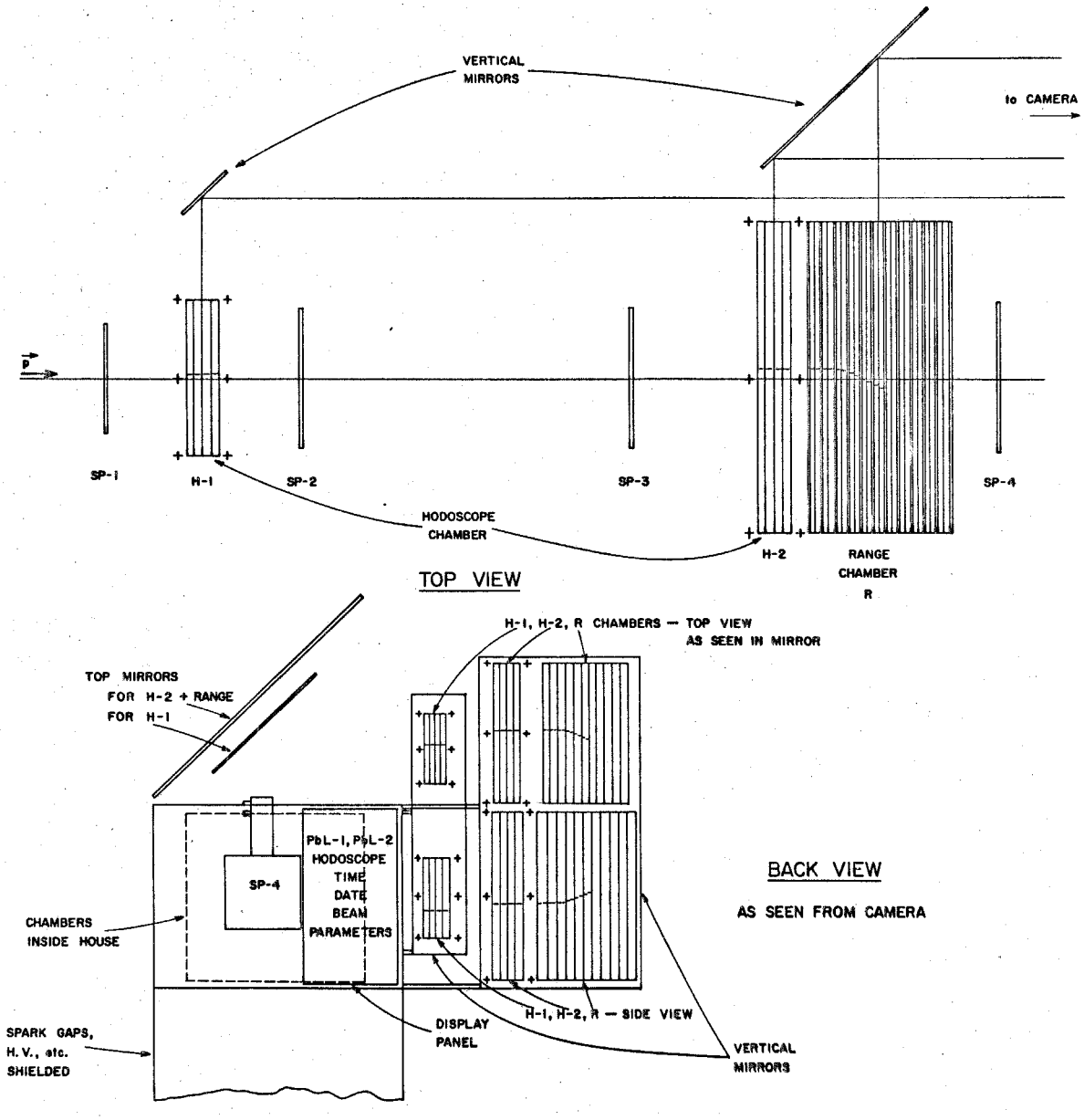

Figure 7.6 Schematic view of the spark chambers

such that the solid angle subtended by the system was defined by the third counter, the one farthest from the target. Each counter had a flat light pipe which was tapered down to fit onto a RCA 7850 photomultiplier. Between the first and second counters was placed a 4-gap thin foil spark chamber. The spark chamber was constructed of .001" aluminum foil stretched and glued between lucite frames that had been accurately machined to .290". Two outside gaps were added, one to the front side and one to the back side, and were covered with .005" mylar. This served to equalize the pressure on the two outside foils of the spark chamber and thus prevent bowing of the thin foils due to the slight pressure differential between the inside and outside of the spark chambers. Gas flowed in parallel through the gaps of the chamber to prevent a pressure differential within the chamber. Electrical contact to the chambers was achieved by contacts mounted in the side of the chamber. The high voltage was applied to the second and fourth foils, by use of spark gaps, while the ground leads were connected to the first, third, and fifth foils. The aperture of the front thin foil chamber was 8" by 10". A second thin foil chamber was constructed in an identical manner to the front chamber, but had an aperture of 17 1/2" square. The third spark chamber was placed behind the large thin foil chamber and consisted of eleven two-gap modules mounted between twelve aluminum plates. The aluminum plates served the purpose of slowing and stopping the protons, thus yielding the energy of the proton through its range. Each two-gap module could be slipped in and out by loosening the frame which held the range chamber together as a unit. The scheme of using two-gap modules between the aluminum absorbers improved the spark efficiency to close to 100% and thus eliminated errors in the proton range

measurements that would otherwise have occurred when the final gap in the proton track failed to fire. The two-gap modules consisted of a foil of aluminum stretched between two frames of lucite. The aluminum foil served as the high voltage electrode and the aluminum plates on either side served as ground contacts. The modules were rendered gas tight by use of a vinyl gasket placed around the edges of the lucite. When the modules and aluminum plates were assembled and the frame compressed by means of bolts which ran the length of the chambers on the outside, the gaskets were pressed firmly against lucite and aluminum and sealed the unit from gas leaks. Figure 7.7 gives the details of the modular construction of the range chamber.

To permit accurate measurement of spark positions in lab coordinates, fiducial marks were added to all views of the spark chambers. These consisted of lucite strips upon which crosses were positioned to high precision. Xenon flash tubes were attached to the ends of the lucite strips and flashed once per event. The film then showed the sparks inside the chamber and the fiducials at the edge of the views. Prior to running the experiment, the fiducial marks were surveyed accurately so as to locate precisely the lab coordinates of each. Then spark coordinates were found by measuring the displacement of sparks from the fiducials on the film. Computer analysis corrected each measurement for parallax effects and for apparent shift of spark positions because of the lucite walls of the spark chamber. The proton angle was obtained by measuring the position of the sparks in the first and second thin foil chambers. The range of the proton was determined by counting gaps that fired in the third chamber. The amount of aluminum contained in the chamber was precisely known, so the energy of

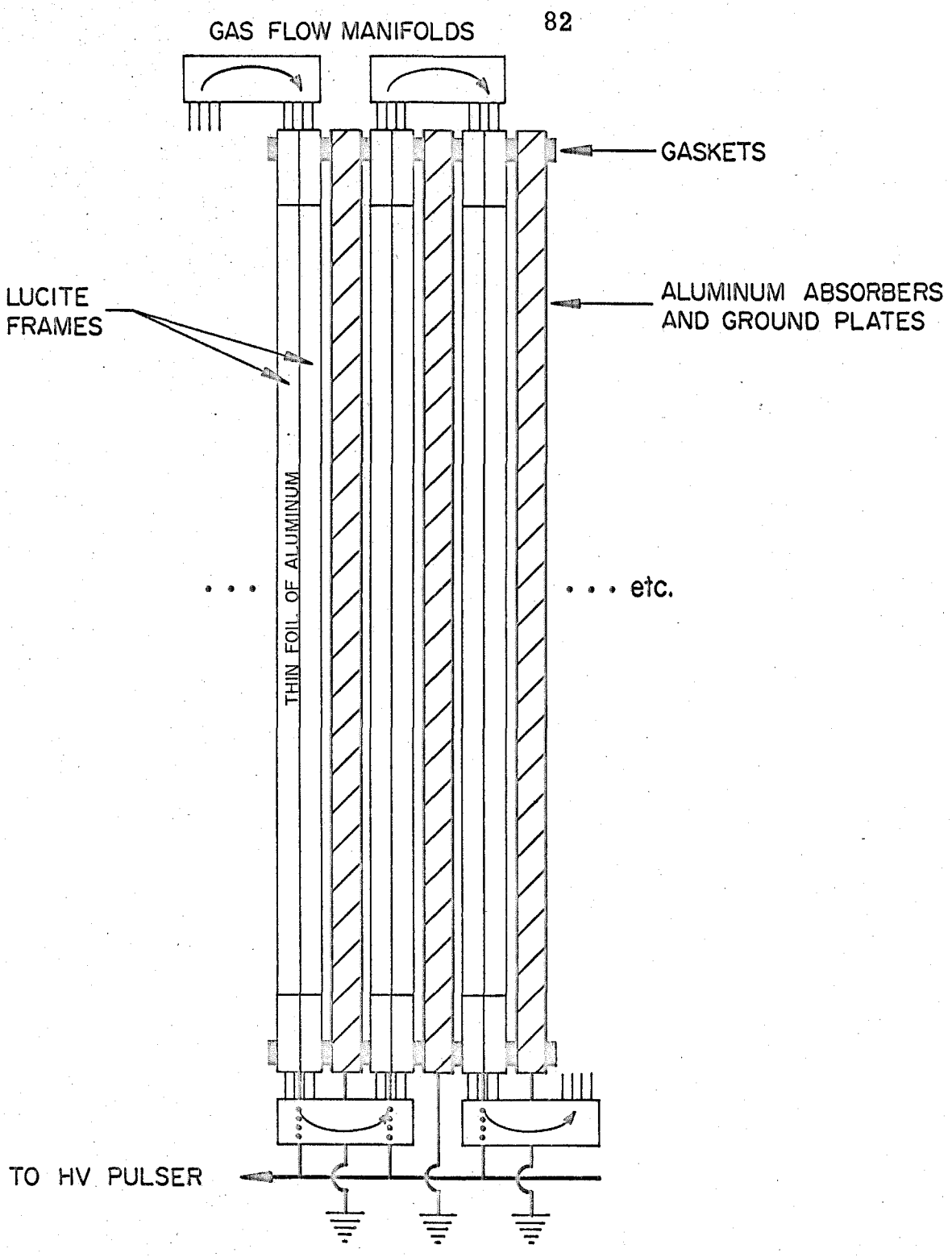

Figure 7.7 Modular construction of the range chamber

the proton could be determined by its range in the aluminum. Figure 2.1 shows the general layout for the spark chamber house and tent. The camera sits behind the chambers and somewhat to one side. Mirrors were placed at the side of the house and sit at $\sim 45^{o}$ to bring the spark chamber image back to the camera. On top of the house a second set of mirrors was placed for the stereo view. They were tilted to bring the image out the top, and into the side mirrors, thus reflecting back to the camera. In effect, the camera looks into the side of the chambers for one view, and into the top for the other view. Alignment of the mirrors, requiring considerable ingenuity and care, was done with the aid of a surveying transit. Details of this alignment, although of great importance to the experiment, will be omitted.

It was desirable to display all the experimental information available for an event on a display panel in the picture, along with the spark chamber pictures. To do this a panel of lights was constructed, which was flashed once per event. The information displayed was:

1) An event number scaler which advanced one per event. It was used to give each frame an identity distinct from all others.

2) Clock

3) A scratch pad to identify run number, date, and extraneous information

4) Two binary readouts for the pulse heights measured in the shower counters

5) Two sets of 5 lights each, which were lit if and only if the corresponding scintillator in the hodoscope counter registered a count at the time of the event. These provide a measure of the "θ_η" for the event.

Finally, for the purpose of calibration of the proton telescope, a fourth scintillator counter was placed behind the range chamber. When this counter was placed in the electronic logic, passing protons could be selected for testing the spark chambers or for setting the biases on the proton counters. Details of the calibration are given in the Appendix, Section VII-C.

c) Electronics

Figures 7.8 and 7.9 show the general structure of the logic and readout systems. The fast logic consisted of a threefold coincidence between the two photon counters and the proton telescope. Photons were defined by the shower counters vetoed by the two veto counters. Protons were defined by the fast threefold coincidence of the three proton counters. All counters which took part in the fast logic system were first put into limiter circuits. The outputs of the limiters were clipped and put into fast discriminators. The discriminators were run with 10 ns. width cables so that all delay curves had approximately a 20 ns. width. The 20 ns. of dead time was short enough to keep corrections down to a minimum.

Timing of counters was done with an independent counter which could be physically moved around in the beam area. Corrections for the time of flight were done by adding additional cable where needed.

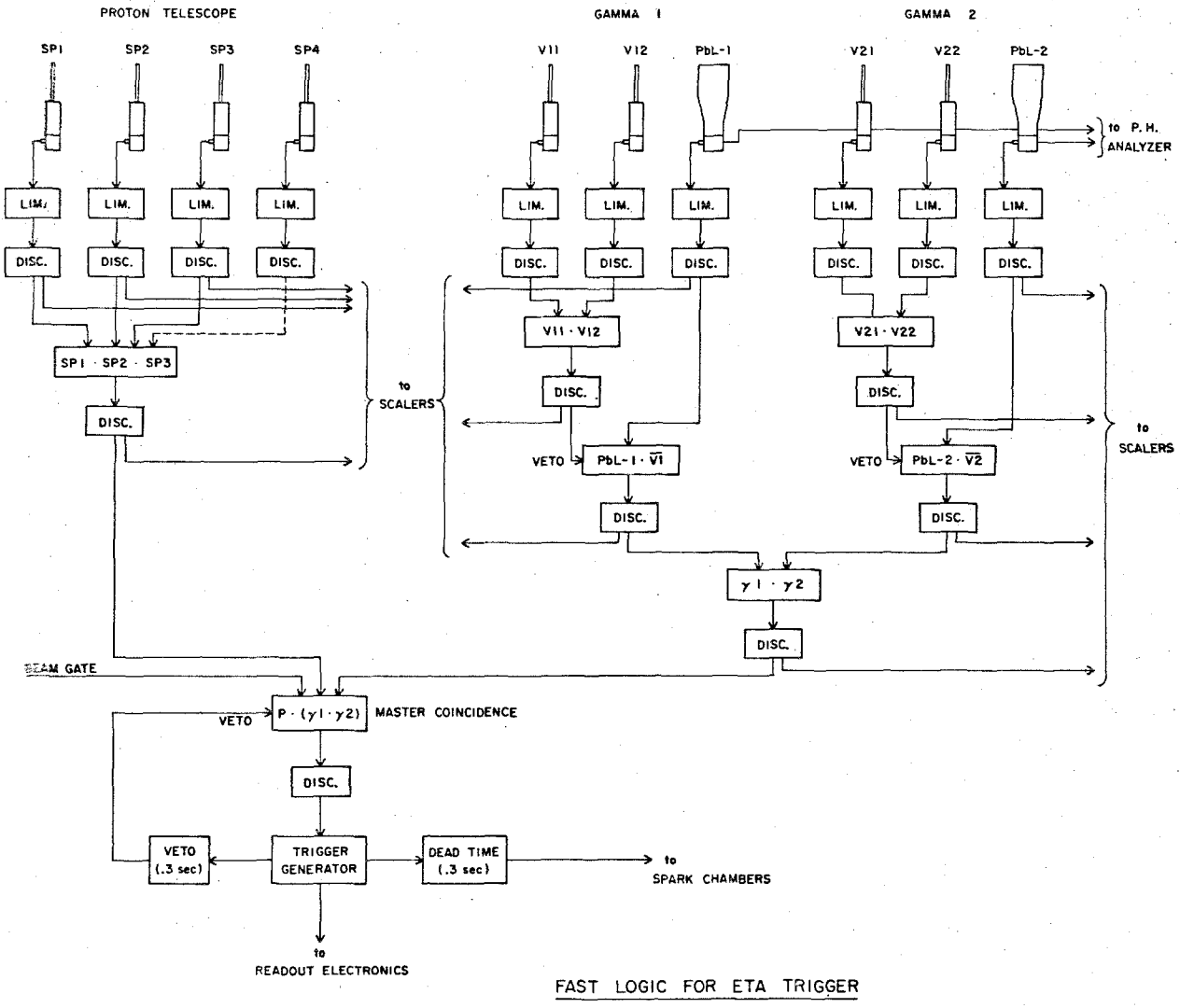

Figure 7.8 Block diagram of the electronics; fast logic

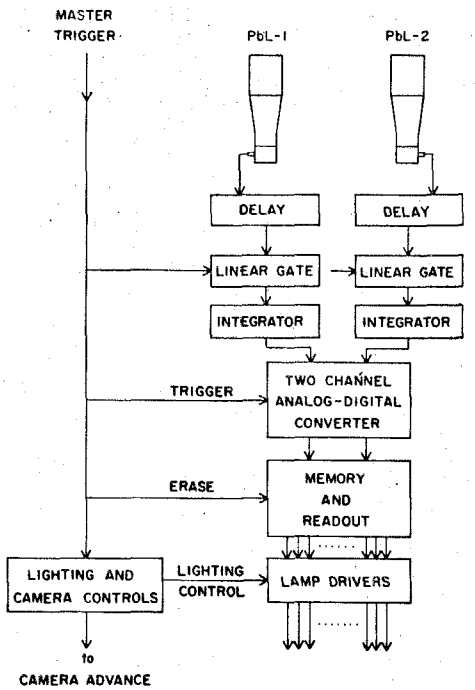

PULSE HEIGHT ELECTRONICS

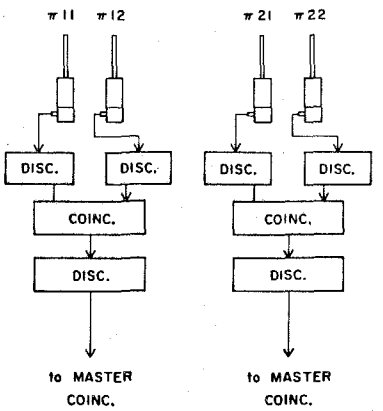

PION CALIBRATION FOR SHOWER COUNTERS

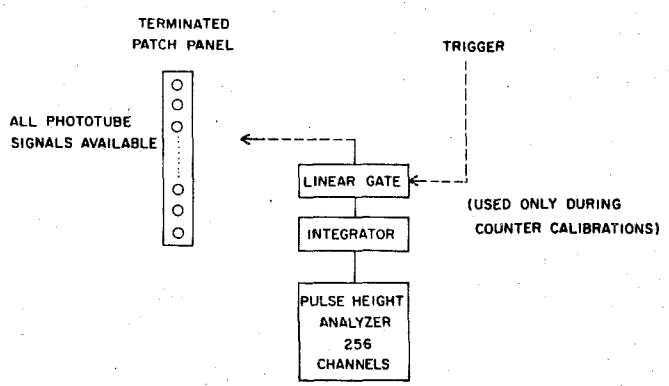

SYSTEM FOR COUNTER CALIBRATION

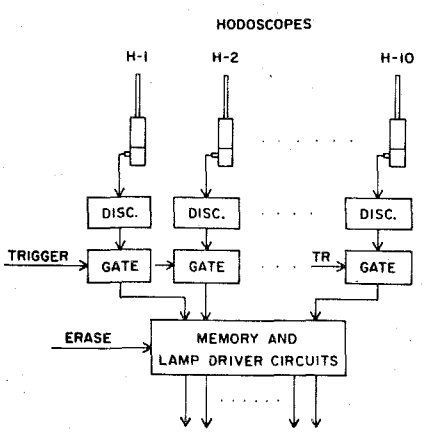

HODOSCOPE ELECTRONICS

Figure 7.9 Block diagram of the electronics; readout and calibration electronics

The fast threefold coincidence then generated a master trigger which was sent to the trigger circuit on the spark chambers, and also initiated a frame advance sequence. This sequence consisted of first erasing the memories of the hodoscope display unit and pulse-height display unit, then reading in the new hodoscope and pulse-height information. The lights for the display panel are then flashed for approximately 100 msec. During this time the film is stationary and is exposed. When the lights on the display panel returned to off, a pulse was sent to advance the film and the event scaler. The apparatus is then ready for the next event. This sequence of events required approximately 300 msec. and was therefore limited to occurring once per beam pulse. To insure that a second master pulse did not occur during this time, a veto circuit prevented the master trigger circuit from operating. Corrections for the resulting dead time were small.

d) Target

A thin-walled liquid hydrogen target was located in the lab at the point defined as the origin of coordinates. It consisted of a cylindrical mylar cup 16.1 cm long and 5 cm in diameter. Around the cup was placed a .001" aluminum heat shield, kept at liquid N_2 temperature through thermal contact with a nitrogen container, to help reduce the boiling rate of the liquid hydrogen. The outside shell of the target was .035" thick, with a window cut for the proton exit. This window was covered with .005" mylar, as were the ends of the cylindrical shell, where the photon beam entered and left the target. The space between the outside shell and the hydrogen cup was maintained at vacuum with a diffusion pump. Figure 7.10 shows the construction of the target.

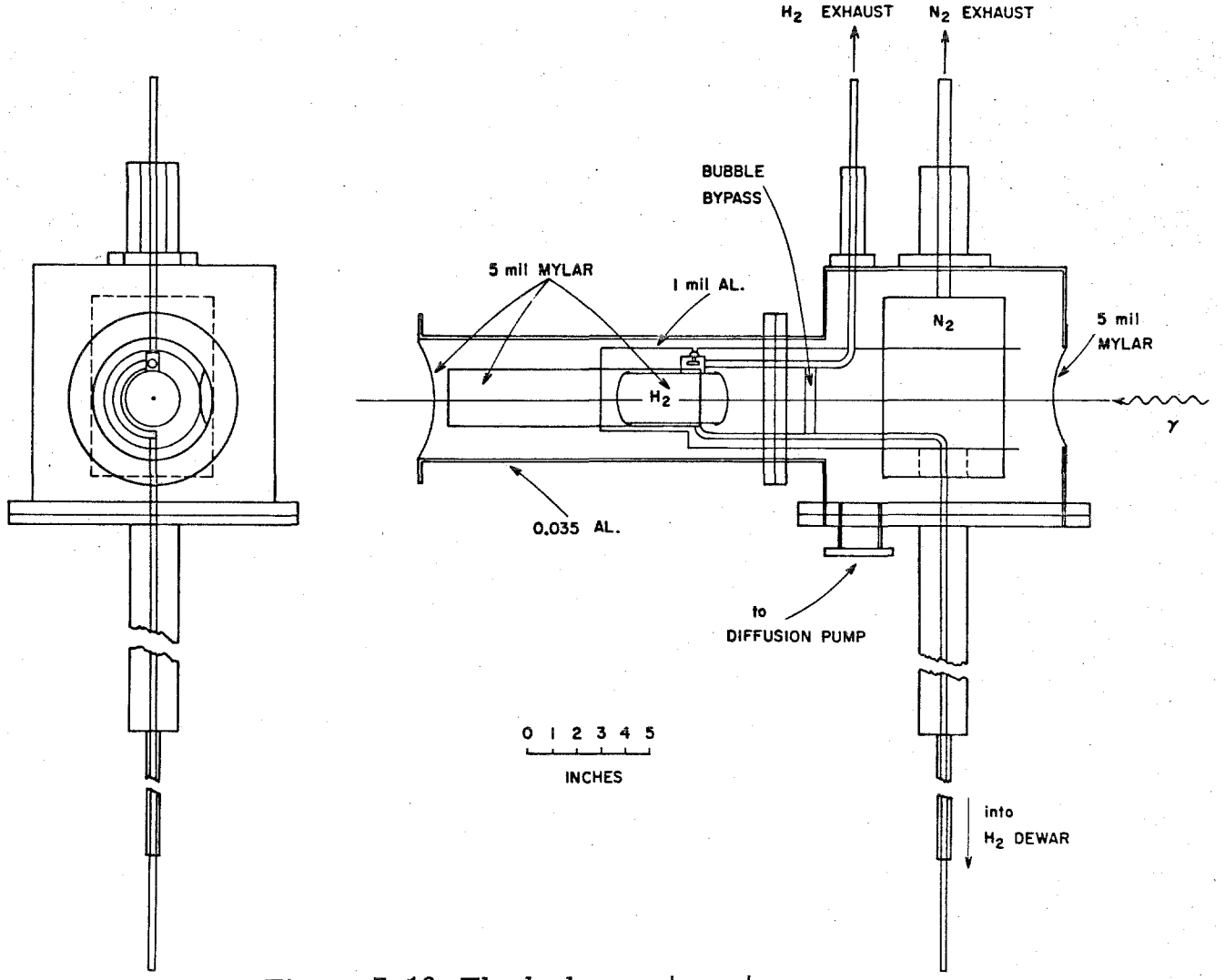

Figure 7.10 The hydrogen target

B. Consistency Checks

a) Measurement of the Pion Photoproduction Cross Section

For an independent check on the experiment as a whole, it was decided that a measurement of some π^o photoproduction cross sections would be performed. It was felt that the kinematics should be chosen so as to duplicate as closely as possible the conditions of the eta experiment. The proton range chamber dictated a definite range in the value of T_p. Furthermore, it was desirable to have a reasonably high energy photon in each shower counter. The following kinematical parameters were the ones chosen:

$k_o = 800$ Mev

$\theta^*_\pi = 50^o$

$\theta_\pi = 31.2^o$

$\theta_p = 60.9^o$

$T_p = 90$ Mev

$\theta_{\gamma\gamma/2} = 11.5^o$

$E_\gamma = 350$ Mev

As far as the apparatus is concerned, the only real difference between the π^o runs and the η^o runs is that the decay photons have less energy. This results in lower pulse heights in the shower counters, but little else is changed.

In this run the cross section is considerably larger than that for the η^o runs. Also the detection efficiency is 10 times larger because of the solid angle transformation on the pion side.

Finally, the pion decays almost entirely into two photons, while the eta goes into that mode only about one third of the time. These effects enhance the π^o yield to give an almost pure selection of events. Background contaminations are held to a negligible level. The rather pure selection of events provided a good set of data against which the Monte Carlo calculations described in Sections III-F through III-H could be compared.

Figure 7.11 shows the distribution of $\Delta\theta$ (= calculated θ_{π} - observed θ_{π}) for all π^o events. The histogram is not centered at 0^o (as it should be) but instead seems to center about $-.4^o$. The source of this error is presumably due to systematic errors in the range measurement of the kinetic energy of the proton. This predicted meson angle is quite sensitive to errors in T_p, especially in the case of π's because of the kinematics of pion photoproduction. This problem is not nearly so critical in eta photoproduction. The solid curve in Figure 7.11 shows the calculated $\Delta\theta$ curve from the Monte Carlo program. This curve has been artificially shifted $.4^o$ to the left so as to agree as well as possible with the data. The agreement is otherwise very good. The gaussian width of the data is 2.19^o while that of the Monte Carlo calculation is 2.16^o.

The angles were surveyed with a transit which is capable of measuring angles to an accuracy of 1 minute of arc. Misalignment of the fiducials is not thought to be the source of the $.4^o$ discrepancy.

For the purpose of data analysis in the eta experiment, the $\Delta\theta$ distribution was not used because it was felt that the (equivalent) mass distribution was more appropriate. A similar M_{π}-distribution could not be used in this case for a somewhat surprising reason. Multiple scattering of the proton sometimes took the proton angle outside kinematical limits. Calculation of

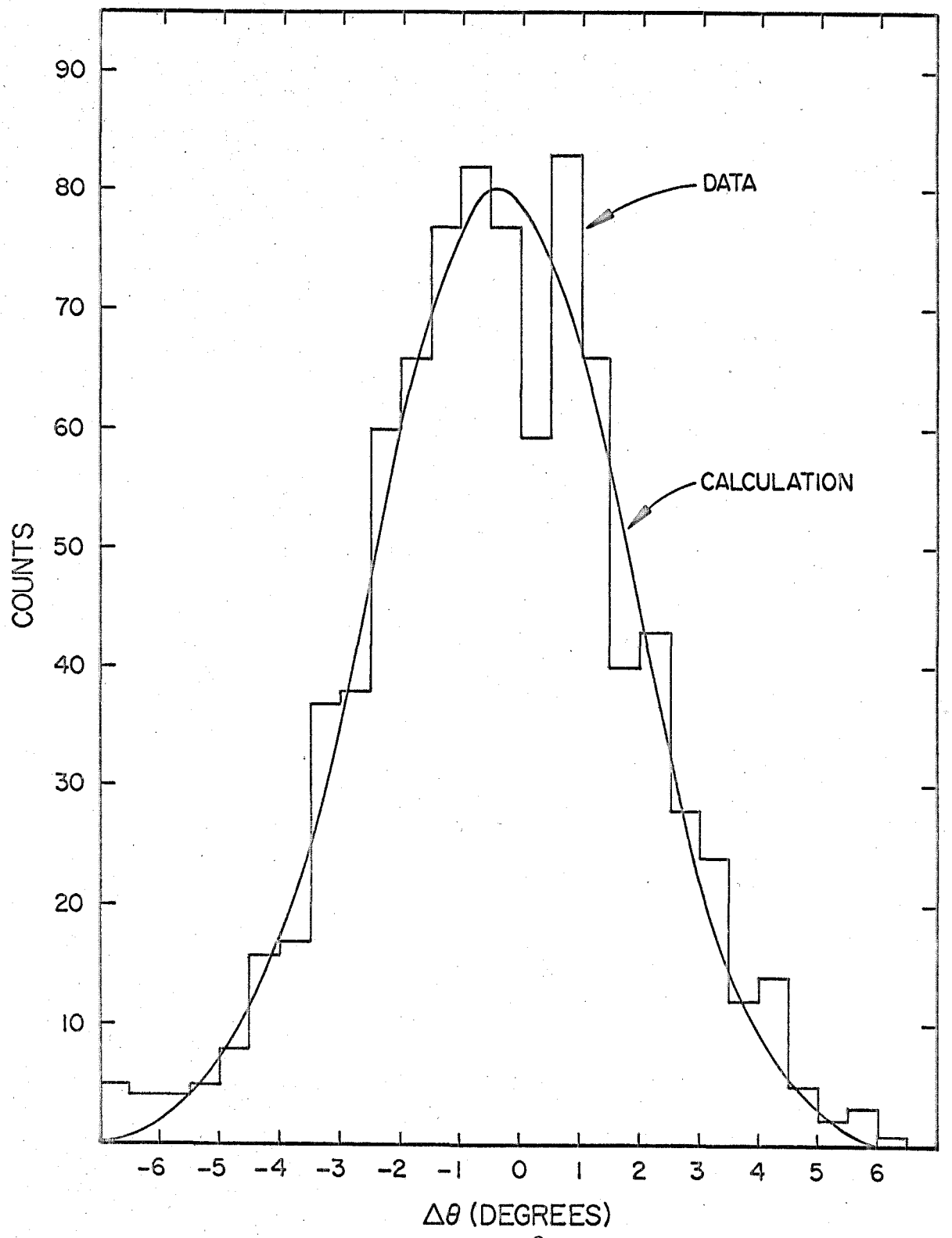

Figure 7.11 $\Delta\theta$-distribution for π^0 check runs; comparison of data with Monte Carlo calculation

the "mass" of the pion resulted in values of M_{π}^{2} less than 0. This was clearly nonsense and therefore the $\Delta\theta$-distribution was more appropriate.

The goodness of the $\Delta\theta$ calculation permits considerable confidence in the goodness of the mass calculation for the eta runs.

Figure 7.12 shows the distribution of the events in k. The histogram is the data. The solid curve is the function

$$F(k) = Eff(k)* B(k)/k \ ,$$

broadened by the experimental resolution in k. For a constant cross section, the data and the curve should have the same shape. The variation of the data from the curve shows, then, the variations in the π^{o} photoproduction cross section. Figure 7.13 shows the photoproduction cross section obtained in this experiment along with values obtained in this region by other experiments. The agreement between this experiment and other experiments is taken to mean that no significant systematic errors exist, and that the experiment overall worked as expected.

b) Shower Counter Pulse-Height Distributions

The behavior of the shower counters was carefully observed, prior to the experiment, in the electron beam. At the time the counters were designed, monoenergetic "tagged" photons were not available, so all distributions are electron-induced shower distributions. However, for a counter of this design, i. e., totally absorbing, the pulse-height distributions depend only on the total energy in the shower, and are the same for electrons

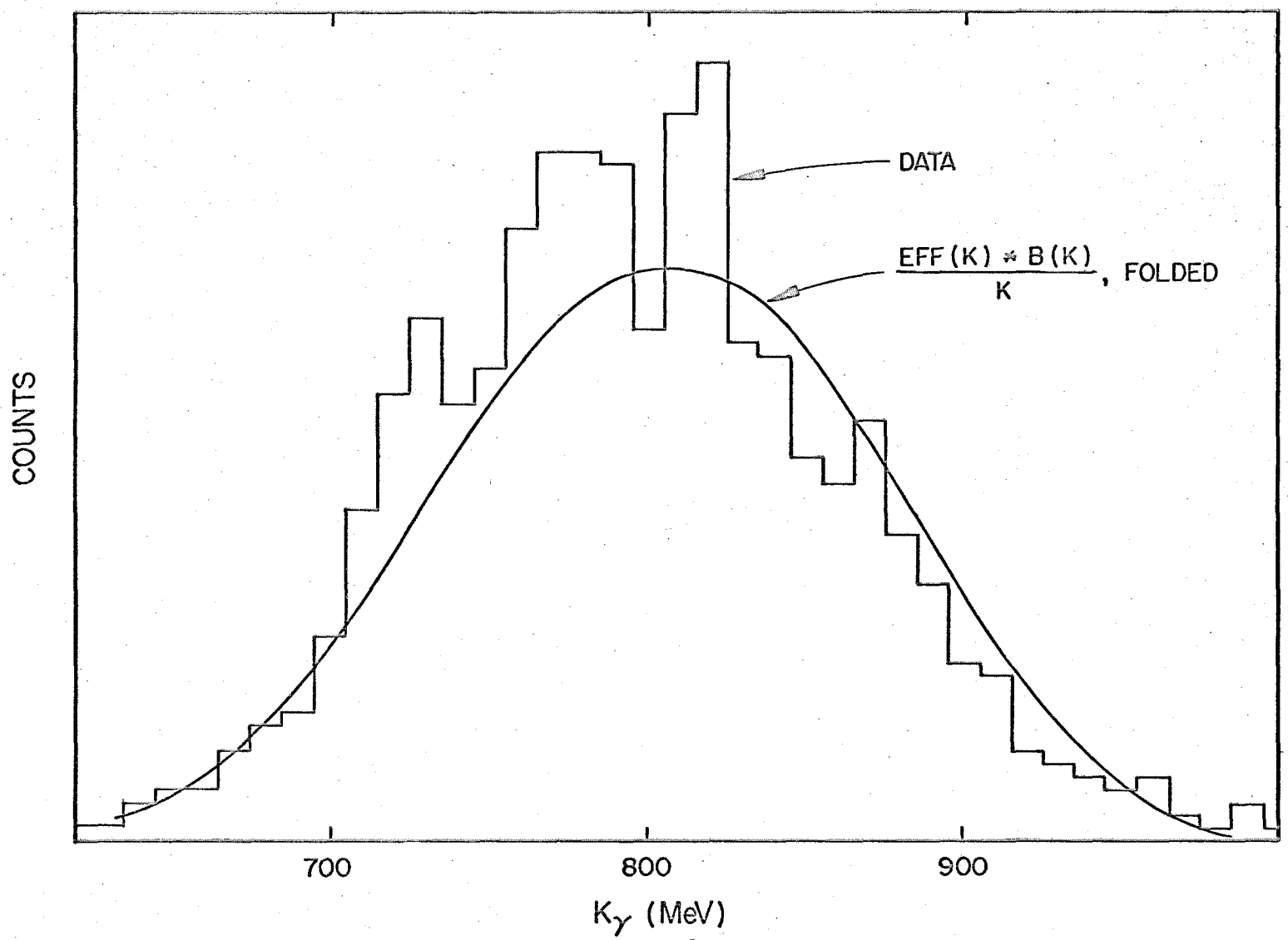

Figure 7.12 K-distribution of events from π^o photoproduction compared with the geometrical detection efficiency

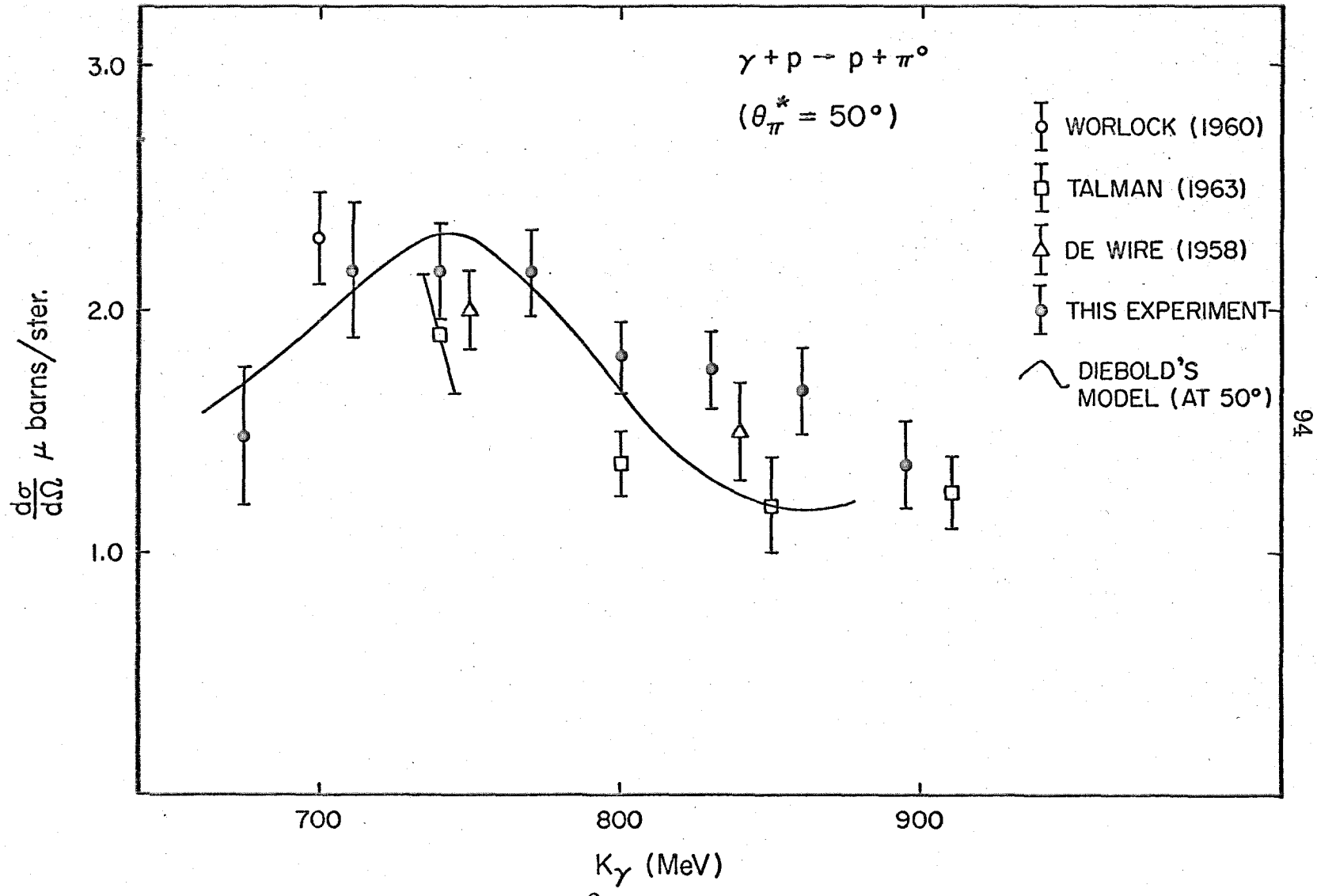

Figure 7.13 Cross section for π^o photoproduction obtained from check runs

(or positrons) and photons of the same energy. Because electrons are experimentally much easier to handle, the test distributions are from electron-induced showers.

Figure 7. 14 shows the pulse-height distributions of the electron beam tests and those obtained from the good events of the experiment. The dashed curve in the lower section is the expected broadening due to variations in the photon energy that each counter sees, 400 to 500 Mev, which arise from variations in the eta energy and the decay angles of the two photons. The upper part shows the pulse-height distributions from the experiment. The π-distribution was obtained by means described in Section VII-C.

Figure 7. 15 shows the distribution of pulse heights in the shower counters taken from the off-kinematics runs (top histogram) compared to the pulse-height distribution for events taken from the wings of the mass plot for the eta runs (bottom histogram).

c) Beam Monitoring

Beam monitoring is necessary to obtain proper normalization of each run. The function of the quantameter is to provide parameters for calculation of the number of incident photons. A Wilson quantameter[27] was mounted in the concrete beam stopper. The output of the quantameter was fed into a charge integrating circuit. Calibration of the integrator was performed at various times during the runs and remained constant to $\pm$ 1%. The integrator calibration and the quantameter constant gives a value

$$1 \text{ B. I. P.} = 1.17 \times 10^{13} \text{ Mev} .$$

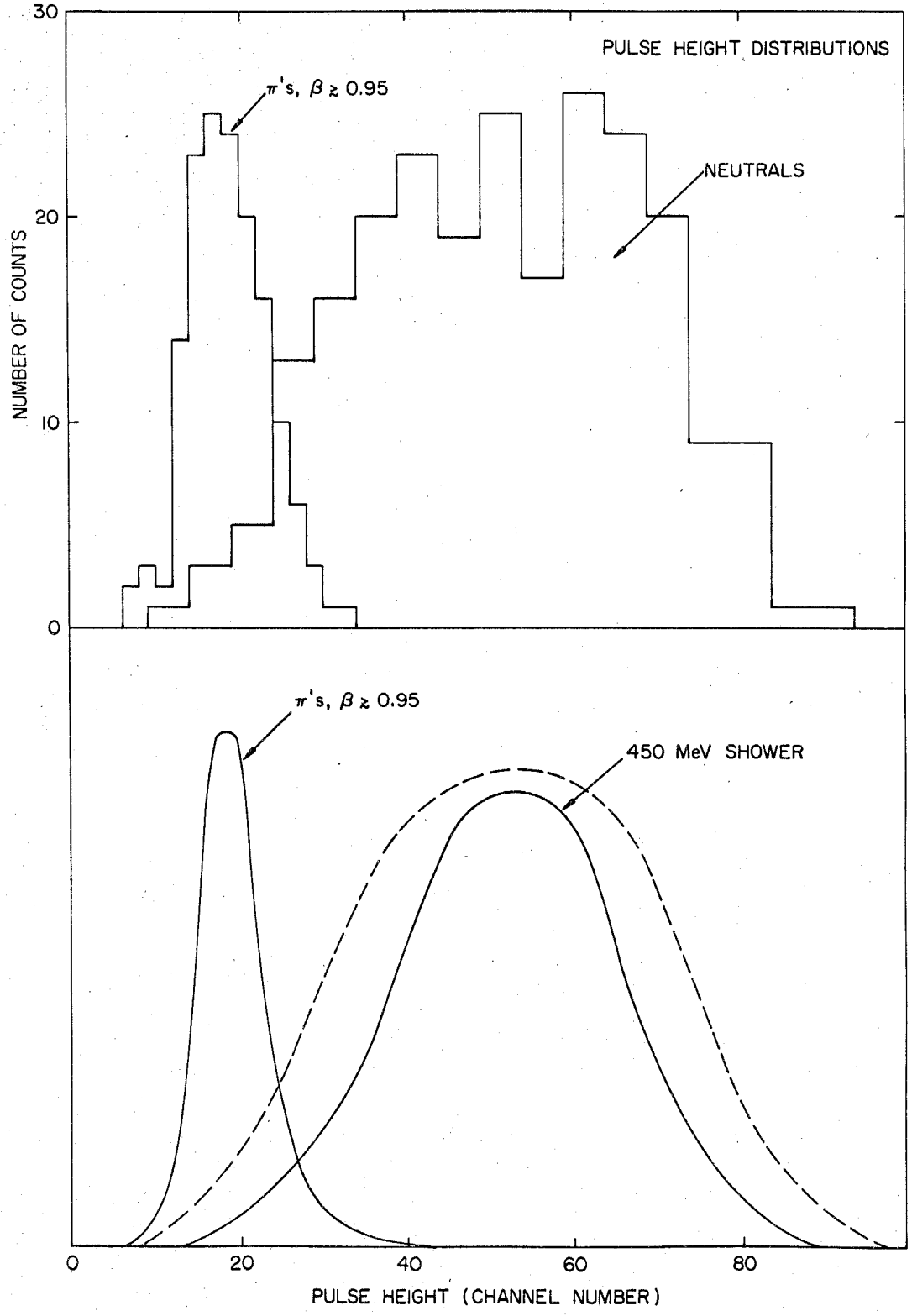

Figure 7.14 Pulse-height distributions in shower counters for all events surviving criteria, compared to standard distribution from pion telescope and electron beam tests

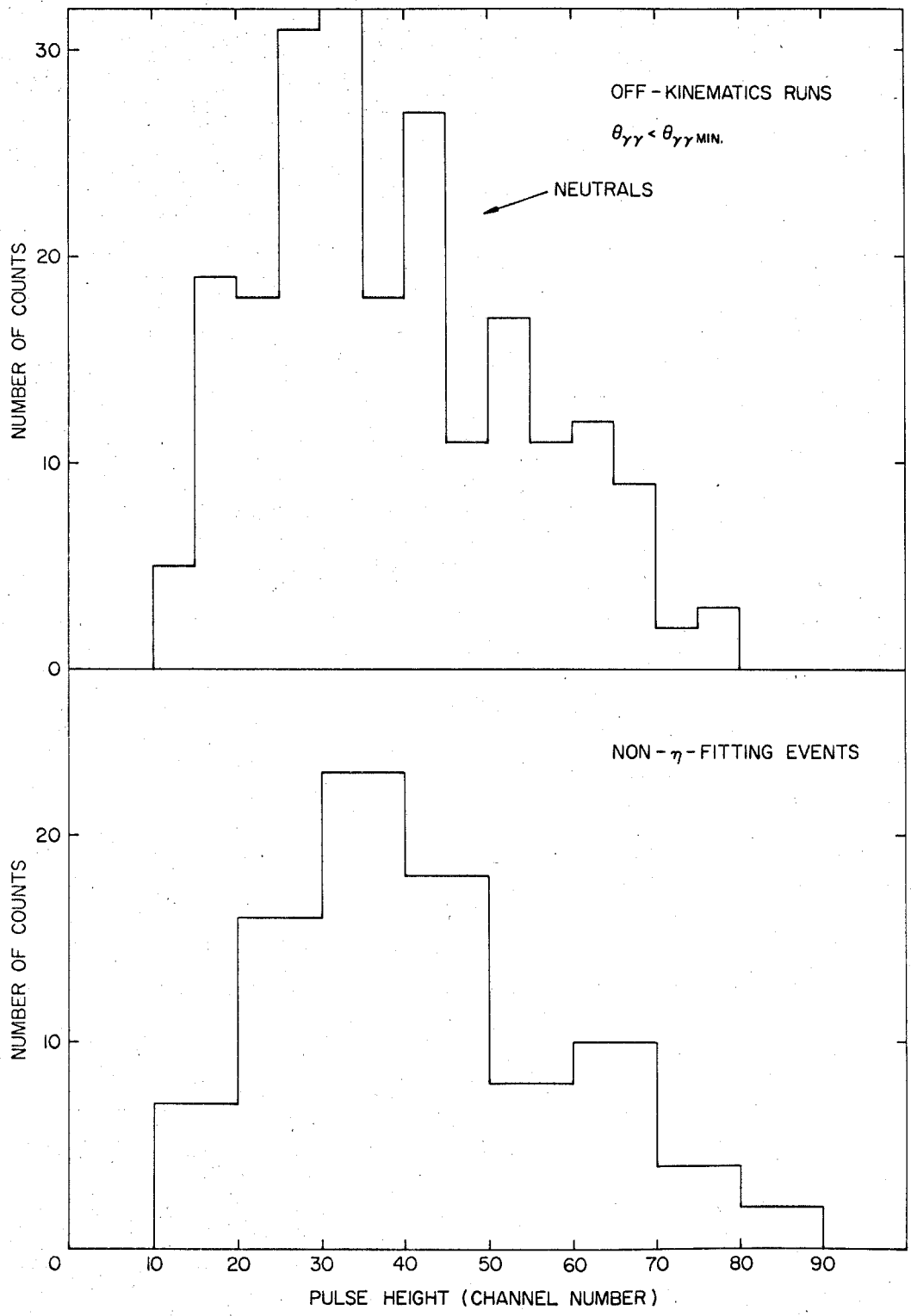

Figure 7.15 Comparison of pulse-height distribution from off-kinematics runs with that from non-eta-fitting events taken from wings of the mass plot

The quantameter constant depends on its internal pressure and temperature. However, the device was mounted behind lead and paraffin shielding, rendering it difficult to maintain continual monitoring. Therefore, the normalization is assumed to be constant during the runs. Variations during the eight weeks of running are insignificant compared to the statistical error of the experiment.

It was desirable to have available independent consistency checks on the beam. For this purpose a monitor telescope was constructed out of two small scintillator counters with lead mounted between them. The counters were pointed so that particles from the target could pass through both counters. This monitor then served as a check on the target condition and beam intensity. However, the monitor failed in the middle of a run, so data from this device had to be discarded. Instead, the proton telescope, which is a monitor of sorts, has been used to check on the counting rate consistency. Figure 7.16 shows the number of counts accumulated in the proton telescope per run during the course of the experiment. The only significant change came early in the experiment when the bias on the third scintillator was changed by a small amount. Otherwise the counting rate remained quite constant.

The counter biases in the proton telescope were set quite conservatively as shown in Figure 7.17. Variations in gain during the runs would have shown up quite strongly in the rates observed in the proton telescope. The consistency of the proton rates shows that the proton telescope and the quantameter normalization behaved normally during the runs.

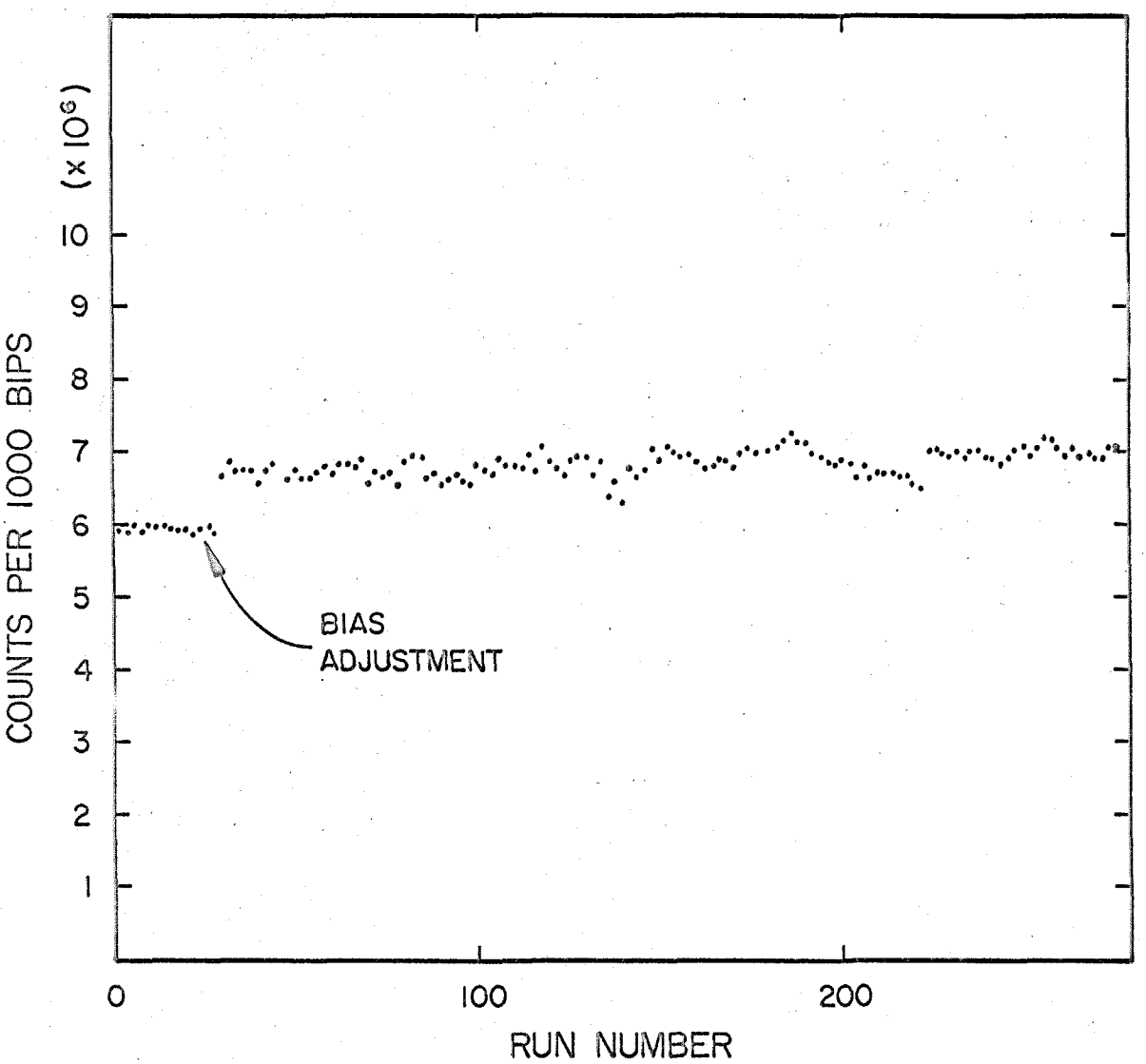

Figure 7.16 Consistency of the proton telescope counting rate

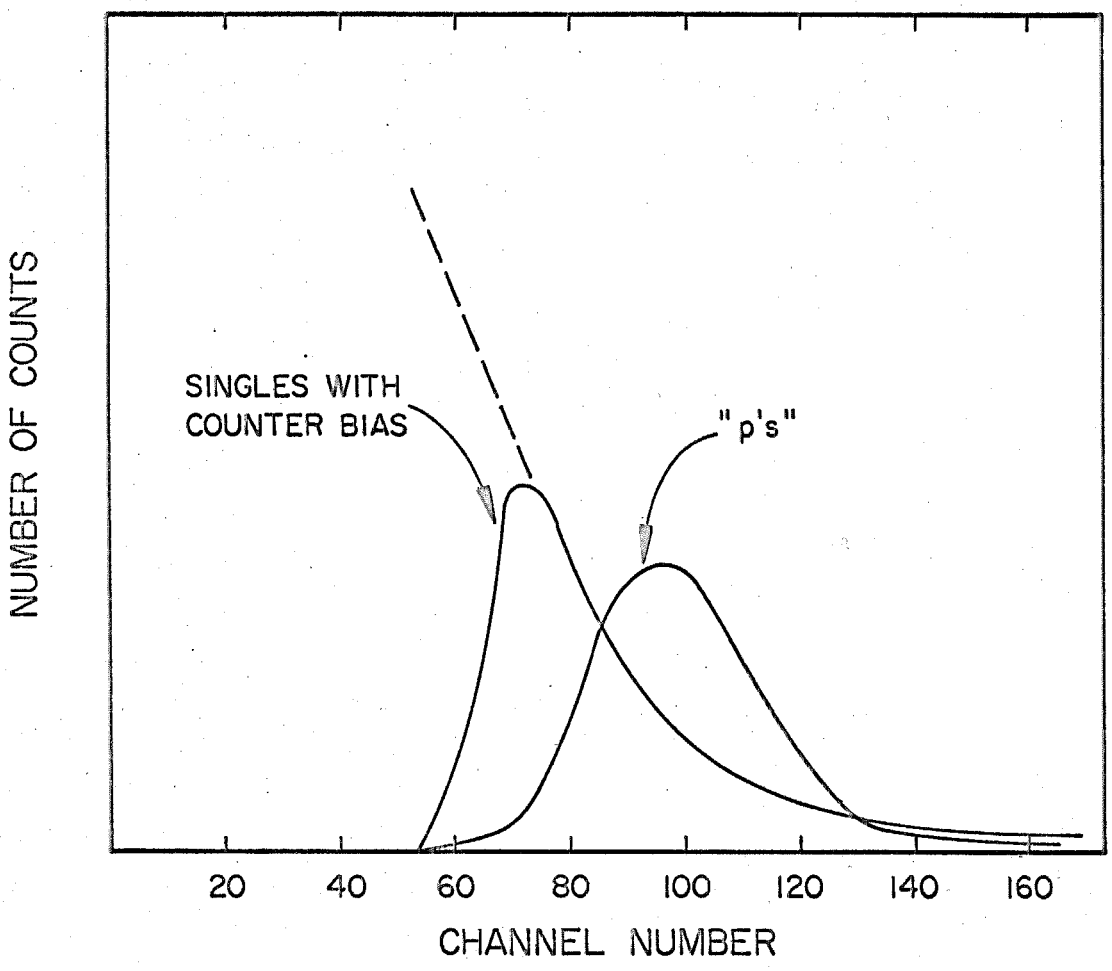

Figure 7.17 Typical proton pulse-height distribution for counter in the proton telescope. Also shown is the distribution of single counts with the electronic bias cutting out the lower pulse heights.

C. Counter Calibration

a) Proton Telescope Calibration

Careful attention to bias settings on each counter was very important to a good cross section measurement. One hundred percent efficiency in each of the three counters had to be guaranteed, and furthermore, careful adjustment of the bias was needed to discriminate against π's and e's. For this purpose, a fourth counter was placed in the proton telescope, behind the range chamber. The bias on this counter was set very high, so that only the largest of pulses triggered the electronics. This counter was placed in the fast logic, and could be turned on when needed. The four counters then defined particles coming from the target, and the requirement that the fourth have a large pulse restricted the events to protons which stopped in it. This technique gave a clean trigger of slow protons for use in setting gains of the first three counters.

The pulse-height distributions from slow protons were obtained for each of the proton counters in a pulse-height analyzer, along with the pulse-height distribution for singles in that counter. Figure 7.17 shows a typical set of distributions obtained in this way. The counter bias and proton peaks are clear.

Voltages on all phototubes were monitored between runs by means of a digital voltmeter. Variations on phototube voltages were constant to 1 part in 10^4.

b) Shower Counter Calibration

It was necessary to be able to set the discrimination level on the shower counters during the experiment. For that

purpose a pion telescope was set up for each shower counter (see Figure 7.5). Behind the shower counter were placed two scintillator counters of smaller aperture, separated by 6" of lead. This lead plus the lead contained in the shower counter was enough to stop all particles except fast π's and μ's. For π's reaching the back counter, the incident kinetic energy was in excess of $T_\pi = 300$ Mev, for which $\beta_\pi \geq .95$. These fast π's thus provided a good means for calibrating the pulse heights of the shower counters. Also, these π's were used to test the hodoscope scintillators and the veto counters. The veto counters exhibited $\geq 99\%$ efficiency during the experiment, and the scintillator counters showed 99.5% efficiency. The discrepancy is probably due to contaminating events in the π-trigger and not a real counter inefficiency. Figure 7.14 shows a typical π-spectrum obtained during the runs.

D. Photon Conversion Efficiency

Detection of photons in the scintillator hodoscopes was required for kinematical reasons. In order for the photons to trigger one of the scintillators, the photon had to pair-produce an electron-positron pair in the lead in front of the scintillators. This materializing or "converting" process then allowed angular measurements to be made for each photon.

If the probability for converting in the $2X_o$ of lead is δ, then the efficiency for detecting both photon is δ^2. It is very important to know the numerical value of δ in order to obtain accurate cross sections. Measurement of the quantity δ was performed in the tagged photon beam. Electrons of energy E_1 were selected by a magnet and allowed to impinge on a thin copper

radiator. A small percentage of these electrons undergo bremsstrahlung in the copper, and come out with energy E_2. A second magnet selects only those electrons of energy E_2 in fast coincidence with an incoming electron. The remaining energy is that of the "tagged" photon, $k = E_1 - E_2$. These photons are used to measure the conversion in the $2X_0$ of lead. Figure 7.18 shows the conversion efficiency for the experimental configuration ($2X_0$ of lead + 1/4" scintillator + .060" copper sheet) for energies from 200 - 600 Mev. The value of interest is at k = 450 Mev and is

$$\delta = .784 \pm .005 \quad .$$

E. Measurement of the Edge Effect in the Shower Counters

The shower counters were run in a self-defining aperture configuration. That is, the aperture of the counter was defined by the physical size of the counter. Showers incident on a region very near the edge of the counter are likely to "leak out" of the counter and fail to register as full pulse heights. The "effective" aperture thus is smaller than the physical aperture, and measurement of the effect is important for calculating the effective solid angle of the apparatus.

The electron beam was used for this test. A small defining counter (1/4" x 1/4" x 1/16") selected a very narrow beam of electrons of 1/16" thickness. The counter was placed against the shower counter near the edge, and successive runs were taken with the defining counter moved closer to the edge for each run. The percentage of the showers having pulse heights above the counter bias is plotted in Figure 7.19. The efficiency drops to 0 at the

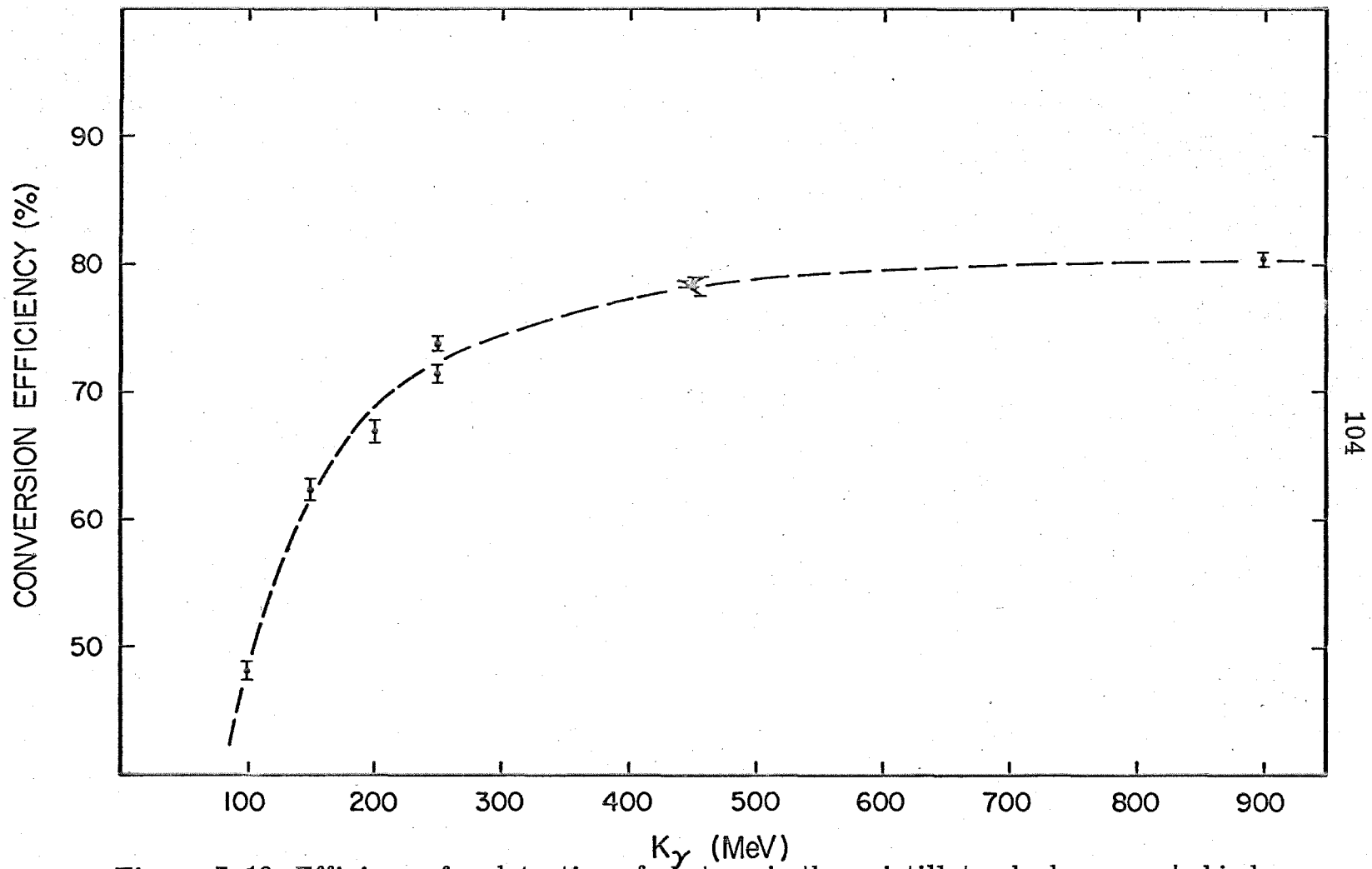

Figure 7.18 Efficiency for detection of photons in the scintillator hodoscope, behind lead converter used in experiment.

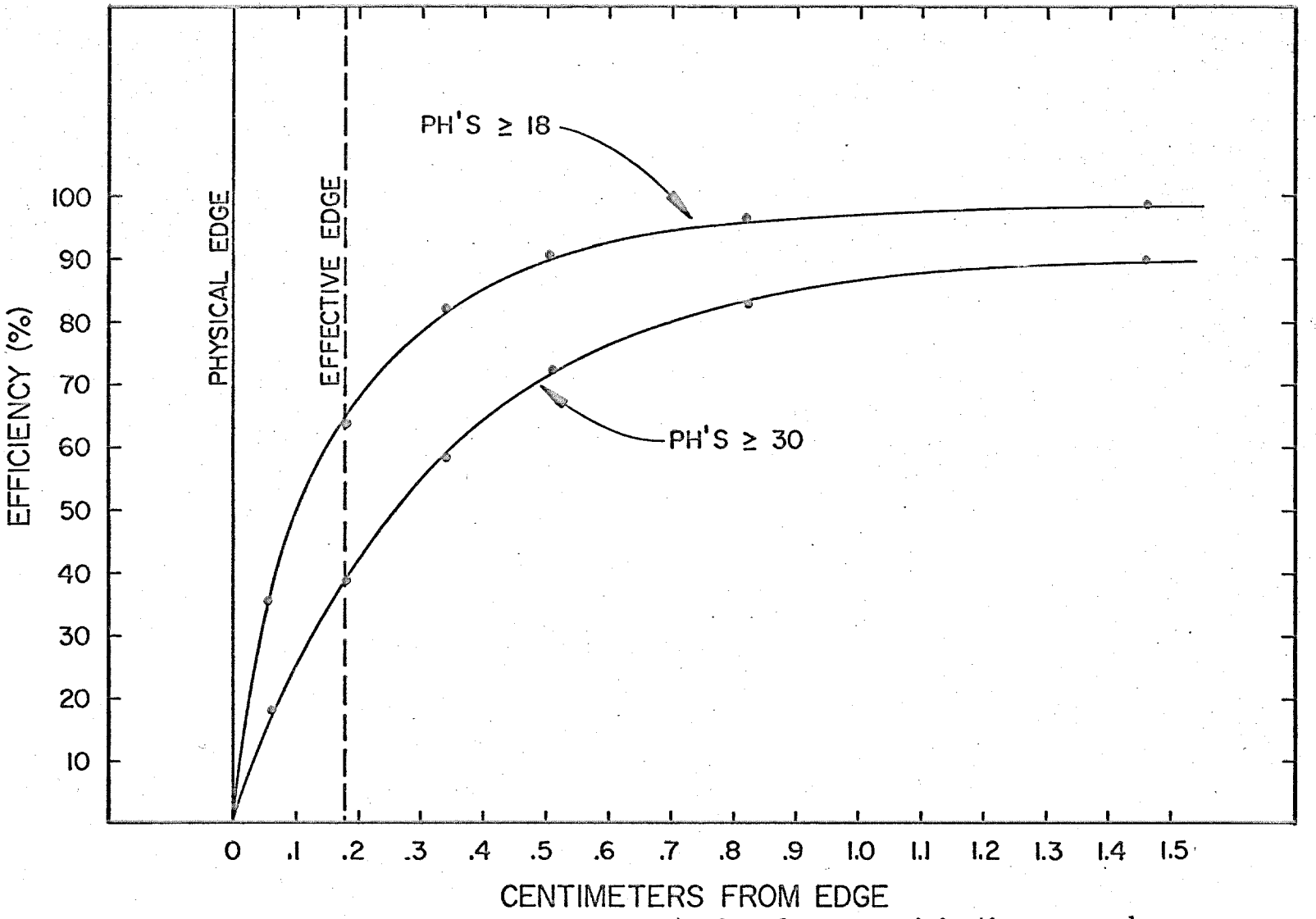

Figure 7.19 Efficiency of shower counters for showers originating near edge

physical edge of the counter, and rises to 98% in the interior region. The effective edge of the counter is defined as the value for which the number of showers lost inside are equal to the number of showers retained outside (i. e., best step-function fit to the curve). The value for the edge correction depends on the counter bias. For the bias used in this experiment, the value is

$$\Delta x = .18 \text{ cm for 450 Mev showers} .$$

F. Spark Chamber Efficiency

A problem commonly encountered in spark chambers is that of multitrack efficiency. Fortunately in this experiment only one track per event was expected. For a range measurement, it was necessary only to have a high efficiency for single tracks, and the chambers were designed to optimize the efficiency. The chamber was constructed of modules which could be placed between the aluminum absorber plates. The module had two gaps with a center thin foil. The thin foil acted as the high voltage electrode, and the aluminum plates were grounded. Thus, a track in the chamber was illuminated by two sparks between each absorber. By requiring only one of the gaps, or both, to fire, the efficiency of the two gap module is much better than that of a single gap module.

Efficiencies of the gaps were measured by exposing film on passing protons defined by the proton telescope. Measurements were taken for the clearing field set at 50 volts and 75 volts. The result for the gaps are given in Table 7. 1.

The gap efficiency is not as good when more than one track is found in the chamber. Presence of other tracks tends to "rob" sparks and lower the efficiency. The presence of more than 1 track

TABLE 7.1

Spark Chamber Gap Inefficiencies*

Chamber	Gap	% Misses 50 Volt Sweep Field	% Misses 75 Volt Sweep Field
Hod 1	1	0	0
	2	0	0
	3	0	.5
	4	0	.5
Hod 2	1	0	0
	2	0	0
	3	0	0
	4	0	0
Range	1		
	2	.5	0
	3		
	4	1.1	0
	5		
	6	0	0
	7		
	8	3.8	2.5
	9		
	10	0	.5
	11		
	12	0	.5
	13		
	14	0	.5
	15		
	16	0	1.0
	17		
	18	0	1.0
	19		
	20	.5	.5
	21		
	22	0	.5

* Measured on 100 events, each sweep field setting.

in the spark chambers was not serious. Only when two tracks appeared in the range chamber simultaneously was the analysis impossible. Corrections for this problem were treated as a systematic effect. When multiple tracks appeared in the first chamber, generally the good track could be found by requiring that it line up with tracks in the back chamber. When the good track could not be identified, the analysis program ignored the front chamber, and used only the back hodoscope chamber and range chamber for proton information. This, of course, gave more error in the measurements, but occurred in less than 10% of the cases.

The number of observable tracks, averaged over the whole experiment, are given in Table 7.2. The number of tracks seen in a chamber is dependent on the length of the chamber memory. Memory of the track occurs because ions in the chamber gas remain near the track of the particle for several microseconds before drifting away or recombining. If the memory can be shortened, the number of tracks seen will be proportionately reduced. This is achieved by adding a quenching agent to the gas that flows through the system. Helium gas was bubbled through ethanol and mixed with argon in the ratio 1 part helium to 5 parts argon. Tests showed that the efficiency was insensitive to this ratio. A d. c. voltage was maintained across the gaps at all times to assist in clearing out the old ions. The memory of the chamber was shortened in this way to about 1 microsecond. Figure 7.20 shows the range chamber gap efficiency as a function of sweeping field applied and triggering delay. These curves are important because one must set the sweeping field so as to minimize the chamber memory time without effecting the chamber efficiency.

TABLE 7.2

Average Tracks per Event in Spark Chambers

Chamber	Tracks / Event
Front Hodoscope	2.17
Back Hodoscope	1.99
Range	1.04

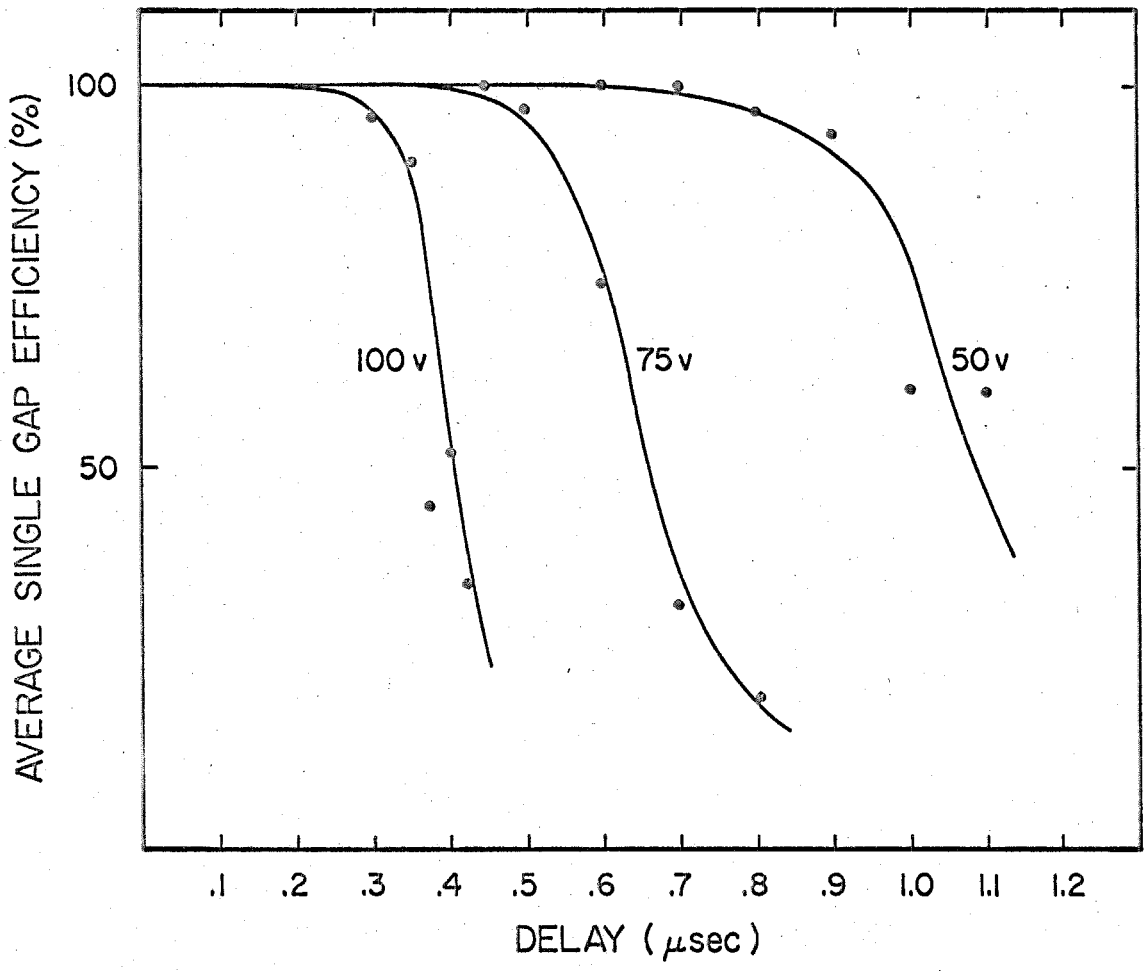

Figure 7.20 Spark chamber single gap efficiency versus delay of trigger to the plates

G. Nuclear Interactions of the Proton

The data on nuclear interactions of protons in aluminum that can be found in the literature is woefully inadequate to do a proper calculation of the effect on the range of protons due to nuclear interactions. The measurement of total cross section for interaction is hardly adequate, since most interactions in the 100 Mev range are elastic, resulting in small changes in the range. The best data available is that of Strauch and Titus[28, 29]. Their work with carbon required a ratio of 60% elastic scatters to 40% inelastic scatters. Measurement of the outgoing energy spectrum of the proton shows a sizeable elastic peak and a broad continuum. The effect of nuclear interactions on the experiment was estimated under the assumption that 60% of these events were elastic and 40% were inelastic. A Monte Carlo program already existed from earlier calculations which generated events under the experimental conditions (see Section III-F). It was modified to force the proton to undergo interactions in the range chamber. The interaction was allowed to occur at any point along the path with equal probability. The point of interaction having been chosen randomly, then the energy loss in the interaction was found, and the proton then was allowed to continue on its path until it stopped. The resulting range was modified because of the interaction and thus fell short, in most cases by not very much. Figure 7.21 shows the calculated distribution in mass for events undergoing such nuclear interactions. There is a noticeable skewness of the curve. However, in the experiment, these events occur only 5% of the time. Of these, only 15% of the events are lost because they fall outside the accepted

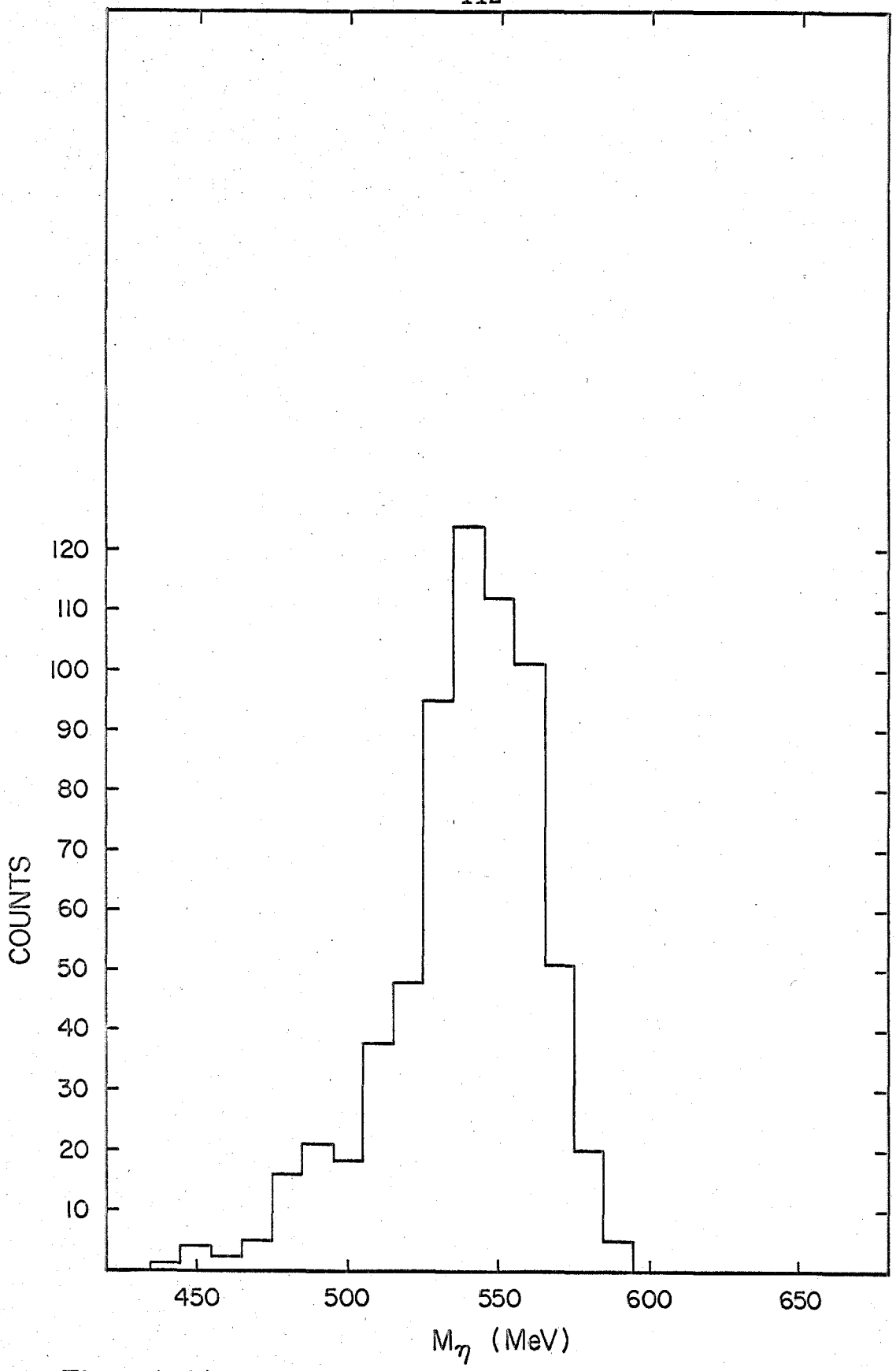

Figure 7.21 Expected mass distribution for events undergoing nuclear interactions in the range chamber

region in the mass distribution. This amounts to an overall .75% correction. This correction is accounted for in the section on systematic effects.

H. Calculation of Contamination from $3\pi^0$ and $\pi^0 2\gamma$ Decay of the Eta

Calculation of contamination to the experiment from other processes is a difficult calculation to perform when three of the many particle final state are required. The calculation depends critically on the model used and hopefully any approximations used are good. The simplest calculation to do is that of the decays of the eta into its contaminating modes

$$\eta^0 \rightarrow 3\pi^0 \rightarrow 6\gamma\text{'s}$$

and

$$\eta^0 \rightarrow \pi^0 2\gamma \rightarrow 4\gamma\text{'s} \quad .$$

These events cannot be used in the experiment simply because they cannot be identified as eta events. The presence of 4 or 6 photons in the final state allows the necessary kinematical constraints to be lost.

In order to evaluate the number of events expected it is necessary to know both the production cross section and the detection efficiency. The production cross section, however, is the question being asked by the experiment. It is known at least approximately by a preliminary analysis of the data, and the value of .2 μbarns/steradian was settled upon for the purpose of the calculation. The final value of the cross section is insensitive to this number. To evaluate the detection efficiency, a new Monte Carlo program was written. It was divided into two separate pieces; the efficiency for

detecting 2 of the 6 photons, and the distribution of protons in θ_p and T_p.

Consider first the problem of detection of 2 of the 6 outgoing photons. Photons which decay from the $3\pi^o$ in the eta center-of-mass must be transformed into the lab, or

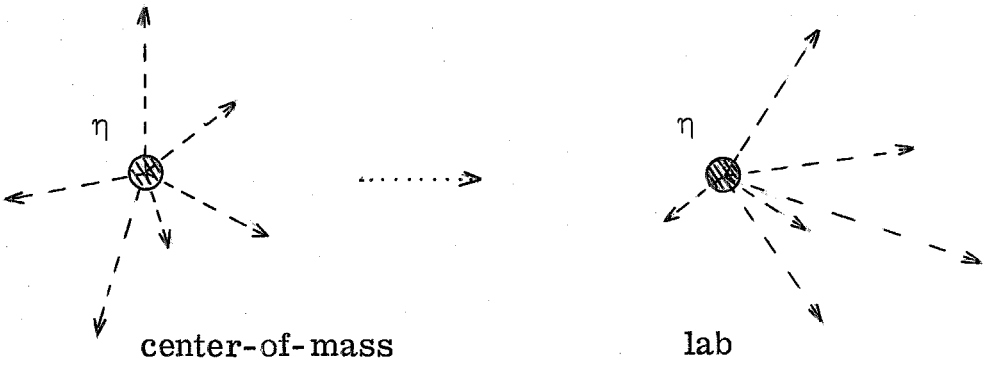

an equivalent approach would be to transform the shower counters into the eta center-of-mass

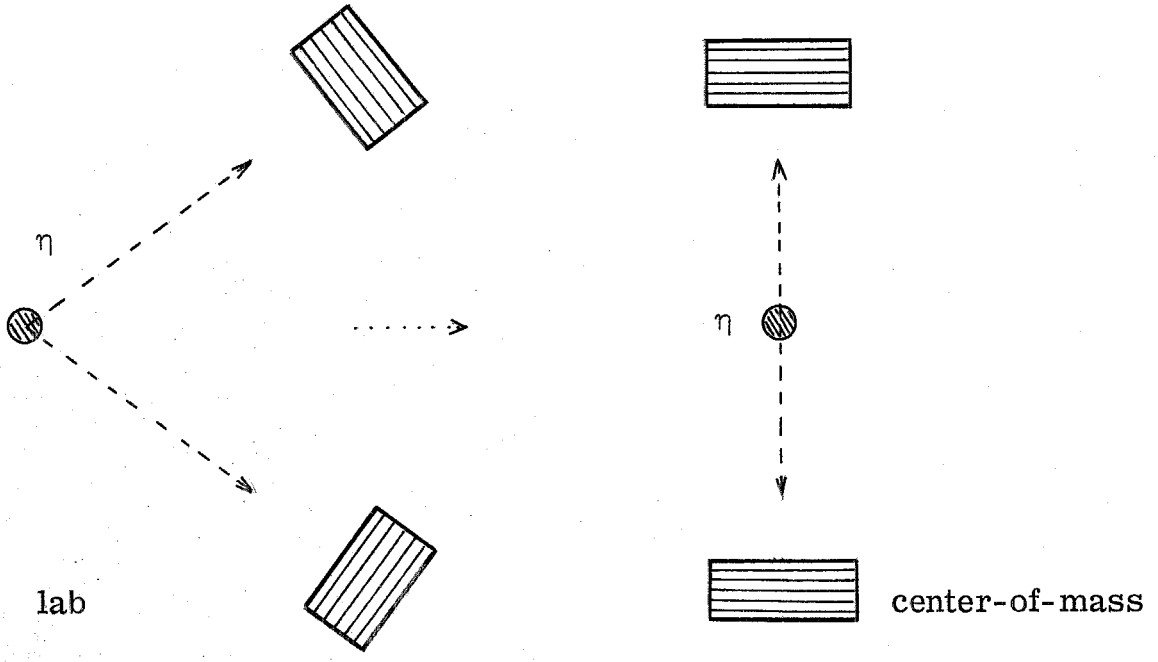

The latter approach was the one taken. The counters are transformed into the center-of-mass and the solid angle is transformed according to

$$\Delta\Omega^* = \Delta\Omega_{LAB}\left(\frac{d\Omega^*}{d\Omega}\right)$$
$$= \Delta\Omega_{LAB}\frac{1-\beta_\eta^2}{(1-\beta_\eta\cos\theta)^2}$$

where $\cos\theta$ = projection of the position vector of the shower counter onto the eta direction.

If the problem were to detect a single photon from the decay, then the problem would be essentially solved at this point. Since the eta meson is a spin zero particle, it can carry no information about spatial directions in its center-of-mass. The decay into $3\pi^o$ and then into 6 photons with all directions equally preferred means that probability per unit solid angle for detecting a photon is constant.

However, in this experiment, two counters are used. The probability for detecting two of the six photons is not simply the product of that of the two counters alone. A direction in the eta center-of-mass has been defined when one counter detects a photon, and the distribution of the remaining photons is no longer isotropic. This results purely from kinematical considerations. When one photon is given a direction in the center-of-mass, the other five must carry a net momentum equal in magnitude but opposite in direction. There will be a net enhancement for the remaining photons to go backward in the center-of-mass, toward the other shower counter. This effect, it turns out, is not negligible. One

must calculate the amount of enhancement when two photons are being detected. It is easy to see that the effect will be more pronounced for higher energy photons. Figure 7.22 shows the distributions in the eta center-of-mass of $\cos\theta_{\gamma\gamma}$ for all pairs of photons in the decay. This set of distributions was calculated from a phase-space model of the $3\pi^0$ decay of the eta, where the mass of two of the π^0's was chosen randomly from a phase space distribution. The invariant phase space distribution has the form[30]

$$P(M_{\alpha\beta}) = \text{const.} * \sqrt{\left\{m_\eta^2 - (M_{\alpha\beta} + m_\pi)^2\right\}\left\{m_\eta^2 - (M_{\alpha\beta} - m_\pi)^2\right\} * \left\{M_{\alpha\beta} - 4m_\pi^2\right\}\left\{M_{\alpha\beta}^2\right\}}$$

where $M_{\alpha\beta}$ is the mass of the π^0 pair. The π^0's are then allowed to decay and the direction and energy of each photon is retained. The correlated $\cos\theta_{\gamma\gamma}$ is then computed for each eta decay and the values are added to the distributions in Figure 7.22. This procedure is repeated with different bias on the photons. That is, photons whose energy falls below the bias are disregarded. In this way, the experimental counter bias can be taken into account.

This information now allows the calculation of the efficiency for the $3\pi^0$ decay mode of the eta. The probability for detecting two of the photons is then

$$N_{eff} * \frac{\Delta\Omega_1^*}{4\pi} * (N_{eff} - 1) * \frac{\Delta\Omega_2^*}{4\pi} * \text{Factor}(z)$$

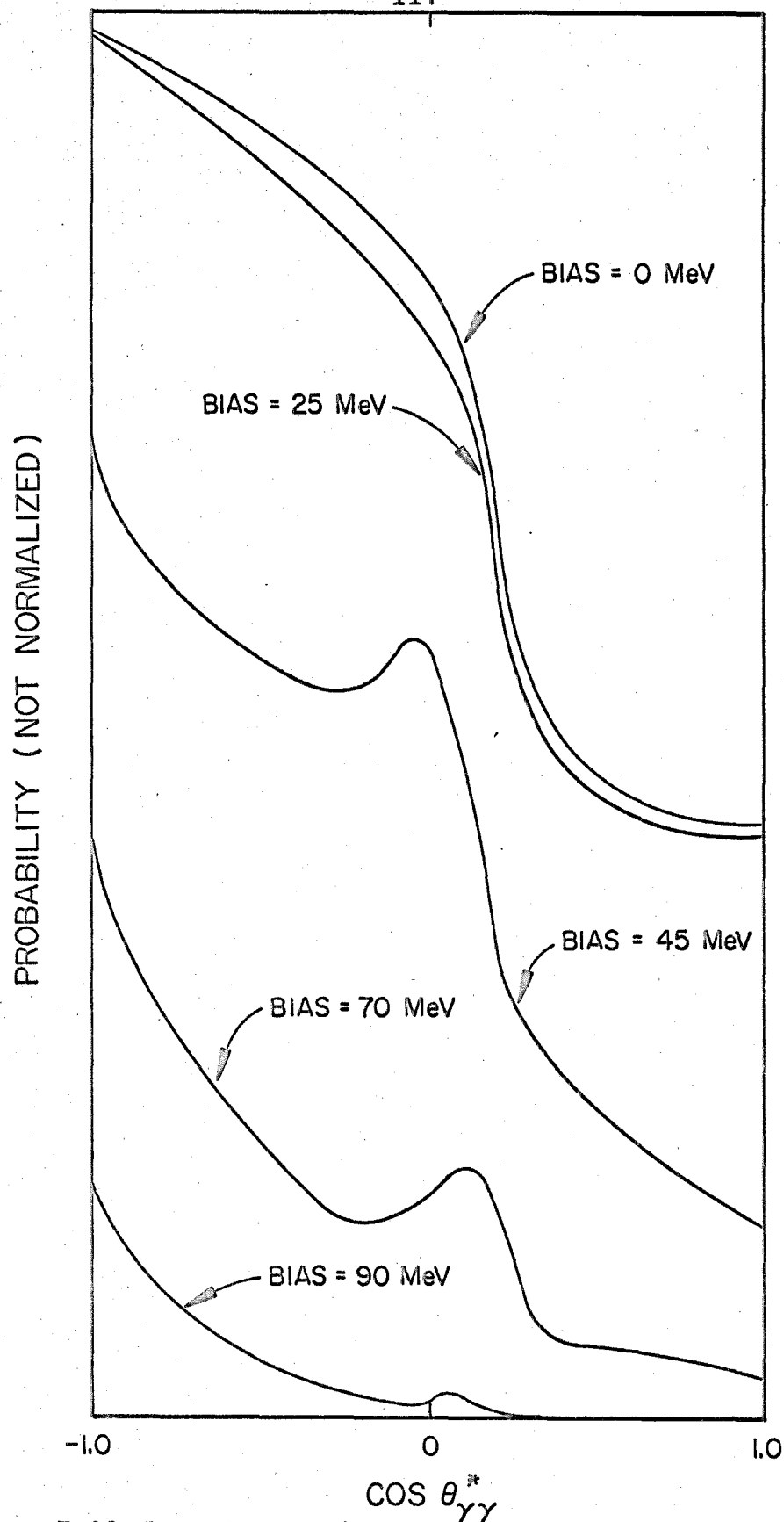

Figure 7.22 Distribution of opening angles for γ pairs from $3\pi^0$ decay of the eta (all pairs considered) in the eta center-of-mass

where N_{eff} is the effective number of photons from the decay which have energies greater than the counter bias, and Factor(z) is the enhancement from the correlated $\cos\theta_{\gamma\gamma}$ distributions. (z is the cosine of the angle between the two shower counters in the eta center-of-mass).

A Monte Carlo program was written to take the proton half of the experiment into consideration. Introduction of target and beam parameters allows the counting rate to be evaluated. Figure 7.23 shows the expected number of counts for the 1025 Mev run of this experiment.

Another neutral decay mode of the eta contributes to the background. The process

$$\eta^0 \rightarrow \pi^0 + \gamma + \gamma$$

gives four outgoing photons, two of which are required to trigger the system. The branching ratio for this process is small and consequently the contribution to the background is small. In addition, the smaller number of photons further suppresses the contribution of this decay mode. The calculation of the efficiency for this process was similar to that of the $3\pi^0$ decay. The main difference is that the $\cos\theta_{\gamma\gamma}$ distribution is somewhat more enhanced.

I. Calculation of π^0 Pair Production Contamination

The most significant contribution to the background comes from π^0 pair production. Although the detection efficiency is somewhat smaller in this case than in the $3\pi^0$ decay mode of the eta, the cross section is large enough to raise the contamination to non-

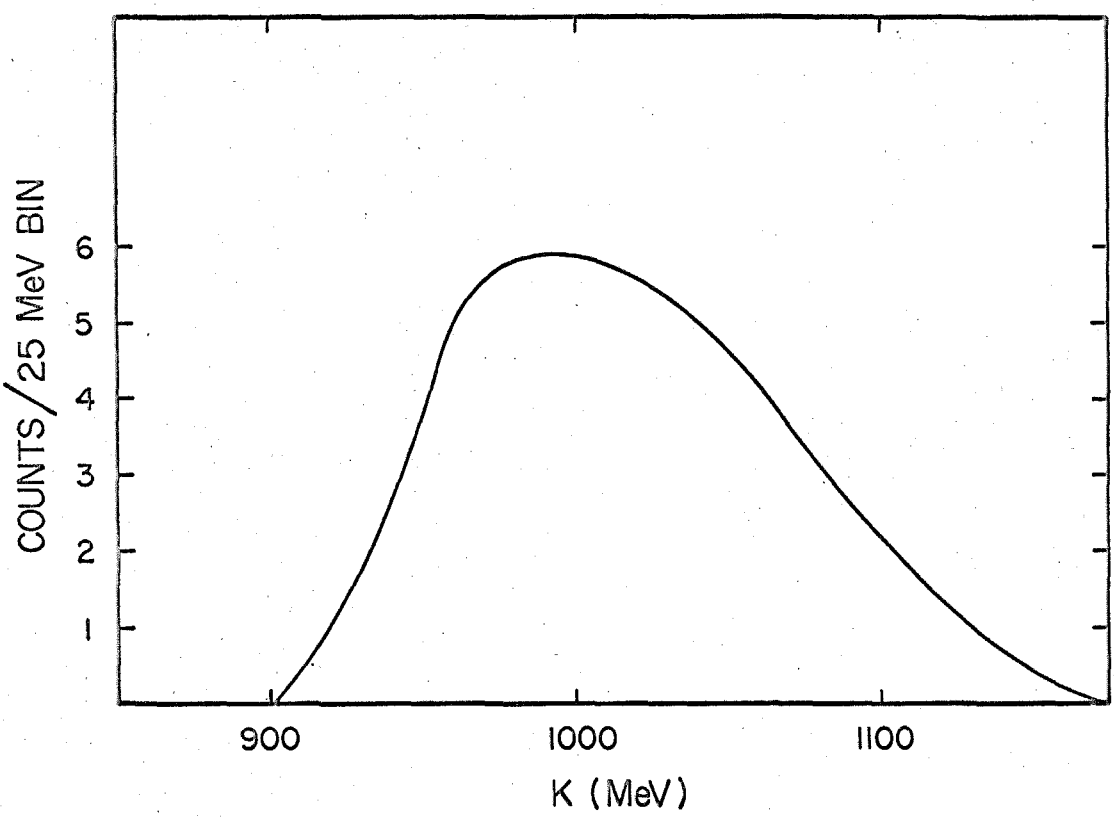

Figure 7.23 Number of background counts expected (per 25 Mev bin) from $\eta^0 \rightarrow 3\pi^0$ and $\eta^0 \rightarrow \pi^0 2\gamma$ decay modes, for Run 2 of this experiment

negligible amounts. Unfortunately, data on the photoproduction of π^o pairs is totally lacking, and one is forced to look at $\pi^+\pi^-$ data in desperation. Since the total cross section for $\pi^o\pi^o$ production is not known, it must be taken as an adjustable parameter, and the final value will be compared to the $\pi^+\pi^-$ data for reasonableness.

The calculation of the π^o pair efficiency follows closely, in principle, the previous calculations of the $3\pi^o$ and $\pi^o 2\gamma$ decay modes of the eta. It differs, however, in two important ways. First, the mass of the π^o pairs is allowed to vary between the phase space limits

$$2m_\pi \leq M_{\pi\pi} \leq E^* - m_p \ .$$

This introduces an additional free parameter which must be summed over. Secondly, the actual incident photon energy, k, from which the event originates is not the value measured by the experiment. The analysis treats all events as though they originate from in η^o photoproduction and calculates k according to

$$k = (M_\eta^2/2 + T_p M_p)/(\sqrt{M_p^2 + T_p^2}\cos\theta_p - T_p) \ .$$

But in general $M_{\pi\pi} \neq M_\eta$ means that the calculated k is wrong. Thus, in the calculation this "apparent" k must be calculated from the range and angle of the proton and this value used instead of the real k. The calculation is based on a statistical model. The mass of the π^o pair is chosen to follow a phase-space distribution. This is strictly an undynamical model for the production of π^o pairs. Dynamical processes could alter the distribution in $M_{\pi\pi}$, and clearly this is a weakness of the calculation. For example, it has

been shown that $\pi^+\pi^-$ production proceeds largely through the process

$$\gamma + p \rightarrow N^* + \pi^- \rightarrow p + \pi^+ + \pi^-$$

and how this distorts the $M_{\pi\pi\pi}$ distribution is not clear. This process should be present in $\pi^o\pi^o$ production also. However, since information seems to be lacking, it was thought that the statistical model would be a good approach. Hopefully, the results are not too sensitive to the shape of the $M_{\pi\pi\pi}$ distribution.

The calculation of the efficiency was done by means of a Monte Carlo program. It generated an event from a value of k, chose a mass for $M_{\pi\pi\pi}$ from a phase-space distribution, tested that the proton successfully entered the proton telescope solid angle, and if so, calculated the probability of two shower counters being triggered. This value, as before, was

$$P = \frac{\Delta\Omega^*_1}{4\pi} * N_{eff} * \frac{\Delta\Omega^*_2}{4\pi} * (N_{eff} - 1) * \text{Factor}(z)$$

where $\Delta\Omega^*_1$, $\Delta\Omega^*_2$ were the π-π center-of-mass solid angles of the two shower counters, and N_{eff} was the number of photons per event with energies greater than the counter biases, and Factor(z) was the enhancement from the photon correlation. This value was then stored in the distribution at the value of k computed from the angle and range of the proton. This procedure yields the geometrical efficiency. Introducing target parameters and number of incident photons on the target gives the expected counting rate. Figure 7.24 shows the results of this calculation for the 1025 Mev runs. Since

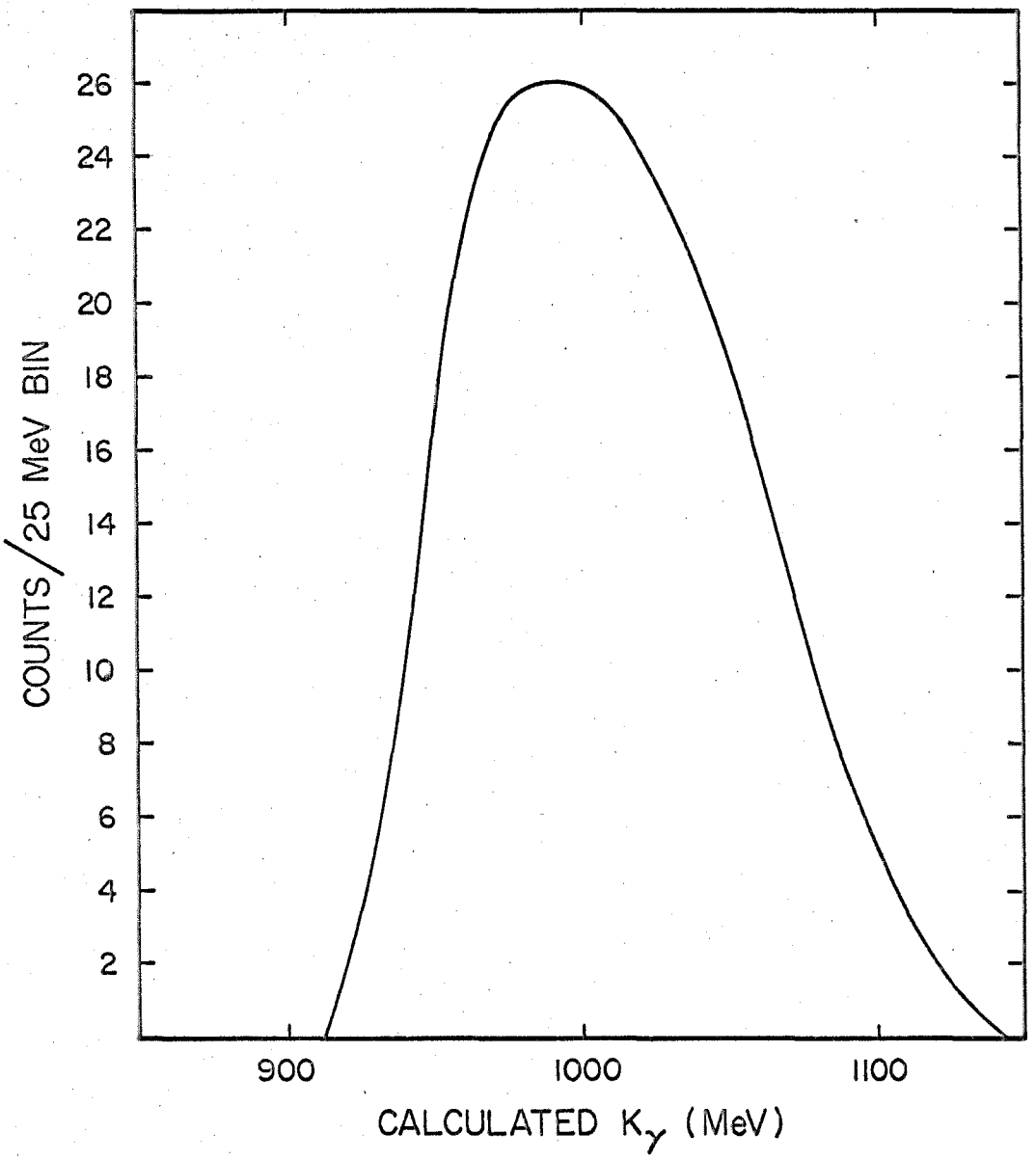

Figure 7.24 Number of background counts expected (per 25 Mev bin) from π^0 pair production for Run 2 of this experiment

the cross section at this point is unknown, it should be kept in mind that an arbitrary scale factor, within reason, exists. The cross section value used to get reasonable fits to the data are given in Section IV-B.

VIII. REFERENCES

1) A. Pevsner, et. al., PRL 7, 421, (1961).

2) M. Gell-Mann, CTSL Report 20 (1961).

3) P. L. Bastien, et. al., PRL 8, 114, (1962).

4) M. Chretien, et. al., PRL 9, 127, (1962).

5) H. W. Foelsche, et. al., PRL 9, 223, (1962).

6) F. S. Crawford, et. al., PRL 10, 546, (1963).

7) E. C. Fowler, et. al., PRL 10, 110, (1963).

8) Kraemer, Fields, Toohig, PR 136, B496, (1964).

9) A. H. Rosenfeld, et. al., "Data on Particles and Resonances", UCRL - 8030, Part I, (1965).

10) R. F. Dashen, Nuovo Cimento 32, 469, (1964).

11) A. W. Hendry and R. G. Moorhouse, Rutherford Lab Preprint, (1965).

12) D. Roper, et. al., PR 138, B190, (1965).

13) B. H. Brandsen, et. al., PRL 11, 339, (1964).

14) R. Cence, Univ. of Hawaii Report HeP 6-3-65, (1965).

15) S. F. Tuan, PR 139, B1393, (1965).

16) P. Dobson, Univ. of Hawaii Report HeP 6-5-65, (1965).

17) P. Anvil, et. al., Phys. Lett. 12, 76, (1964).

18) S. L. Glashow and A. H. Rosenfeld, PRL 10, 192, (1963).

19) C. R. Clinesmith, et. al., Proceedings of the Hamburg Conf., (1965).

20) R. Talman, et. al., PRL 9, (1963).

21) C. Bacci, et. al., Laboratori Nazionali di Frascati del CNEN, LNF 64-4, (1964).

22) W. S. C. Williams and F. Corbett, "Ionization Loss, Range, and Straggling of Charged Particles", High Energy and Nuclear Physics Data Handbook, Rutherford High Energy Laboratory, (1962).

23) UCRL - 8030, Revised April 1963 Edition.

24) J. V. Allaby, et. al., "Pair Production Below 1 Bev" International Symposium on Electron and Photon Interactions at High Energies, Hamburg, (1965).

25) C. A. Heusch and C. Y. Prescott, CTSL-41, (1964).

26) C. A. Heusch, et. al., Nuclear Inst. and Methods 29, 205, (1964).

27) R. R. Wilson, Nuclear Instruments 1, 101, (1957).

28) K. Strauch and F. Titus, PR 104 (1), 191, (1956).

29) K. Strauch and F. Titus, PR 103 (1), 200, (1956).

30) R. Hagedorn, Relativistic Kinematics, Chapter 7, (1964).